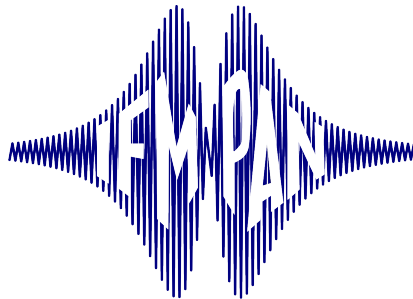


DOCTORAL THESIS

Theoretical modelling of magnetic materials based on transition metals

Justyn Snarski-Adamski

December 2024



INSTITUTE OF MOLECULAR PHYSICS POLISH ACADEMY OF SCIENCES
DEPARTMENT OF THEORY OF NANOSTRUCTURES AND QUANTUM MATERIALS

This dissertation is the result of research project PRELUDIUM BIS 1 entitled “Design of future permanent magnets” financed by the National Science Centre Poland. This project I have conducted under the supervision of **Mirosław Werwiński**.

Dissertation Submitted By:

Justyn Snarski-Adamski

Department of Theory of Nanostructures and Quantum Materials
Institute of Molecular Physics Polish Academy of Sciences

Supervised By:

Mirosław Werwiński

Department of Theory of Nanostructures and Quantum Materials
Institute of Molecular Physics Polish Academy of Sciences

Co-Supervised By:

Justyna Rychły-Gruszecka

Department of Theory of Nanostructures and Quantum Materials
Institute of Molecular Physics Polish Academy of Sciences

Acknowledgements

I gratefully acknowledge support from:

- National Science Centre Poland under decision DEC-2019/35/O/ST5/02980 (PRELUDIUM BIS 1),
- National Agency for Academic Exchange Poland under decision PPN/STA/2021/1/00014/U/00001, and
- Poznan Supercomputing and Networking Centre (PSNC/PCSS) in grant number 354.

I want to express my heartfelt gratitude to everyone who contributed to the completion of this project.

I owe a special debt of thanks to my supervisor, Mirosław Werwiński, whose unwavering support and assistance made this work possible. His boundless patience, insightful guidance, ongoing encouragement, and dedicated supervision were invaluable throughout the process. His constructive feedback, thoughtful advice, and willingness to review and improve numerous early drafts played a crucial role in bringing this project to fruition. I also sincerely thank my co-supervisor, Justyna Rychły-Gruszecka, for her invaluable guidance, support and pleasant cooperation on undertaken research projects.

I would like to sincerely thank all my faculty colleagues and teachers for their invaluable guidance throughout my graduation journey. I would like also to express my gratitude to Paweł Leśniak and Daniel Depcik for their efforts in compiling the scientific software and managing the computing cluster at the Institute of Molecular Physics, Polish Academy of Sciences.

I am deeply grateful to my parents, who have been the unwavering foundation of my life. Their endless love, steadfast support, and invaluable guidance have been my greatest source of strength. Their encouragement and faith in me have uplifted me throughout this journey, and I am forever thankful for their enduring presence in my life.

I would also like to extend my heartfelt thanks to my girlfriend, whose love, patience, and constant encouragement have been a source of immense comfort and motivation.



POLISH NATIONAL AGENCY
FOR ACADEMIC EXCHANGE



NATIONAL SCIENCE CENTRE
POLAND

Abstract

This dissertation presents a theoretical exploration of magnetic materials through a cycle of four articles published in peer-reviewed journals. Advanced computational methods were employed to investigate the structural, electronic, and magnetic properties of magnetic heterostructures, ferromagnetic ultra-thin films, antiferromagnets, and permanent magnets, providing insights into their behavior, modifications, and potential applications. The density functional theory within the implementation of the full-potential local-orbital code (FPLO) was applied to study the electronic structure of the materials. Additionally, the multislice method was employed to simulate transmission electron microscopy experiments, enabling the exploration of antiferromagnetic Bragg diffraction patterns. The results presented in the first article, covering the investigations of the magnetic properties in bcc iron-based heterostructures with an embedded atomic monolayer of transition metals, revealed agreement with the Slater-Pauling curve. Calculations also showed that Pt and W monolayers exhibit the strongest perpendicular magnetic anisotropy from all $3d$, $4d$, and $5d$ monolayers. The results in the second study, conducted in collaboration with the experimental group, identified a boundary-induced state at the Fe/MgAl₂O₄ interface, leading to the phase transition in ultra-thin iron films from body-centered cubic to body-centered tetragonal structure. Theoretical findings suggest that optimization of the substrate can enhance both the Fe film stability and the magnetocrystalline anisotropy energy. The third study employed a multislice method based on the paraxial Pauli equation, analyzing antiferromagnetic Bragg scattering in two antiferromagnetic materials NiO and LaMnAsO. The innovative computational approach of incorporating thermal effects for magnetic systems has allowed successfully reproduced experimental observations for NiO at room temperature. The study underlined experimental parameter optimization to detect antiferromagnetic Bragg scattering in materials consisting of heavier elements, which are increasing thermally diffused scattering. The fourth study examined the optimization of the magnetic properties of the CeFe₁₂ alloyed with transition metals and interstitial atoms. The results show, that alloying with the elements like Ti, Mn, and W enhances magnetocrystalline anisotropy energy, at the same time reducing the total magnetic moment, and leading to magnetic hardness sufficient to use selected materials as permanent magnets. Interstitial doping with light atoms like B, C, and N further tailored the magnetic properties of the selected alloys. Comparative studies with LaFe₁₂ revealed that Ce $4f$ electrons have a secondary impact on magnetocrystalline anisotropy energy value in the considered phases. The findings of the dissertation contribute to the design of advanced materials for spintronics and permanent magnet applications.

Keywords: density functional theory, multislice method, magnetic materials, thin films, ferromagnets, antiferromagnets, permanent magnets, magnetocrystalline anisotropy.

Streszczenie

Niniejsza rozprawa doktorska pt. *Teoretyczne modelowanie materiałów magnetycznych na bazie metali przejściowych* ma postać cyklu czterech artykułów naukowych opublikowanych w recenzowanych czasopismach i obejmuje teoretyczną analizę materiałów magnetycznych. Zastosowane metody obliczeniowe pozwoliły wykonać badania właściwości strukturalnych, elektronowych i magnetycznych w heterostrukturach magnetycznych, ultracienkich warstwach ferromagnetycznych, antyferromagnetykach oraz magnesach trwałych, dostarczając wglądu w ich właściwości, modyfikacje oraz potencjalne zastosowania. Do badań wykorzystano teorię funkcjonału gęstości w implementacji metody pełnopotencjałowej z użyciem orbitali lokalnych (FPLO). Ponadto do symulacji eksperymentów z wykorzystaniem transmisyjnej mikroskopii elektronowej zastosowano metodę wieloprzekrojową (*multislice*), umożliwiając interpretację dyfraktogramów antyferromagnetycznego rozpraszania Bragga. Wyniki przedstawione w pierwszym artykule, dotyczące badań właściwości magnetycznych w heterostrukturach na bazie przestrzennie centrowanego kubicznego (*bcc*) żelaza okrywającego atomową monowarstwę metali przejściowych, wykazały zgodność wyników z krzywą Slater-Paulinga. Obliczenia pokazały również, że monowarstwy Pt i W wykazują najsilniejszą prostopadłą anizotropię magnetyczną spośród wszystkich monowarstw $3d$, $4d$ i $5d$. Wyniki drugiego badania, przeprowadzonego we współpracy z grupami eksperymentalnymi, pozwoliły zidentyfikować stan indukowany na granicy międzyfazowej $\text{Fe/MgAl}_2\text{O}_4$, prowadzący do przejścia fazowego w ultracienkich warstwach żelaza ze struktury przestrzennie centrowanej kubicznej, do struktury przestrzennie centrowanej tetragonalnej. Wyniki teoretyczne sugerują, iż optymalizacja podłoża może prowadzić do zwiększenia stabilności warstw żelaza oraz wzrostu energii anizotropii magnetokrystalicznej. W trzecim badaniu, analizując antyferromagnetyczne rozpraszanie Bragga w NiO i LaMnAsO , zastosowano metodę wieloprzekrojową (*multislice*) opartą na równaniu Pauliego w przybliżeniu przyosiowym (*paraxial*). Innowacyjne podejście obliczeniowe, uwzględniające efekty termiczne w układach magnetycznych, pozwoliło na pomyślne odtworzenie obserwacji eksperymentalnych dla NiO w temperaturze pokojowej. Badanie uwydatniło znaczenie optymalizacji parametrów eksperymentalnych w celu wykrycia antyferromagnetycznego rozpraszania Bragga w materiałach składających się z cięższych pierwiastków, które zwiększają termiczne rozpraszanie dyfuzyjne. Czwarta praca skupiła się na optymalizacji właściwości magnetycznych w stopie CeFe_{12} z metalami przejściowymi oraz atomami międzywęzłowymi. Wyniki ujawniły, że domieszkowanie takimi pierwiastkami jak Ti, Mn i W podnosi energię anizotropii magnetokrystalicznej, jednocześnie zmniejszając całkowity moment magnetyczny, co prowadzi do wartości twardości magnetycznej pozwalającej sklasyfikować te stopy jako magnetycznie twarde. Dalsze domieszkowanie atomami lekkimi, takimi jak B, C i N, dodatkowo poprawia twarde właściwości magnetyczne układów. Porównanie CeFe_{12} z LaFe_{12} ujawniło, że elektrony Ce $4f$ mają drugorzędny wpływ na wartość energii anizotropii magnetokrystalicznej.

Publications constituting the doctoral thesis

1. J. Snarski-Adamski, J. Rychły, and M. Werwiński, “Magnetic properties of $3d$, $4d$, and $5d$ transition-metal atomic monolayers in Fe/TM/Fe sandwiches: Systematic first-principles study,” *Journal of Magnetism and Magnetic Materials*, 546, 168828 (2022).
2. A. L. Ravensburg, M. Werwiński, J. Rychły-Gruszecka, J. Snarski-Adamski, A. El-sukova, P. O. Å. Persson, J. Ruzs, R. Brucas, B. Hjörvarsson, P. Svedlindh, G. K. Pálsson, and V. Kapaklis, “Boundary-induced phase in epitaxial iron layers,” *Physical Review Materials* 8, L081401 (2024).
3. J. Snarski-Adamski, A. Edström, P. Zeiger, José Ángel Castellanos-Reyes, Keenan Lyon, Mirosław Werwiński, Ján Ruzs, “Simulations of magnetic Bragg scattering in transmission electron microscopy,” *Ultramicroscopy*, 247, 113698 (2023).
4. J. Snarski-Adamski and M. Werwiński, “Effect of transition metal doping on magnetic hardness of CeFe_{12} -based compounds,” *Journal of Magnetism and Magnetic Materials*, 554, 169309 (2022).

Table of Contents

Acknowledgements	II
Abstract	III
Streszczenie	IV
1 Introduction	1
1.1 Magnetic materials	2
1.2 Magnetic thin films for spintronic application	3
1.3 Permanent magnets	4
2 Methodology	5
2.1 Density functional theory	5
2.1.1 Full-potential local-orbital code	6
2.1.2 Exchange-correlation potentials	7
2.1.3 Modeling of alloys	7
2.1.4 Magnetocrystalline anisotropy	8
2.1.5 Fixed spin moment calculations	9
2.2 Multislice method	10
2.2.1 Pauli multislice method	11
2.2.2 Magnetic vector potentials \mathbf{A} and magnetic field \mathbf{B}	12
2.2.3 Quantum excitation of phonons	13
3 Results	14
3.1 Magnetic properties of $3d$, $4d$, and $5d$ transition-metal atomic monolayers in Fe/TM/Fe sandwiches: Systematic first-principles study	14
3.2 Boundary-induced phase in epitaxial iron layers	15
3.3 Simulations of magnetic Bragg scattering in transmission electron microscopy	17
3.4 Effect of transition metal doping on magnetic hardness of CeFe_{12} -based compounds	18
4 Summary and conclusions	20

5 Publications constituting the doctoral thesis	22
Article: Magnetic properties of $3d$, $4d$, and $5d$ transition-metal atomic monolayers in Fe/TM/Fe sandwiches: Systematic first-principles study . . .	22
Article: Boundary-induced phase in epitaxial iron layers	27
Article: Simulations of magnetic Bragg scattering in transmission electron microscopy	49
Article: Effect of transition metal doping on magnetic hardness of CeFe_{12} -based compounds	56
Appendix	66
Searching for magnetically hard monoborides (and finding a few): A first- principles investigation	66
Magnetic hardness of hexagonal and orthorhombic Fe_3C , Co_3C , $(\text{Fe-Co})_3\text{C}$, and alloys with boron, nitrogen, and transition metals: A first-principles study .	67
About Author	68
Outlook	68
Bibliography	72

Chapter 1

Introduction

This thesis explores ways to control magnetic properties in transition metal-based materials, starting from thin films that are relevant to spintronic applications and ending with bulk materials, applicable as candidates for permanent magnets. Density functional theory (DFT) is used as a primary tool to investigate the fundamental magnetic properties of considered materials. Through systematic modeling, the thesis provides insight into how structural configurations and interactions with transition metals can influence magnetic characteristics. The dissertation consist of four primary studies, each addressing a distinct aspect of transition metal-based magnetic material properties. These studies can be organized along the thickness of the materials examined. The first two papers, according to the list *Publications constituting the doctoral thesis*, are focused on magnetic ultra-thin films within the thickness of single nanometers, the third paper discusses magnetic materials with a thickness of 100 nanometers, while the last article describes bulk magnetic materials. These publications provide a comprehensive study, giving a deeper understanding of the design of magnetic materials and showing possible paths for tailoring their properties to specific applications.

In this guide, I will present a brief introduction to the computational and analytical methods that were employed in the presented works. Specifically, I will discuss density functional theory (DFT) as one of the main approaches to electronic structure calculations and highlight its suitability for magnetic materials modeling. I will also introduce the multislice method, which is used in the third paper to simulate the interaction of electrons with magnetic materials in transmission electron microscopy (TEM), providing essential insights into magnetic phenomena related to antiferromagnetic phase.

In the dissertation, I would like to verify the following hypotheses:

1. spin magnetic moment dependence in sandwiches systems of bcc iron with monolayer of transition metals will be consistent with Slater-Pauling curve,
2. as the thickness changes, the ultra-thin iron (001) film shows inherent structural phase transition,

3. ultra-thin Fe (001) films with thickness above single atomic monolayer exhibit perpendicular magnetic anisotropy,
4. simulation of the magnetic Bragg scattering with incorporation of quantum excitation of phonons is computationally possible for 100 nm thick samples,
5. observation of antiferromagnetic Bragg spot in compounds with heavy elements is possible,
6. proper choice of the acceleration voltage for particular sample thickness is necessary to capture weak magnetic phenomenon related to the antiferromagnetic Bragg scattering,
7. $4f$ electrons are not required to exhibit magnetic hardness greater than unity in the ThMn_{12} structure,
8. the potential maximum MAE value for a given ferromagnetic material can be determined from the fully relativistic fixed spin moment calculations.

I contend that these hypotheses are substantiated by my dissertation.

1.1 Magnetic materials

Magnetism is an inherent characteristic of all matter, which arises from the magnetic moments of fundamental particles like protons, neutrons, and electrons. From all three, electrons exhibit the most significant magnetic moments, neglecting the contributions coming from others mentioned. Notably, the magnetic behavior is primarily influenced, according to Hund's principles, by the electrons in the outermost atomic orbitals. While the magnetic moments of inner shell electrons are compensated due to the Pauli exclusion principle, the outer shell electrons can retain an uncompensated magnetic moment, allowing atoms to exhibit magnetism. The Pauli exclusion states, that it is impossible for two fermions to occupy the same quantum state at the same time.

As the materials can exhibit different magnetic behaviors depending on their interaction with the external magnetic field, the universal phenomenon is diamagnetism, which occurs in all of the materials through a weak repulsion of that magnetic field. This means that magnetic susceptibility of diamagnetic material is less than or equal zero. Such an effect arises due to the fact that all electrons in a material are paired, which means that there is no net magnetic moment.

In contrast, materials with unpaired electrons can respond differently to the magnetic field. The magnetic moments of such materials with unpaired electrons tend to align with the external field, creating a net magnetic moment. Materials having the net magnetic moment only in the existence of the external field are called paramagnetic materials.

Certain materials exhibit stronger magnetic interactions, overcoming thermal fluctuations until the temperature limit, which is defined by Curie temperature for ferromagnetic

and ferrimagnetic materials. In contrast, for antiferromagnetic materials, this limit is defined by Néel temperature. In mentioned configurations, the ferromagnetic materials can be characterized by the alignment of the magnetic moments in the same direction. The antiferromagnetic materials have magnetic moments equal in magnitude, but oriented in the opposite directions. The last one from mentioned, ferrimagnetic materials have magnetic moments unequal and oppositely oriented. In this work, ferri-, ferro- and antiferromagnetic materials will be considered.

1.2 Magnetic thin films for spintronic application

In the modern electronics, the quest for smaller and faster devices with increased energy efficiency is gaining momentum, as its successor in the form of spintronics is emerging. The natural step forward is to engage electron spin as a carrier of information. The magnetic thin films are the heart of this revolution, and their unique properties may overcome the limitations of semiconductor-based technology. The main idea behind spintronics is the capability to manipulate the magnetic and spin-dependent properties of materials on tiny scales.

Magnetic thin films show an extraordinary capacity to control and manipulate the spins of electrons, making them perfect for the development of next-generation spintronic devices. Such thin films introduce new physical phenomena such as giant magnetoresistance (GMR) [1] or tunneling magnetoresistance (TMR), which serve as foundations of spintronic applications. Based on that, areas such as memory technologies, data storage, and sensor devices has improved. For example, one of the most common applications of TMR is in the magnetic tunnel junctions (MTJs) [2], which are a fundamental construction in the modern spintronics. Those junctions are made of two ferromagnetic layers separated by the insulating layer. Depending on the relative orientation of the magnetization in that junctions, we are able to control the tunneling of electrons through the insulating layer. This effect is sensitive to the magnetic state and has an application in the magnetic random access memory (MRAM) [3]. The improvement to the MRAM can go further with devices based on the spin-transfer torque (STT) [4], where spins of the electrons may be employed to manipulate the magnetization of the magnetic layers. Based on that, spin-transfer torque magnetic random access memory (STT-MRAM) [5] can be built. The STT-MRAM offers better and faster performance, less power consumption, and more resilience by storing data within the use of magnetic states – as opposed to electrical charges. Such an improvement can be made due to the use of the layers with perpendicular magnetic anisotropy (PMA), which plays a crucial role in spintronic devices like perpendicular magnetic anisotropy magnetic tunnel junctions (PMA-MTJ).

Despite the enormous potential of magnetic thin film applications, their integration into practical devices remains a major challenge. Concerns like interface quality, thermal stability, and magnetic anisotropy must be properly handled in order to maximize their potential. In this place, the density functional theory (DFT) is coming with help

as an essential tool in development of magnetic ultra-thin films, allowing to predict how electronic structure and magnetic properties will change within reduced thickness or interacting with other materials. The insights given by the DFT allows improving the efficiency of constructed devices.

1.3 Permanent magnets

While magnetic thin films have spintronic application, the bulk magnetic materials characterized as permanent magnets are essential parts in a variety of contemporary technologies, having a crucial function in devices depending on constant magnetic fields. Permanent magnets, unlike electromagnets, keep their magnetic properties with no need for external power sources, making them essential for energy-efficient applications. We can find them, for example, in electric motors and wind turbines. The demand for permanent magnets has been steadily raising due to the fast expansion of sectors like electric transportation and renewable energy [6, 7]. Efforts to reduce carbon emissions have further increased the need to develop high-performance magnets; in the best scenario, without the rare-earth content. Such increase in the demand poses huge challenges, particularly in the supply chain of rare-earth elements, due to their allocation on the globe.

Currently, the permanent magnets most commonly used in transport and energy production are based on neodymium (Nd) and samarium (Sm). The well known $\text{Nd}_2\text{Fe}_{14}\text{B}$ exhibits the magnetocrystalline anisotropy energy (MAE) of 4.9 MJ m^{-3} and magnetic hardness of 1.54 (dimensionless unit). The samarium-based magnets, such as SmCo_5 and $\text{Sm}_2\text{Co}_{17}\text{N}_3$, exhibit even higher of those values: MAE of 17 MJ m^{-3} and 8.9 MJ m^{-3} and magnetic hardness of 4.4 and 2.17, respectively [8]. However, they are more expensive than the Nd-based magnets. Sm-based magnets, due to their high Curie temperature, are used in higher-temperature applications.

Chapter 2

Methodology

In this chapter, I present a brief introduction to the methodologies that are employed to obtain the results discussed in the publications constituting the doctoral thesis. Across all investigations included in the dissertation, the core computational approach is based on density functional theory, which serves as the main framework for obtaining fundamental insights of the systems that are being studied. In the case of the study focusing on magnetic Bragg scattering, the methodology is likewise built upon the density functional theory calculations, enabling a detailed simulation of the scattering process. Such an approach provides a comprehensive understanding of the phenomena, capturing the complexity of the interactions of wavefunction with crystalline structures.

2.1 Density functional theory

Density functional theory (DFT) is a quantum mechanical method of investigating the electronic structure of solids and molecules [9]. DFT calculations are based on solving the Schrödinger equation applied to a many-electron system, with the electron density employed as the central variable [10, 11]. The many-body Schrödinger equation can be expressed in the non-relativistic time-independent form:

$$\hat{H}\Psi(r_1, r_2, \dots, r_N) = E\Psi(r_1, r_2, \dots, r_N), \quad (2.1)$$

where Ψ stands for the many-body wavefunction, N for number of electrons, E for total energy, and \hat{H} is the Hamiltonian operator defined as:

$$\hat{H} = \hat{T} + \hat{V}_{eke} + \hat{V}_{iee}, \quad (2.2)$$

where, \hat{T} describes electron's kinetic energy operator, \hat{V}_{eke} - interaction between nuclei and electrons potential operator, and \hat{V}_{iee} - interaction between electrons forming Coulomb repulsion. Meaning that, we can express total energy of the system as a functional $\rho(r)$ of

the electron density:

$$E[\rho] = T_{keni}[\rho] + \hat{V}_{eke}[\rho] + J[\rho] + E_{XC}[\rho], \quad (2.3)$$

where T_{keni} is defined as kinetic energy of non-interacting electron, $J[\rho]$ – Coulomb interaction between electrons, and $E_{XC}[\rho]$ – exchange-correlation energy.

The DFT is based on the Hohenberg-Kohn theorems, published in Physical Review journal in 1964. The theorems bring the existence of direct correlation between the ground state of electron density and external potential, and provide a principle stating that within minimizing the energy functional of electron density, we can obtain the true ground state energy of the considered system [12].

As the theorem mentioned above, which makes possible to solve the many-electron problem, the Kohn-Sham approach introduces a transformation into a set of single-electron equations. In this way, we obtain a set of self-consistent solutions of single-particle equations $\Psi_i(r)$:

$$\left[-\frac{\hbar^2}{2m} \nabla^2 + V_{eff}(r) \right] \Psi_i(r) = \epsilon_i \Psi_i(r), \quad (2.4)$$

where ϵ_i is an eigenvalue and V_{eff} is a sum of the potentials, giving the effective potential as follows:

$$V_{eff}(r) = V_{eke}(r) + V_{Hartree}(r) + V_{XC}(r). \quad (2.5)$$

In the above equation $V_{Hartree}(r)$ describe Hartree potential and $V_{XC}(r)$ exchange-correlation potential.

2.1.1 Full-potential local-orbital code

In this thesis, the full-potential local-orbital (FPLO) code plays a central role, as it forms the computational backbone of three out of the four studies constituting this dissertation. FPLO is a DFT code developed and customized for material science by a group from Leibniz Institute for Solid State and Materials Research, Dresden, led by Klaus Koepernik. From my perspective, the particular strength of this code, is to deal with magnetic materials, including transition metals and heavy elements [13, 14]. In this code, an all-electron full-potential method is employed, which means that no shape approximation is applied for charge density and potential. In FPLO, a localized basis set is used to calculate the electronic structure of the system. To optimize this process, the minimal basis set approach is used, reducing the number of applied basis functions to only those relevant, ensuring efficient computations without sacrificing accuracy. In such approach, functions for the valence electrons are included, and possibly some semi-core electrons functions, which may overlap with the valence states. This means that basis orbitals need to be properly tuned to the self-consistent potential.

2.1.2 Exchange-correlation potentials

The DFT calculation results depend on the choice of the exchange-correlation functional $E_{XC}[\rho]$ for which various approximations have been developed, such as local density approximation (LDA), generalized gradient approximation (GGA), and hybrid functionals.

LDA assumes that the $E_{XC}[\rho]$ depends only on the electron density at a given point in space, as in uniform electron gas. The strength of this approximation lies in its simplicity. The LDA typically underestimates the exchange-correlation energy, leading to underestimation of the bond lengths and overestimation of cohesive energies. The exchange-correlation energy for a given point is only dependent on the density value there, which can be written as:

$$E_{LDA}^{XC}[n \uparrow, n \downarrow] = \int d^3r \epsilon_{XC}^{UNIFORM}(n \uparrow, n \downarrow), \quad (2.6)$$

where $\epsilon_{XC}^{UNIFORM}$ represents the exchange-correlation energy in a uniform electron gas.

GGA improves LDA by introducing a gradient of electron density. Considering the density variation across space, GGA provides a more accurate description. The improved precision of GGA arises from a better way of capturing the effects of electron localization and exchange-correlation hole near the electron, making a significant difference in more complex environments [15]. Those improvements incorporated in Eq. 2.6 can be expressed as:

$$E_{GGA}^{XC}[n \uparrow, n \downarrow] = \int d^3r f(n \uparrow, n \downarrow, \nabla n \uparrow, \nabla n \downarrow). \quad (2.7)$$

The best known implementation of GGA is the PBE functional. The PBE acronym is formed of the initial letters of the surnames of John P. Perdew, Kieron Burke, and Matthias Ernzerhof, who in 1996 published the work entitled *Generalized gradient approximation made simple* [15]. This functional is build on the previous GGA version named PW91, authored by John P. Perdew and Yue Wang [16, 17]. PBE in the comparison to PW91 improved basic formulas, avoiding empirical fitting of parameters and using fundamental constants and precise exchange-correlation hole properties. Cessation from using numerical approach leads to smoother and more stable potentials.

2.1.3 Modeling of alloys

In my research, I have focused on modeling a diverse range of alloy systems with significant scientific and industrial relevance. This includes alloys of Fe/TM/Fe-sandwiches systems and CeFe_{12} with all 3d, 4d, and 5d transition metals. By investigating these materials with different alloy modeling schemes, I aimed to understand and predict their behavior under various conditions, contributing to the development of new materials. Understanding the properties of alloys often requires detailed techniques for modeling that can accurately capture their disordered and complex nature. Several computational approaches, each having their unique strength, can be employed to study such a system.

One of them is the virtual crystal approximation (VCA). It simplifies the problem of

dealing with random distributions of atoms by replacing the real disordered configuration with a virtual crystal consisting of virtual atoms. VCA involves replacing two types of atoms in an alloy with a single type of atoms with a fractional nuclear charge. This method is advantageous for the binary alloys of the elements with consecutive atomic numbers such as for FeCo alloys [18], providing approximate, yet insightful predictions of bulk properties. To address the limitations of the virtual crystal approximation, particularly for systems, where disordered and local atomic effects play a significant role, a more sophisticated approach can be employed in the form of a coherent potential approximation (CPA) [19] or supercell approach.

CPA accounts for disorder via an effective medium which represents the alloy's average potential, where each atom is considered with a coherent potential field. For magnetic systems CPA can be transformed into the disordered local moment (DLM) method [20], which allows modelling of the disordered paramagnetic state and determination of the Curie temperature.

The supercell method is a powerful approach with many degrees of freedom that need to be taken care of while constructing a large, periodic cell with multiple atomic sites representing local configurations explicitly. This method directly incorporates atomic arrangements, allowing for the substitution of a particular atomic site, and allowing detailed exploration of the local environment. Such approach is computationally expensive, nevertheless, it is sometimes necessary and beneficial to grasp details of considered phenomena.

Each of the mentioned methods has its advantages and disadvantages, and for a more comprehensive understanding, they can be employed parallel if computing power resources allow it.

2.1.4 Magnetocrystalline anisotropy

The magnetic properties of the material can differ for the specific crystallographic axes. Magnetocrystalline anisotropy energy (MAE) quantifies this difference as a difference in the energy between perpendicular orientations of the magnetic moments. The origin of MAE comes from the electron's spin-orbit coupling (SOC), which links the orientation of the electron's spin to its orbital motion and is influenced by the symmetry of the crystal. Atoms disrupt the symmetry of the electric field, breaking the isotropic nature of spin-orbit coupling. Such a disturbance introduces a directional preference of the magnetic moments alignment. This leads to the fact that a certain direction in the crystal is energetically more/less favorable, making natural alignment/anti-alignment of the magnetic moment along this direction. The magnetocrystalline anisotropy strength is influenced by factors like the symmetry of the crystal lattice, spin-orbit interaction and electronic structure. In the DFT studies, the spin-orbit coupling can be introduced to the system with the Hamiltonian through the terms described by the equation:

$$H_{SOC} = \xi LS \quad (2.8)$$

where ξ describes the constant of spin-orbit coupling that is proportional to the atomic number. L and S are the angular momentum of orbital and spin, respectively. In this context, the MAE is calculated for the systems with introduced spin-orbit coupling within the relativistic effects treated in FPLO code with full four component formalism from the equation:

$$\text{MAE} = E_{\text{HARD}} - E_{\text{EASY}}, \quad (2.9)$$

where E_{HARD} and E_{EASY} describes quantization axis with the highest and the lowest energy, respectively.

The calculation and interpretation of MAE are critical in understanding the preferred orientation of the magnetic moments. As I consider various crystallographic systems in the works forming this doctoral thesis, a consistent convention is employed, where MAE values can be either positive or negative, depending on the nature of the anisotropy. The positive value of MAE for bulk materials indicates uniaxial anisotropy, while for layer systems represents perpendicular anisotropy. The negative value of MAE in both cases describes *in-plane* anisotropy. Dealing with different symmetries of the crystallographic systems also influences the MAE interpretation, which for tetragonal and hexagonal structures is very simple. In those systems one axis (typically *c*-axis) is distinguished, so a positive MAE indicates the alignment of magnetic moments along that direction. The matter is getting complicated, while dealing with orthorhombic structures, where all three lattice parameters are non-equivalent, due to the lower symmetry. The MAE is therefore calculated as the difference between the direction with the lowest energy (easy axis) and the direction with the middle value of energy. This approach needs to be supplemented with an additional factor DE_{32} giving the comprehensive description of the anisotropy in orthorhombic systems. DE_{32} is described by me as an energy difference between the middle value of the energy and the direction with the highest energy (hard axis).

2.1.5 Fixed spin moment calculations

Regarding the determination of the magnetocrystalline anisotropy energy, it is worth mentioning the proposed suggestion in one of my works, to use fixed-spin moment (FSM) method to characterize this value in a given structure and composition properly. This method involves the change in the total spin magnetic moment of the system, making it possible to investigate how deviations from the equilibrium magnetic configuration influence all properties. Such an approach offers a powerful tool for exploring the relationship between the MAE and the spin magnetic moment of the material. As within basic DFT we are limited to 0 K calculations, the calculations for the equilibrium state with different exchange-correlation potentials are insufficient to properly predict thermal response of the material on MAE value. As we want our material to work in temperature above room temperature, it is important to show dependence of the MAE on the magnetic moment, as we know that increase in temperature will affect the magnetic moment value. The FSM calculations imposes the total spin magnetic moment per unit cell, giving hints for the

further modification of the composition to optimize the magnetic parameters in such a way that at room temperature, observed magnetic hardness and MAE will be the highest possible. As there is a difference in the equilibrium calculations for the different exchange-correlation functionals, the FSM calculations for each of them show an underlying relation between spin polarization and MAE. I have also demonstrated, that the significant advantage of this method lies in its independence from the choice of the exchange-correlation potential, giving reliable predictions and showing if there is a possibility to improve the magnetic parameters in the structure under consideration.

2.2 Multislice method

Multislice method [21] is a powerful computational approach for simulating the behavior of electrons interacting with condensed matter in transmission electron microscopy (TEM) [22–26].

TEM imaging can be split into four main parts: electron source, electron-specimen interaction, optics, and detector. While modeling those phenomena separately, we need to use our models within a consistent framework. The first assumption is the fact that only imaging electrons are treated as a time harmonic wave within quantum-mechanical principles. This wave function is described by equation:

$$\Psi(x, t) = \psi(x) \exp(-iEt/\hbar), \quad (2.10)$$

where E is the energy of the emitted electron. In TEM imaging, to achieve coherent illumination, the electrons after being emitted from the electron gun need to pass through the condenser aperture. It can be assumed that such electrons can be treated as a monochromatic plane wave, which allow us to describe them with the following relation:

$$\Psi(x, t) = \exp(ikx) \exp(-iEt/\hbar), \quad (2.11)$$

where the optical axis of the TEM is parallel to the direction of propagation ω , k is a wave number, which is expressed as $k = \frac{2\pi}{\lambda}$ and λ is a wavelength. However, in real experiment the illumination is not perfectly coherent, and this partial incoherence can be modelled as envelope functions.

To computationally introduce the model of the specimen, the Hamiltonian of interaction V should be calculated for the considered sample using the equation:

$$V(x) = \sum_i V_{Zi}(x - x_i), \quad (2.12)$$

where V_Z represent an electrostatic potential of an isolated atom at the position x_i with

atomic number Z . Equation 2.12 can be expressed as:

$$V_Z(x - x_0) = \frac{1}{4\pi\epsilon_0} \left[\int_{\mathbb{R}^3} \frac{\rho(y)}{|x - y|} dy - \frac{eZ}{|x - x_0|} \right], \quad (2.13)$$

where $\rho(y)$ stand for function of electron density, which are associated to the isolated atom shell electrons, y represents the position vector in the three-dimensional space and ϵ_0 stand for vacuum permittivity. In the specimen, the isolated atoms consist of the positively charged nuclei surrounded by the negatively charged electrons. The incoming electron scattered on the specimen can be described by Schrödinger equation:

$$i\hbar \frac{\partial}{\partial t} \Psi(x, t) = \left[-\frac{\hbar^2}{2m} + V(x) \right] \Psi(x, t), \quad (2.14)$$

where m is the relativistic mass of the electron.

The effects of the microscope optics are also implemented in the simulations. They describe how the system of lenses affects the electron wavefunction, including defocus and spherical aberration. The defocus causes a quadratic phasing effect in the Fourier space changing the wavefunction along the equation:

$$\Psi_{DEFOCUS}(x, y) = \mathcal{F}^{-1} \left(\mathcal{F}\Psi(x, y) \exp \left(i \frac{\pi \lambda \Delta f (u^2 + v^2)}{2} \right) \right), \quad (2.15)$$

where \mathcal{F}^{-1} and \mathcal{F} describe the inverse and normal Fourier transform, respectively, u and v are spatial frequencies coordinates in the Fourier space, and Δf is the value of defocus. The spherical aberration is introduced giving higher order phase distortion, and the phase factor can be expressed as:

$$\Psi_{C_S}(x, y) = \mathcal{F}^{-1} \left(\mathcal{F}\Psi(x, y) \exp \left(i \frac{\pi C_S (u^2 + v^2)^2}{\lambda} \right) \right), \quad (2.16)$$

where C_S stands for spherical aberration. We neglect any detector-specific effects in the simulations, because we focus on the interaction of electrons with the sample and not on improving the detection components.

2.2.1 Pauli multislice method

Having discussed the standard multislice method, I will now present a correction and extension of this method, called Pauli multislice method, that allow modeling magnetic systems and their interaction with incoming electrons.

The Pauli multislice method extend the conventional multislice scheme incorporating magnetic interactions, which are essential to properly describe magnetic materials [27]. It is stemming from the paraxial approximation applied to the Pauli equation, which describes the motion of an electron in electric and magnetic fields. The paraxial approxi-

mation to the Pauli equation can be expressed as:

$$\frac{\partial \Psi}{\partial z} = \frac{im}{\hbar} (\hbar k + eA_z)^{-1} \left\{ \frac{\hbar^2 \nabla_{xy}^2}{2m} + \frac{ie\hbar}{m} \mathbf{A}_{xy} \nabla_{xy} - \frac{\hbar k e A_z}{m} - \frac{e\hbar}{2m} \sigma \mathbf{B} + eV \right\} \Psi, \quad (2.17)$$

where the Ψ wave function includes components of both spins, up and down, called Pauli spinor, ∇_{xy} stands for the in-plane gradient operator, and V is the electrostatic potential. The included paraxial approximation assumes that the electron beam is predominantly traveling in the direction perpendicular to the sample surface (z-axis) and any kind of deviations are rather small, meaning that the term $\frac{\hbar k e A_z}{m}$ makes the biggest contribution owing to magnetism. In the Pauli multislice method, the electron wavefunction is propagated as in traditional multislice, slice by slice though the crystal.

2.2.2 Magnetic vector potentials \mathbf{A} and magnetic field \mathbf{B}

As it is crucial to incorporate magnetic interaction into simulations of TEM to properly analyze magnetic materials, the magnetic vector potentials (\mathbf{A}) and magnetic fields (\mathbf{B}) are parameterized, in the described method, based on DFT calculations. Since magnetic interactions are much weaker than the dominant Coulomb forces, modeling them with high accuracy using *ab initio* calculations is computationally demanding. Therefore, parameterizing these interactions is necessary to obtain results within a reasonable time-frame. The magnetic responses of elements with atomic number starting from $Z = 21$ (Sc) and ending at $Z = 79$ (Au) were pre-computed using DFT and applied to large-scale systems.

Simulations of the electron beam scattered in the magnetic materials need to consider the interaction of the electron's spin not only with the Coulomb potentials, but also with the magnetic vector potential. The relation of the magnetic field $\mathbf{B}(r)$ and magnetic vector potential $\mathbf{A}(r)$ is well known from the Maxwell's equation:

$$\mathbf{B}(r) = \nabla \times \mathbf{A}(r). \quad (2.18)$$

As the magnetization $\mathbf{M}(r)$ is generated by the spin density distribution, which from Ampere's law can correlate both magnetic field and vector potential, the following equations need to be solved:

$$\mathbf{M}(r) = -\mu_B \langle s(r) \rangle; \quad (2.19)$$

$$\nabla \times \mathbf{B}(r) = \mu_0 J_{spin}(r). \quad (2.20)$$

The spin density $\rho_s(r)$ obtained from the DFT calculations is expressed as the $\langle s(r) \rangle$, which is the spin expectation value at given position r , while spin current $J_{spin}(r)$ is derived from the magnetization $\mathbf{M}(r)$ by solving Maxwell's equations in the Coulomb gauge condition, which means that $\nabla \cdot \mathbf{A} = 0$.

Overcoming the computational challenges of directly solving both the magnetic field

and magnetic vector potentials for each atom can be achieved using a parameterization approach. In this approach, a quasi-dipole model approximates the magnetic field around every atom. Such an approximation is inspired by the classical dipole field extended by the modification in order to take into account the complexity of atomic spin distributions in crystals. In the mentioned quasi-dipole approximation, the magnetic vector potential $\mathbf{A}(r)$ is represented by the following form:

$$\mathbf{A}(r) = (\bar{m}_m \times r) \sum_{i=0}^4 \frac{a_i}{r^{n(i)} + b_i}, \quad (2.21)$$

where \bar{m}_m describes the unity vector along the direction of the atomic magnetic moment and $n(i) = i/2 + 3$ expresses the radial dependence. The b_i coefficients in above equation smooth out the classical dipole's short-range behavior, while the a_i adjust the field's strength throughout space. Due to Eq. 2.18 we can express \mathbf{B} in the following form:

$$\mathbf{B} = \sum_{i=0}^4 a_i \frac{n(i)(r\bar{m}_m)r^{n(i)-2}r + [2b_i - (n(i) - 2)r^{n(i)}]\bar{m}_m}{[r^{n(i)} + b_i]^2}. \quad (2.22)$$

2.2.3 Quantum excitation of phonons

Quantized vibration of atoms plays a fundamental role in the determination of the physical properties of materials such as thermal, magnetic and electrical behavior. Those vibrations in the crystal lattice, called phonons, have a huge impact on the simulation of the transmission electron microscopy (TEM). They can be observed particularly through the feature known as Kikuchi bands, which arise due to electron-phonon interaction [28, 29]. This makes TEM a powerful method to explore the quantum excitation of phonons in the real materials. This paragraph explains the basics of the phonon excitation implemented in the code. As atoms are arranged in the crystal in a periodic lattice, and the vibrations of the atoms take place around their equilibrium positions, they are classically treated as waves propagating through the lattice. The quantum mechanics nevertheless imposes the restriction limiting existence of phonons at specific energy level. The energy of each phonon can be described with the following equation:

$$E_n = \left(n + \frac{1}{2}\right) \hbar\omega, \quad (2.23)$$

where n stands for the number of phonons in the specific vibrational mode and ω is the frequency of lattice vibration [30].

In transmission electron microscopy experiments, high-energy electrons pass through a sample, scattering on the lattice. To simulate a different configuration of these interactions, the final diffraction pattern is an average of hundreds of possible placements of the atom within the random distribution of the mean squared displacement described for specific atoms at a given temperature.

Chapter 3

Results

In the series of four papers constituting this dissertation, I present results for a full range of material thicknesses – from a single atomic monolayer to a solid crystal. The first two papers on the list discuss ultrathin layered systems with thicknesses ranging from a single atomic monolayer to about 2 nm (dozen monolayers), the third paper addresses films with the thickness on the order of 100 nm, while the last paper deals with bulk materials. In the following section, I will introduce the main concepts, results, and conclusions of each of the mentioned publications.

3.1 Magnetic properties of $3d$, $4d$, and $5d$ transition-metal atomic monolayers in Fe/TM/Fe sandwiches: Systematic first-principles study

In a publication entitled *Magnetic properties of $3d$, $4d$, and $5d$ transition-metal atomic monolayers in Fe/TM/Fe sandwiches: Systematic first-principles study*, I have conducted a comprehensive investigation using first-principles calculations of the Fe-based sandwich system. The main objective of this study was to explore how the atomic monolayer of transition metal (TM) influences the magnetic characteristics of the heterostructure, while introduced into the bulk Fe bcc. That research was driven by increased interest in the thin films and magnetic multilayer systems within application in the spintronics devices.

In my model, the transition metal monolayer was inserted between Fe layers. The Fe layers represent the bulk Fe-bcc. For series of $3d$, $4d$ and $5d$ transition-metal monolayers, I have systematically computed magnetic characteristics such as: spin and orbital magnetic moments and magnetocrystalline anisotropy energy. The main focus I have put on understanding how the TM monolayers modify the magnetic behavior at the interface of sandwich systems.

The study revealed a wider range of magnetocrystalline anisotropy energy (MAE) values for $5d$ elements than for $3d$ or $4d$ elements. The highest values of perpendicular magnetic anisotropy were obtained for the systems with Pt and W monolayers. The

highest values of in-plane magnetic anisotropy were also obtained for the elements from 5d series, Lu and Ir. The achieved high value of perpendicular anisotropy for the system with Pt is consistent with observations in the L1₀ FePt compound, which is known for the outstanding magnetic properties [31].

For total spin magnetic moment, we observe clear trends in which most of the transition-metal elements lower its value, while the Co and Ni slightly increase it. This growth can be explained within the framework of the Slater-Pauling curve described for metal alloys in which there is an interaction of the valence electrons of Fe and the *d* shell of the transition-metal monolayer. Looking at the orbital magnetic moment, the Pt monolayer also stands out, which is correlated with the enhanced MAE.

Exploring values of spin magnetic moment and charge density in the direction perpendicular to the Pt monolayer, I have found oscillations in both quantities. The three monolayers of Fe atoms on each side of the Pt monolayer exhibit an increase in the spin magnetic moment, from bulk value 2.16 μ_B up to 2.76 μ_B for the first Fe monolayer counting from the Pt monolayer, demonstrating localized influence of the transition metals in the system.

In densities of states of systems with Ag, Pd, Ir, Pt and Au, I have observed the van Hove singularity at the Fermi level. Such a state can significantly affect electrochemical properties of the system and also is crucial in spintronic devices, increasing efficiency in spin-polarized transport [32]. A van Hove singularity occurring at the Fermi level can enhance spin-polarized tunneling due to higher availability of spin-polarized states making such Fe/TM/Fe systems particularly attractive for use in spin-transfer torque memory or magnetic tunnel junctions, taking into account the fact that van Hove singularity also affect magnetoresistance [33].

Concluding, my research offers valuable insights for designing magnetic multilayers for application in magnetic storage, magnetoresistive devices, and spintronics.

3.2 Boundary-induced phase in epitaxial iron layers

The paper entitled *Boundary-induced phase in epitaxial iron layers* shows combined theoretical and experimental investigations of the structural and magnetic properties of iron thin films. The following methods and measuring devices were used: X-ray reflectometry (XRR), X-ray diffraction (XRD), longitudinal (L-) and polar (P-) magneto-optical Kerr effect (MOKE), superconducting quantum interference device (SQUID), atomic force microscopy (AFM), and high-angular annular dark field scanning transmission electron microscopy (HAADF-STEM). I did not participate in the experimental work for this study, but I have performed the DFT calculations included in the work. The study is presented in the form of a letter, with a single DFT result incorporated into the main text and additional DFT results provided in the supplementary material.

The performed DFT calculations focused on modeling bcc Fe (001) thin films with the thickness in the range from a single monolayer to twelve monolayers. The model was

constructed as a slab, which means that the Fe film was surrounded by vacuum. Full optimizations of the lattice parameters and Wyckoff positions were performed, allowing to observe the phase transition within change of the sample thickness. For a freestanding Fe films, a critical thickness of 9 monolayers was found, below which body centered tetragonal (bct) structure with a high c/a ratio is preferred. The lattice parameter c was found to increase with decreasing number of monolayers.

As in the experiment the Fe layers were epitaxially produced on the MgAl_2O_4 (001) substrate, the corresponding calculations were performed for the fixed lattice parameter a equal to 2.8 \AA reflecting the property of the substrate. Those results shown in the paper are in an excellent agreement with the lattice parameters measured experimentally.

In the article, we present a comparison of the structural analysis of the asymmetric reflections of the Bragg peaks Fe (002) and (112) measured experimentally and the change in the lattice parameter c for fixed parameters a calculated within the DFT framework. Both presented results are consistent in their essence and clearly indicate that Fe bct structure of ultra-thin films can be stabilized through epitaxial deposition and this distortion is not induced by strain.

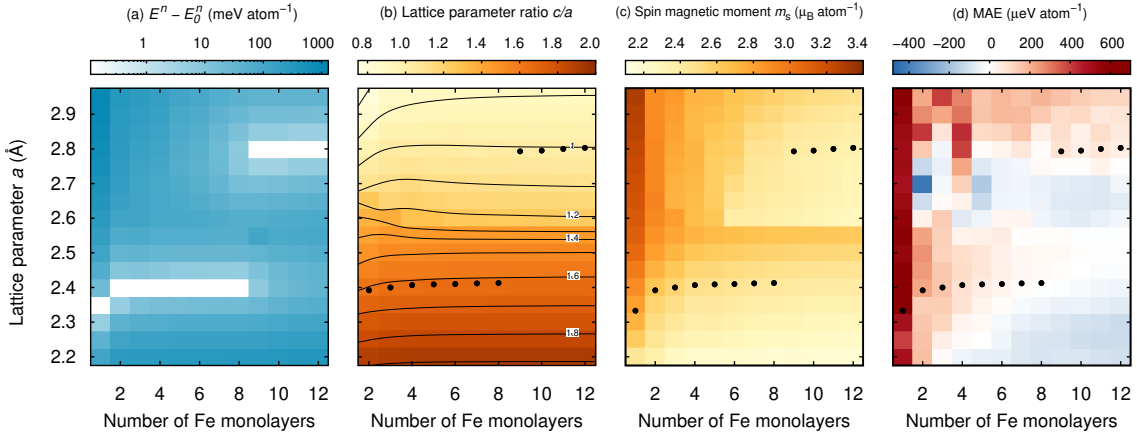


Figure 3.1: Structural and magnetic characteristics of Fe thin films as a function of the square lattice parameter a and the number of Fe monolayers. (a) The logarithmic scale is used to display the total energies of Fe thin films with n monolayers (E^n) shifted to the lowest energy of each slab (E_0^n); (b) lattice parameter ratio c/a ; (c) total spin magnetic moments expressed in Bohr magnetons per atom; and (d) magnetocrystalline anisotropy energy. Equilibrium solutions are shown by full circles.

Since only part of the DFT results were shown in the published letter and supplementary materials, I would like to present some more data obtained. Since in the publication, most of the results are presented for the fixed lattice parameter a , here I show the results for the freestanding Fe (001) films with optimized parameter a .

For tetragonal films (with $c/a \sim 1.6$) the equilibrium lattice parameter a is much lower ($\sim 2.40 \text{ \AA}$) than the lattice parameter of MgAl_2O_4 (001), see Figs. 3.1(a,b). As Fig. 3.1(c) shows, the magnetic moment per atom increases within the decrease of the film thickness. The value of the magnetic moment for the bulk bcc Fe equals $2.16 \mu_B$ is increased up to

$2.8 \mu_B$ for the single Fe monolayer. From Fig. 3.1(d) we can extract information about the highest values of the magnetocrystalline anisotropy energy (MAE) that can be obtained for the single Fe layer, but also for the 4 monolayers with the lattice parameter 2.8 \AA , which is a similar value as the lattice parameter of MgAl_2O_4 (001) used in the experiment as a substrate.

3.3 Simulations of magnetic Bragg scattering in transmission electron microscopy

In the paper entitled *Simulations of magnetic Bragg scattering in transmission electron microscopy*, I have explored the occurrence of magnetic Bragg scattering in antiferromagnetic compounds using as an example NiO and LaMnAsO. The primary goal of this work was to simulate the magnetic Bragg reflection, which is a very subtle phenomenon that arises when a transmission electron microscope is used to study antiferromagnetic materials. This weak type of scattering had been previously observed experimentally by J.C Loundon in 2012, studying NiO [34].

My aim was to computationally reproduce those results for NiO, as well as extend the investigation for more complex system with heavier elements. Additionally, the goal was to better understand how experimental parameters such as sample thickness and electron acceleration voltage, temperature and presence of phonons affect the visibility of antiferromagnetic Bragg spots.

To perform such calculations, I have utilized the multislice method based on the Pauli equation, to simulate the interaction of the incoming electron beam with the magnetic and electrostatic potentials in considered materials. Applied method allows for detailed modeling of both magnetic and non-magnetic scattering processes in TEM, with and without introducing phonons into the system. The introduction of phonons has been applied within the framework of the quantum excitation of phonons (QEP) method. According to that, we can distinguish in this paper two approaches. The first one is the static model calculations, where all atoms are considered as static, and the second one, which includes the vibration of the atoms and thermal diffuse scattering.

For NiO, my simulations successfully reproduced the antiferromagnetic Bragg spot observed experimentally by J.C. Loundon. The calculations showed that the magnetic Bragg reflection in NiO is much stronger than thermal diffuse scattering background at room temperature, particularly for higher acceleration voltages. This result confirmed the experimental finding that magnetic Bragg scattering can be observed with use of transmission electron microscopy, even at room temperature.

As the LaMnAsO contains heavier elements such as La and As, the thermal diffuse scattering in the room temperature is overcoming magnetic Bragg scattering, making antiferromagnetic Bragg spot indistinguishable. So, to make it identifiable, I have also explored calculations for the smaller mean squared displacement equivalent of approximately 30 K.

At lower temperature, the antiferromagnetic Bragg spot became more visible suggesting that low-temperature experiments or extended data acquisition time would be obligatory to detect magnetic scattering in LaMnAsO.

Magnetic Bragg scattering in antiferromagnetic materials occurs when the scattering vector matches the periodicity of the magnetic structure. The intensity of this scattering is typically weak and due to being masked by stronger non-magnetic scattering phenomena it may not always be distinguishable. My work showed that adjusting experimental conditions such as acceleration voltage of the incoming beam, sample thickness and temperature can enhance magnetic signal detection. In both of the considered cases, optimal acceleration voltage was found to be around 300 kV in terms of detection of the antiferromagnetic Bragg spot.

To conclude, the presented study provides insight into the factors that influence the visibility of the magnetic Bragg scattering in transmission electron microscopy. This study also advances the use of TEM in exploring magnetic phenomena and opens new possibilities for examining antiferromagnetic materials for spintronic applications.

3.4 Effect of transition metal doping on magnetic hardness of CeFe₁₂-based compounds

In a paper entitled *Effect of transition metal doping on magnetic hardness of CeFe₁₂-based compounds*, I investigated influence of transition metal doping on the magnetic hardness and magnetocrystalline anisotropy energy. As the Lanthanum and Cerium content in rare-earth ores are much higher than neodymium or samarium, and at the same time much cheaper, interest in these elements as ingredients of permanent magnets is emerging.

The density functional theory was employed to determine the magnetic properties of CeFe₁₂-based compounds alloyed with 3d, 4d, and 5d transition metal elements in both “1-11-1” and “1-10-2” compositions. All the d-element substitutions were placed at Fe sites.

The CeFe₁₁Ti was considered as a benchmark alloy, well known experimentally for its uniaxial magnetocrystalline anisotropy and stable ThMn₁₂-type structure. MAE was calculated for a number of other compositions, which made it possible to identify materials with improved magnetic properties. Especially, the CeFe₁₁Re and CeFe₁₀W₂ alloys display the highest magnetic hardness and MAE. Fixed spin moment (FSM) calculations show strong correlation between the MAE and spin magnetic moment. The correlation between FSM and the choice of exchange-correlation functionals emerges as a critical factor in accurately describing MAE.

In the article, I also analyze the effects of substituting cerium by lanthanum, which help to understand the role of the 4f electrons in the considered (Ce/La)Fe₁₂ system. The comparison of CeFe₁₂ with selected La compounds such as LaFe₁₂, LaFe₁₁Ti, and LaFe₁₀W₂ shows that 4f electrons have secondary effect on the magnetic anisotropy and

the dominant contribution to the MAE comes from the Fe atoms. A challenge that emerged from presented studies was the chemical instability of some proposed new candidates for CeFe₁₂-based new permanent magnets, particularly those with W and Mo. Further alloying with other rare earth elements or the use of interstitial doping with light atoms such as B, C, N or H could not only stabilize the structure, but also improve the magnetic properties of the systems. Calculations for CeFe₁₂N and CeFe₁₁TiN have shown that nitrogen alloying enables further improvements in MAE and magnetic hardness.

This work contributes to the ongoing effort to develop an economically feasible new generation of permanent magnets.

Chapter 4

Summary and conclusions

Each of the four publications presented in this thesis focused on different aspects of the magnetic materials based on transition metal elements, employing advanced computational techniques to explore their magnetic properties.

The first study involved a heterostructure with an atomic monolayer of transition metal embedded in a bulk bcc iron. The results demonstrated that most of the transition metal monolayers, except Co and Ni, reduce the total spin magnetic moment of the system, which is consistent with the Slater-Pauling curve. Strong perpendicular magnetic anisotropy was observed for the Pt and W, while Lu and Ir monolayers favored the *in-plane* magnetic anisotropy. The behavior of the magnetic moment and charge density along the z direction of the model (perpendicular to the interface) showed oscillations in both values. This fact emphasizes the influence of the monolayer on electronic properties of the system. Furthermore, for cases with monolayers of Ag, Pd, Pt, Ir, and Au, the van Hove singularities at the interface were identified, highlighting the role of the interface in modifying electronic and magnetic properties of the heterostructure.

The second study investigated the magnetic properties of Fe ultra-thin films deposited on a substrate MgAl_2O_4 with a surface (001). From the experiment, a boundary-induced state was identified in Fe layers, which is attributed to the proximity effect at the Fe/ MgAl_2O_4 interface. This effect led to the rotation of the easy axis in the body centered tetragonal Fe phase by $\pi/4$ compared to the bulk bcc Fe. This reorientation significantly influences the magnetocrystalline anisotropy, particularly as a function of the thickness. The DFT findings contribute to the understanding and optimization of Fe films for use in the heterostructures and with potential applications in magnetic tunnel junctions. The DFT calculations also suggest the use of another substrate with the surface square lattice parameter close to the equilibrium value of the ultrathin bcc Fe film, which is around 2.4 Å.

In the third study, multislice simulations based on the paraxial Pauli equation were employed to explore the diffraction patterns in two antiferromagnetic materials, LaMnAsO and NiO . Performed simulations successfully reproduced the experimental observations of the antiferromagnetic Bragg spots in NiO at room temperature, which were introduced to

the system via quantum excitation of phonons. The simulations confirmed that this unique magnetic phenomenon in NiO is significantly stronger than thermal diffuse scattering. In contrast, for LaMnAsO, the presence of heavier elements, and consequently much stronger thermal diffuse scattering, hindered the detection of antiferromagnetic Bragg spots at room temperature. The study highlighted the importance of optimizing experimental parameters such as acceleration voltage and reduction of temperature to achieve reliable detection of these subtle magnetic phenomena.

The fourth study focused on the bulk CeFe_{12} alloyed with transition metals. The work examined the effects of alloying on the magnetic properties, with the purpose of finding the highest MAE and magnetic hardness in the considered alloys. I have found that an increase of Ti concentration in $\text{CeFe}_{12-x}\text{Ti}_x$ reduces the total magnetic moment, significantly enhancing both MAE and magnetic hardness. A similar trend was observed for doping with Mn and W. Interstitial doping with light atoms such as B, C, and N showed the additional ability to tailor those values. Performed studies comparing LaFe_{12} and CeFe_{12} revealed that the Ce $4f$ electrons in the ThMn_{12} structure have secondary impact on the MAE.

Overall, the publications being a part of this thesis provide a comprehensive investigation of the magnetic properties of materials. The results improve the understanding of the interplay between structural, electronic, and magnetic properties, offering insights into better understand the design of advanced materials for spintronic and permanent magnet applications.

Chapter 5

Publications constituting the doctoral thesis

The publications composing this dissertation are attached below.



Magnetic properties of 3d, 4d, and 5d transition-metal atomic monolayers in Fe/TM/Fe sandwiches: Systematic first-principles study

Justyn Snarski-Adamski^{*}, Justyna Rychły, Mirosław Werwiński

Institute of Molecular Physics, Polish Academy of Sciences, M. Smoluchowskiego 17, 60-179 Poznań, Poland

ARTICLE INFO

Keywords:

Magnetocrystalline anisotropy energy
FPLO
DFT
First-principles calculations

ABSTRACT

Previous studies have accurately determined the effect of transition metal point defects on the properties of bcc iron. The magnetic properties of transition metal monolayers on the iron surfaces have been studied equally intensively. In this work, we investigated the magnetic properties of the 3d, 4d, and 5d transition-metal (TM) atomic monolayers in Fe/TM/Fe sandwiches using the full-potential local-orbital (FPLO) scheme of density functional theory. We prepared models of Fe/TM/Fe structures using the supercell method. We selected the total thickness of our system so that the Fe atomic layers furthest from the TM layer exhibit bulk iron-bcc properties. Along the direction perpendicular to the TM layer, we observe oscillations of spin and charge density. For Pt and W we obtained the largest values of perpendicular magnetocrystalline anisotropy and for Lu and Ir the largest values of in-plane magnetocrystalline anisotropy. All TM layers, except Co and Ni, reduce the total spin magnetic moment in the generated models, which is in good agreement with the Slater-Pauling curve. Density of states calculations showed that for Ag, Pd, Ir, and Au monolayers, a distinct van Hove singularity associated with TM/Fe interface can be observed at the Fermi level.

1. Introduction

Over the past decades, the magnetic thin films and layered structures have attracted considerable attention in theoretical and applied physics [1]. These systems exhibit novel physical phenomena such as enhanced magnetic moments and magnetocrystalline anisotropy energy (MAE), oscillatory interlayer coupling, and spin- and charge-density waves [2,3]. These quantum phenomena related to magnetism and spin-orbit coupling are also the subject of interest in spintronics. An important example of a spintronic device is the spin-transfer torque memory, which uses a spin-polarized tunneling current to switch magnetization [4]. Although there is huge potential in creating magnetic multilayer structures, their control is difficult. Moreover, controlling and growing clean and sharp interfaces requires a large amount of labor and knowledge. Previous studies have predicted strong effects of 3d transition-metal (TM) monolayers on ferromagnetic moments of metallic overlayers [5,6] or sandwich bilayers [7]. For the systems considering the sandwich model with Mn bilayers, oscillations of spin magnetic moments were observed [7]. The magnetic properties of 3d TM on metallic substrates such as Pd(001) and Ag(001) show great similarity to the interactions of 3d magnetic impurities in bulk alloys [8]. For 4d and 5d monolayer on Ag(001) and Au(001) substrates, the magnetism has been explained as effect of two-dimensional band structure [9]. An exceptionally large perpendicular magnetocrystalline anisotropy

was found for Ir monolayer capped on Fe(001) surface [10]. There has also been interest in forcing ferromagnetic coupling in rare-earth metal/Fe sandwich systems using 3d elements, which allow obtaining huge magnetic moments of the order of $10 \mu_B$ /rare-earth atom [11,12]. Furthermore, the ferromagnetic coupling in the Fe/TM/Gd sandwich system with 4d and 5d metal spacers was found to be stronger than that with 3d spacers [13].

In this work, we focused on the systems consisting of a Fe-bcc matrix and a transition metal monolayer, see Fig. 1.

2. Computational details

In this paper, the results of computations performed in the framework of density functional theory (DFT) are presented. The models of 3d, 4d, and 5d transition-metal atomic monolayers in Fe/TM/Fe sandwiches were investigated using the full-potential local-orbital scheme (FPLO18.00-52) [14,15]. To model the systems, we used the supercell method [16]. The structural parameters of our models are $a = b = 2.83 \text{ \AA}$ and $c = 31.13 \text{ \AA}$. The generalized gradient approximation (GGA) in the Perdew–Burke–Ernzerhof (PBE) form [17] was used. The lattice parameters were set as for bulk Fe-bcc and multiply 11 times in the c -direction, whereas the Wyckoff positions were optimized for each

^{*} Corresponding author.

E-mail address: justyn.snarski-adamski@ifmpan.poznan.pl (J. Snarski-Adamski).

<https://doi.org/10.1016/j.jmmm.2021.168828>

Received 8 July 2021; Received in revised form 4 November 2021; Accepted 8 November 2021

Available online 27 November 2021

0304-8853/© 2021 The Authors. Published by Elsevier B.V. This is an open access article under the CC BY license (<http://creativecommons.org/licenses/by/4.0/>).

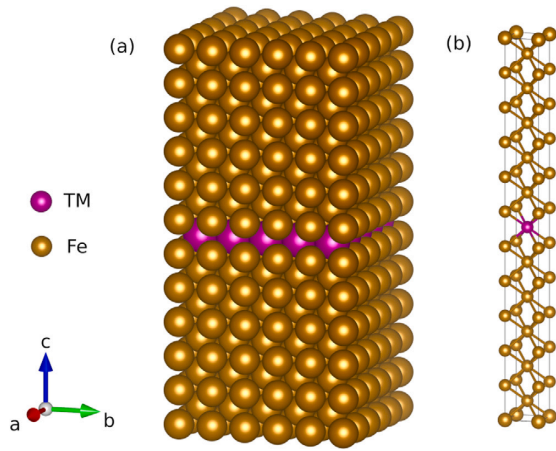


Fig. 1. A model of the crystal structure of the Fe/TM/Fe-sandwich system which crystallizes in a tetragonal structure [space group $P4/mmm$ (No. 123), $a = b = 2.83$ Å and $c = 31.13$ Å]. (a) Model showing the periodic multiplication of the unit cell, which is the subject of our consideration. (b) Unit cell of the Fe/TM/Fe-sandwich system.

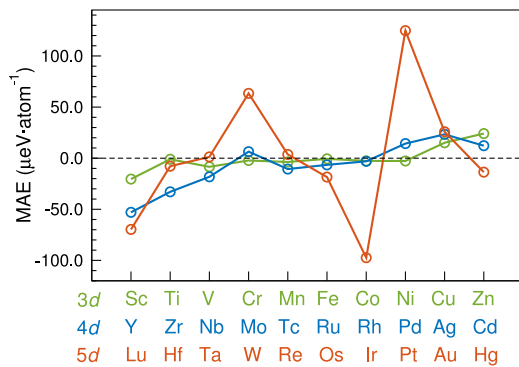


Fig. 2. Magnetocrystalline anisotropy energy (MAE) of Fe/TM/Fe-sandwiches for various 3d, 4d, and 5d transition metal (TM) elements. Calculations were performed with the FPLO18 using the PBE functional and supercell model. Considered unit cell include 21 atoms of Fe and 1 atom of TM.

considered system using a spin-polarized scalar-relativistic approach, see Fig. 1. The substitution of TM element was intended to create a single dopant monolayer in the center of this structure. Our calculation did not include optimization of lattice parameters. In order to validate the approximation taken under consideration, in which we assume no change in the lattice parameters in the presented model, we have conducted full optimization for the Fe/Pt/Fe case and thus determined the accuracy of our MAE calculations in the range of 7%. A $12 \times 12 \times 1$ k -mesh was used for atomic positions optimization and accuracy of forces was set as 10^{-3} eV Å $^{-1}$. An $80 \times 80 \times 10$ k -mesh was found to lead to well converged results of the magnetocrystalline anisotropy energies (MAE). The convergence criterion for the charge density was set as 10^{-6} . MAE was evaluated as a difference between the fully-relativistic total energies calculated for quantization axes [100] and [001]. The applied full-potential approach plays an important role in the accurate determination of the values of magnetic moments and MAE [18]. The VESTA code was used to visualize the crystal structure [19].

3. Results and discussion

Since we considered all 3d, 4d, and 5d transition metals in Fe/TM/Fe-sandwich models, we obtained a complete picture of the variations of MAE, total spin magnetic moment, and magnetic moments on TM, see Figs. 2, 3a, 3b, and 3c. We see that 5d elements can lead to a more extreme MAE than the 3d and 4d elements due to the stronger spin-orbit coupling. Positive and negative MAE values indicate alignment of magnetic moments perpendicular and in-plane of the TM layer, respectively. For Pt and W we obtained the largest values of perpendicular magnetocrystalline anisotropy and for Lu and Ir the largest values of in-plane magnetocrystalline anisotropy. The largest value of MAE for Pt interlayer is not surprising, considering the extremely high MAE values observed for the L_{10} FePt phase [20]. Furthermore, the previous calculations also showed an increase in the value of MAE for systems with W substitution [18,21].

Almost all TM elements, except Co and Ni, decrease the total spin magnetic moment relative to the Fe atom in the structures under our consideration, see Fig. 3(a), which is in good agreement with the Slater-Pauling curve [22]. We also see that almost all TMs, except Co, Ni, and Pt, contribute a lower orbital magnetic moment than Fe, see Fig. 3(c). Against this background, Pt stands out again, as it has the highest orbital moment among all the TMs considered. The orbital magnetic moment for bcc Fe calculated in this paper, which is $0.045 \mu_B$, is underestimated relative to the experimental value of $0.085 \mu_B$ [23]. Calculations of the spin and orbital magnetic moments on the atomic monolayer of the transition metal show explicit trends with increasing atomic numbers. Analogous trends have been found for point substitutions in bulk-iron, both theoretically [24,25] and experimentally [26].

Therefore, we conducted a detailed case study for system with Pt for which we obtained the maximum value of MAE. In Fig. 4a, we have shown the oscillation of charge and spin magnetic moment in Fe/Pt/Fe-sandwich system. For Pt we observe spin magnetic moment $0.42 \mu_B$ and for three Fe layers nearest to Pt the corresponding values are as follows: 2.76, 2.32, and $2.25 \mu_B$. However, the Fe layers farthest from the Pt layer exhibit bulk Fe-bcc magnetic properties.

We present the calculation of density of states to show what happens near the interface in the Fe/Pt/Fe-sandwich, see Fig. 5. In Fig. 5b we present the total DOS for the Fe/Pt/Fe system with the comparisons in Fig. 5a for Fe₂₂-bcc in the same model as discussed here (Fe/Fe/Fe-sandwich system). In this notation, the Fe₂₂ is a pristine 22-atom supercell containing only Fe atoms. The comparison of Fe₂₂ DOS with Fe/Pt/Fe DOS shows great similarity and few differences, resulting from about two additional electrons on the Pt 5d shell compared to the Fe 3d shell. The c–g panels show the contributions from the d orbitals of the two closest (Fe1, Fe2) and farthest (Fe10, Fe11) Fe layers in relation to the Pt layer. For the Pt 5d band, one spin channel is partially empty, and the other is completely filled. The DOS for Fe10 and Fe11, farthest from the Pt layer, resemble the spectra observed for Fe₂₂. The van Hove singularity on the Fermi level observed for Fe/Pt/Fe-sandwich system comes from the Pt 5d states. This narrow maximum at the Fermi level can have a significant impact on the electrochemical properties of the considered system. Unlike the band-types typical of valence band states, it can be interpreted as a characteristic of an atomic-like state of electrons.

4. Summary and conclusions

We have presented the first-principles results for the Fe/TM/Fe-sandwich system. Almost all TM layers, except Co and Ni layers, reduce the total spin magnetic moment in the considered models, which agrees well with the Slater-Pauling curve. We observe that W and Pt monolayers induce strong perpendicular magnetocrystalline anisotropy, while Lu and Ir most strongly prefer in-plane anisotropy. Our calculations indicate oscillation of spin magnetic moment and charge in the direction perpendicular to the plane of the monolayer. We have also observed the van Hove singularity in the formed Fe/TM interface for TM = Ag, Pd, Pt, Ir, and Au.

Article: Magnetic properties of 3d, 4d, and 5d transition-metal atomic monolayers in Fe/TM/Fe sandwiches: Systematic first-principles study

J. Snarski-Adamski et al.

Journal of Magnetism and Magnetic Materials 546 (2022) 168828

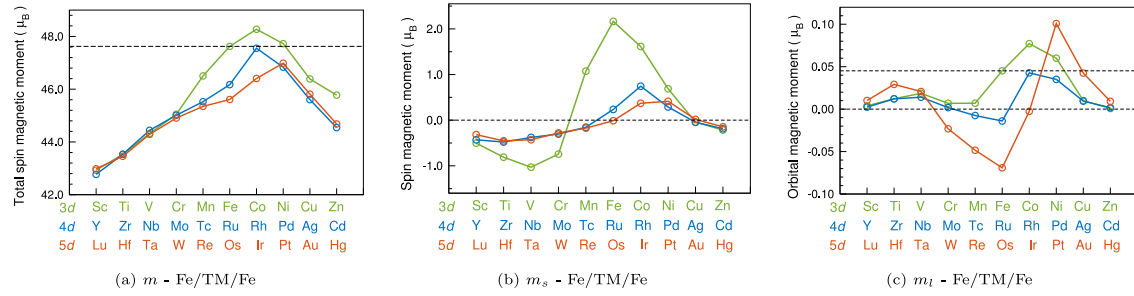


Fig. 3. (a) Total spin magnetic moment per formula unit, (b) spin magnetic moment as calculated for spin quantization axis along the distinguished axis [001], (c) orbital magnetic moment as calculated for spin quantization axis along the [001] for various 3d, 4d, and 5d TM elements in the Fe/TM/Fe-sandwiches. Calculations were performed with FPLO18, using the PBE functional and supercell method.

Table 1

Values of magnetocrystalline anisotropy energy [MAE (μeV/atom)], total spin magnetic moment [m (μ_B u.c.⁻¹)], spin magnetic moment [m_s (μ_B u.c.⁻¹)] on transition metal (TM), and orbital magnetic moment [m_l (μ_B u.c.⁻¹)] on TM for various 3d, 4d, and 5d TM elements in the Fe/TM/Fe-sandwiches. Calculations were performed with PBE FPLO18.

3d					4d					5d				
TM	MAE	m	m_s	m_l	TM	MAE	m	m_s	m_l	TM	MAE	m	m_s	m_l
Sc	-20.46	42.93	-0.50	0.0039	Y	-52.96	42.77	-0.43	0.0024	Lu	-69.73	42.98	-0.32	0.0102
Ti	-1.06	43.53	-0.81	0.0123	Zr	-32.93	43.54	-0.48	0.0121	Hf	-7.88	43.46	-0.45	0.0292
V	-8.47	44.32	-1.03	0.0186	Nb	-18.24	44.44	-0.38	0.0141	Ta	1.27	44.29	-0.43	0.0207
Cr	-2.25	45.05	-0.74	0.0068	Mo	6.38	45.01	-0.30	0.0018	W	63.41	44.91	-0.28	-0.0232
Mn	-3.69	46.50	1.07	0.0070	Tc	-10.62	45.53	-0.16	-0.0075	Re	3.65	45.35	-0.17	-0.0484
Fe	-0.63	47.62	2.16	0.0451	Ru	-6.52	46.17	0.23	-0.0140	Os	-18.48	45.61	-0.01	-0.0692
Co	-2.67	48.27	1.61	0.0771	Rh	-3.06	47.55	0.74	0.0427	Ir	-97.39	46.41	0.37	-0.0027
Ni	-2.76	47.73	0.69	0.0601	Pd	14.28	46.83	0.29	0.0351	Pt	124.80	46.99	0.41	0.1008
Cu	15.08	46.39	-0.04	0.0101	Ag	23.30	45.60	-0.05	0.0094	Au	25.82	45.81	0.02	0.0425
Zn	24.08	45.77	-0.22	0.0008	Cd	12.22	44.54	-0.19	0.0017	Hg	-13.64	44.68	-0.15	0.0092

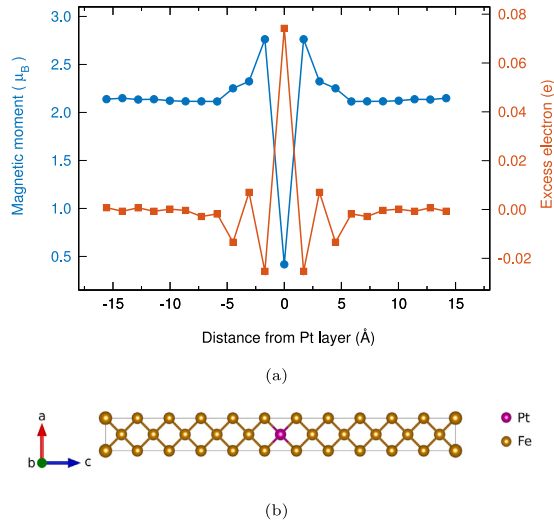


Fig. 4. (a) Calculation of spin magnetic moment and charge oscillations in Fe/Pt/Fe-sandwich system. (b) A model of the crystal structure of Fe/TM/Fe-sandwich. Calculations were performed with PBE FPLO18.

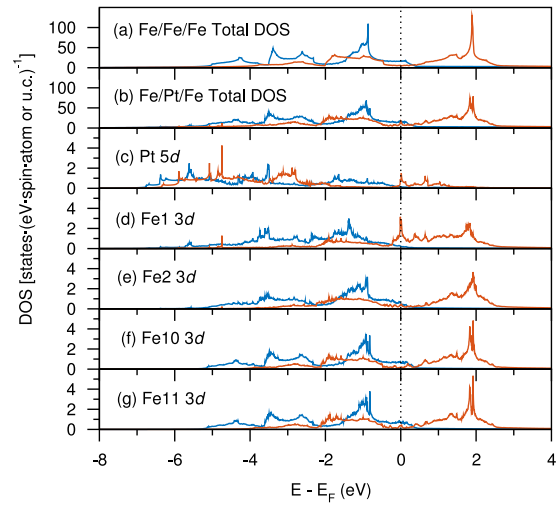


Fig. 5. Calculated densities of states (DOS) for the considered Fe/TM/Fe structures. (a) Fe₂₂ total DOS, (b) Fe/Pt/Fe total DOS, (c) Pt 5d DOS, (d, e) Fe1 and Fe2 3d DOS for the two Fe layers closest to the Pt layer, (f, g) Fe10 and Fe11 3d DOS for the two Fe layers furthest from the Pt layer. Calculations were performed with PBE FPLO18.

Article: Magnetic properties of 3d, 4d, and 5d transition-metal atomic monolayers in Fe/TM/Fe sandwiches: Systematic first-principles study

J. Snarski-Adamski et al.

Journal of Magnetism and Magnetic Materials 546 (2022) 168828

CRediT authorship contribution statement

Justyn Snarski-Adamski: Conceptualization, Methodology, Validation, Formal analysis, Investigation, Writing – original draft, Data curation, Writing – review & editing. **Justyna Rychły:** Conceptualization, Validation, Formal analysis, Investigation, Writing - Original Draft, Writing – review & editing. **Mirosław Werwiński:** Conceptualization, Methodology, Validation, Formal analysis, Investigation, Writing – original draft, Resources, Data curation, Writing – review & editing, Supervision, Project administration, Funding acquisition.

Declaration of competing interest

The authors declare that they have no known competing financial interests or personal relationships that could have appeared to influence the work reported in this paper.

Acknowledgments

We acknowledge the financial support of the National Science Center Poland under the decision DEC-2019/35/O/ST5/02980 (PRELUDIUM-BIS 1) and DEC-2018/30/E/ST3/00267 (SONATA-BIS 8). Part of the computations were performed on resources provided by the Poznan Supercomputing and Networking Center (PSNC). We thank Paweł Leśniak and Daniel Depcik for compiling the scientific software and administration of the computing cluster at the Institute of Molecular Physics, Polish Academy of Sciences.

Appendix

Table 1 provides the values shown in Figs. 2, 3a, 3b, and 3c.

References

- [1] T. Thersleff, S. Muto, M. Werwinski, J. Spiegelberg, Y. Kvashnin, B. Hjorvarsson, O. Eriksson, J. Ruz, K. Leifer, Towards sub-nanometer real-space observation of spin and orbital magnetism at the Fe/MgO interface, *Sci. Rep.* 7 (1) (2017) 44802, <http://dx.doi.org/10.1038/srep44802>.
- [2] R.S. Fishman, Spin-density waves in Fe/Cr trilayers and multilayers, *J. Phys. Condens. Matter* 13 (13) (2001) R235–R269, <http://dx.doi.org/10.1088/0953-8984/13/13/201>.
- [3] C. Turtur, G. Bayreuther, Magnetic moments in ultrathin Cr films on Fe(100), *Phys. Rev. Lett.* 72 (10) (1994) 1557–1560, <http://dx.doi.org/10.1103/PhysRevLett.72.1557>.
- [4] J.C. Slonczewski, Current-driven excitation of magnetic multilayers, *J. Magn. Magn. Mater.* 159 (1) (1996) L1–L7, [http://dx.doi.org/10.1016/0304-8853\(96\)00062-5](http://dx.doi.org/10.1016/0304-8853(96)00062-5).
- [5] C.L. Fu, A.J. Freeman, T. Oguchi, Prediction of strongly enhanced two-dimensional ferromagnetic moments on metallic overlayers, interfaces, and superlattices, *Phys. Rev. Lett.* 54 (25) (1985) 2700–2703, <http://dx.doi.org/10.1103/PhysRevLett.54.2700>.
- [6] C. Li, A.J. Freeman, Giant monolayer magnetization of Fe on MgO: A nearly ideal two-dimensional magnetic system, *Phys. Rev. B* 43 (1) (1991) 780–787, <http://dx.doi.org/10.1103/PhysRevB.43.780>.
- [7] S.T. Purcell, M.T. Johnson, N.W.E. McGee, R. Coehoorn, W. Hoving, Two-monolayer oscillations in the antiferromagnetic exchange coupling through Mn in Fe/Mn/Fe sandwich structures, *Phys. Rev. B* 45 (22) (1992) 13064–13067, <http://dx.doi.org/10.1103/PhysRevB.45.13064>.
- [8] S. Blügel, B. Dittler, R. Zeller, P.H. Dederichs, Magnetic properties of 3d transition metal monolayers on metal substrates, *Appl. Phys. A* 49 (6) (1989) 547–562, <http://dx.doi.org/10.1007/BF00616980>.
- [9] S. Blügel, Two-dimensional ferromagnetism of 3d, 4d, and 5d transition metal monolayers on noble metal (001) substrates, *Phys. Rev. Lett.* 68 (6) (1992) 851–854, <http://dx.doi.org/10.1103/PhysRevLett.68.851>.
- [10] D. Odkhui, S.H. Rhim, N. Park, S.C. Hong, Extremely large perpendicular magnetic anisotropy of an Fe(001) surface capped by 5d transition metal monolayers: A density functional study, *Phys. Rev. B* 88 (18) (2013) 184405, <http://dx.doi.org/10.1103/PhysRevB.88.184405>.
- [11] B. Sanyal, C. Antoniak, T. Burkert, B. Krumme, A. Warland, F. Stromberg, C. Praetorius, K. Fauth, H. Wende, O. Eriksson, Forcing ferromagnetic coupling between rare-earth-metal and 3d ferromagnetic films, *Phys. Rev. Lett.* 104 (15) (2010) 156402, <http://dx.doi.org/10.1103/PhysRevLett.104.156402>.
- [12] C. Autieri, P.A. Kumar, D. Walecki, S. Webers, M.A. Gubbins, H. Wende, B. Sanyal, Recipe for high moment materials with rare-earth and 3d transition metal composites, *Sci. Rep.* 6 (1) (2016) 29307, <http://dx.doi.org/10.1038/srep29307>.
- [13] C. Autieri, B. Sanyal, A systematic study of 4d and 5d transition metal mediated exchange coupling between Fe and Gd nanolaminates, *J. Phys. Condens. Matter* 29 (46) (2017) 465802, <http://dx.doi.org/10.1088/1361-648X/aa8f1e>.
- [14] K. Koepnick, H. Eschrig, Full-potential nonorthogonal local-orbital minimum-basis band-structure scheme, *Phys. Rev. B* 59 (3) (1999) 1743–1757, <http://dx.doi.org/10.1103/PhysRevB.59.1743>.
- [15] H. Eschrig, 2. The essentials of density functional theory and the full-potential local-orbital approach, in: W. Hergert, M. Däne, A. Ernst (Eds.), *Computational Materials Science: From Basic Principles to Material Properties*, in: Lecture Notes in Physics, Springer, Berlin, Heidelberg, 2004, pp. 7–21, http://dx.doi.org/10.1007/978-3-540-39915-5_2.
- [16] A. Edström, Magnetocrystalline anisotropy of Laves phase Fe₂Ta_{1-x}W_x from first principles: Effect of 3d-5d hybridization, *Phys. Rev. B* 96 (6) (2017) 064422, <http://dx.doi.org/10.1103/PhysRevB.96.064422>.
- [17] J.P. Perdew, K. Burke, M. Ernzerhof, Generalized gradient approximation made simple, *Phys. Rev. Lett.* 77 (18) (1996) 3865–3868.
- [18] M. Werwiński, A. Edström, J. Ruz, D. Hedlund, K. Gunnarsson, P. Svedlindh, J. Cedervall, M. Sahlberg, Magnetocrystalline anisotropy of Fe₂Pb₂ and its alloys with Co and 5d elements: A combined first-principles and experimental study, *Phys. Rev. B* 98 (21) (2018) 214431, <http://dx.doi.org/10.1103/PhysRevB.98.214431>.
- [19] K. Momma, F. Izumi, *VESTA*: A three-dimensional visualization system for electronic and structural analysis, *J. Appl. Crystallogr.* 41 (3) (2008) 653–658, <http://dx.doi.org/10.1107/S0021889808012016>.
- [20] R.A. Ristau, K. Barmak, L.H. Lewis, K.R. Coffey, J.K. Howard, On the relationship of high coercivity and L₁0 ordered phase in CoPt and FePt thin films, *J. Appl. Phys.* 86 (8) (1999) 4527–4533, <http://dx.doi.org/10.1063/1.371397>.
- [21] A. Edström, M. Werwiński, D. Iuşan, J. Ruz, O. Eriksson, K.P. Skokov, I.A. Radulov, S. Ener, M.D. Kuz'min, J. Hong, M. Fries, D.Y. Karpenkov, O. Gutfleisch, P. Toson, J. Fidler, Magnetic properties of (Fe_{1-x}Co_x)₂B alloys and the effect of doping by 5d elements, *Phys. Rev. B* 92 (17) (2015) 174413, <http://dx.doi.org/10.1103/PhysRevB.92.174413>.
- [22] A. Williams, V. Moruzzi, A. Malozemoff, K. Terakura, Generalized Slater-Pauling curve for transition-metal magnets, *IEEE Trans. Magn.* 19 (5) (1983) 1983–1988, <http://dx.doi.org/10.1109/TMAG.1983.1062706>.
- [23] C.T. Chen, Y.U. Idzerda, H.-J. Lin, N.V. Smith, G. Meigs, E. Chaban, G.H. Ho, E. Pellegrin, F. Sette, Experimental confirmation of the X-ray magnetic circular dichroism sum rules for iron and cobalt, *Phys. Rev. Lett.* 75 (1) (1995) 152–155, <http://dx.doi.org/10.1103/PhysRevLett.75.152>.
- [24] H. Akai, Nuclear spin-lattice relaxation of impurities in ferromagnetic iron, *Hyperfine Interact.* 43 (1) (1988) 253–270, <http://dx.doi.org/10.1007/BF02398306>.
- [25] P.H. Dederichs, R. Zeller, H. Akai, H. Ebert, Ab-initio calculations of the electronic structure of impurities and alloys of ferromagnetic transition metals, *J. Magn. Magn. Mater.* 100 (1) (1991) 241–260, [http://dx.doi.org/10.1016/0304-8853\(91\)90823-S](http://dx.doi.org/10.1016/0304-8853(91)90823-S).
- [26] R. Wienke, G. Schütz, H. Ebert, Determination of local magnetic moments of 5d impurities in Fe detected via spin-dependent absorption, *J. Appl. Phys.* 69 (8) (1991) 6147–6149, <http://dx.doi.org/10.1063/1.348786>.

Boundary-induced phase in epitaxial iron layers

Anna L. Ravensburg¹, Mirosław Werwiński², Justyna Rychły-Gruszecka², Justyn Snarski-Adamski², Anna Elsukova,³
Per O. Å. Persson³, Ján Rusz⁴, Rimantas Brucas⁴, Björgvin Hjörvarsson¹, Peter Svedlindh⁴,
Gunnar K. Pálsson¹ and Vassilios Kapaklis¹

¹Department of Physics and Astronomy, Uppsala University, Box 516, 75120 Uppsala, Sweden

²Institute of Molecular Physics, Polish Academy of Sciences, ul. M. Smoluchowskiego 17, 60-179 Poznań, Poland

³Thin Film Physics Division, Department of Physics, Chemistry and Biology (IFM), Linköping University, 58183 Linköping, Sweden

⁴Department of Materials Science and Engineering, Uppsala University, Box 35, 75103 Uppsala, Sweden



(Received 22 January 2024; revised 15 May 2024; accepted 21 June 2024; published 12 August 2024)

We report on the discovery of a boundary-induced body-centered tetragonal iron phase in thin films deposited on MgAl_2O_4 (001) substrates. We present evidence for this phase using detailed x-ray analysis and *ab initio* density functional theory calculations. A lower magnetic moment and a rotation of the easy magnetization direction are observed, as compared with body-centered cubic iron. Our findings expand the range of known crystal and magnetic phases of iron, providing valuable insights for the development of heterostructure devices using ultrathin iron layers.

DOI: 10.1103/PhysRevMaterials.8.L081401

The magnetic properties of iron are multifaceted. This is reflected in the results obtained from investigations on the electric control of magnetic domains [1], magnetic anisotropy [2–4], magnetic damping [5], as well as magnetic interface effects [6–8]. Not only are single layers of Fe of relevance, but also Fe in multilayers and superlattices such as Fe/Cr [9,10], Fe/V [11], Fe/Au [12], Fe/MgO [13–15], or Fe/MgAl₂O₄ [16–20] exhibits nontrivial properties. The epitaxial matching of the layers is of particular importance [21,22] since strain and crystal structure can have large effects on the magnetic properties [23–26]. For example, iron can be ferromagnetic, low-spin or high-spin, antiferromagnetic, or even nonmagnetic [23–25], all depending on its tetragonal distortion (c/a) and unit cell volume. Therefore, access to unstrained ultrathin Fe layers is of large importance to enable the separation of boundary and strain effects.

Recently, it was found that Fe (001) layers can be epitaxially grown on single-crystalline MgAl_2O_4 (001) substrates [5,27,28]. A 45° in-plane rotation of the Fe unit cell relative to the unit cell of the substrate, provides growth conditions with an epitaxial misfit of only −0.2% compared with bulk body-centered cubic (bcc) Fe (001) [16,28–30]. Thus, the tetragonal distortion is expected to be low, and the Fe film is structurally similar to bcc Fe. Consequently, the crystal quality of Fe (001) layers can be significantly improved, as compared with Fe layers grown on MgO (001) [5,28,31] or Al₂O₃ (11 $\bar{2}$ 0) [32]. This opens up new alternatives to investigate the effects of layer thickness on, e.g., the magnetic properties of Fe, with

only minor substrate-induced strain effects, which is explored in this letter.

The Fe films were deposited using direct current magnetron sputtering, with nominal thicknesses t_{Fe} in the range of 6–100 Å, at a substrate temperature of 619(2) K. All films were capped at ambient temperature with Pd, Pt, or Al₂O₃. The purpose of the capping is to protect the Fe layer from oxidation. Measuring identical Fe layers with different capping layers allowed us to explore the effect of the outer boundary on the investigated properties. Representative x-ray diffraction patterns using Cu $K_{\alpha 1}$ radiation around the specular Fe (002) Bragg peak of three samples with 25, 50, and 100 Å Fe layer thicknesses are displayed in Fig. 1. As seen in the figure, the peak intensity, position, and shape are different for these samples. The intensity is found to increase quadratically with increasing thickness, as expected for fully structurally coherent layers [33,34]. Furthermore, the positions of the Fe (002) Bragg peak are shifted toward smaller angles with decreasing thickness of the layers. The out-of-plane atomic distance d in Fe layers of 25, 50, and 100 Å thicknesses is elongated compared with equilibrium bcc Fe [35,36], with the average out-of-plane lattice parameters c_0 along [001] being 2.9088(8), 2.8856(1), and 2.8738(2) Å, respectively. Hence, the average out-of-plane lattice parameter is consistent with a tetragonal distortion, which appears to increase with decreasing film thickness [16,28–30]. The full width at half maximum (FWHM) of the Fe (002) rocking curves are all <0.04°, independent of layer thickness, consistent with near-perfect single crystalline growth of all these layers. An atomic registry of the interface between Fe and the substrate was confirmed with atomic-resolved high-angular annular dark-field scanning transmission electron microscopy imaging. Furthermore, no evidence for any oxidation or structural damage was found near the interface (see the Supplemental Material (SM) [37]).

The observation of Laue oscillations around the Fe (002) Bragg peak (see Fig. 1) for all three samples [28,38,39]

Published by the American Physical Society under the terms of the Creative Commons Attribution 4.0 International license. Further distribution of this work must maintain attribution to the author(s) and the published article's title, journal citation, and DOI. Funded by Bibsam.

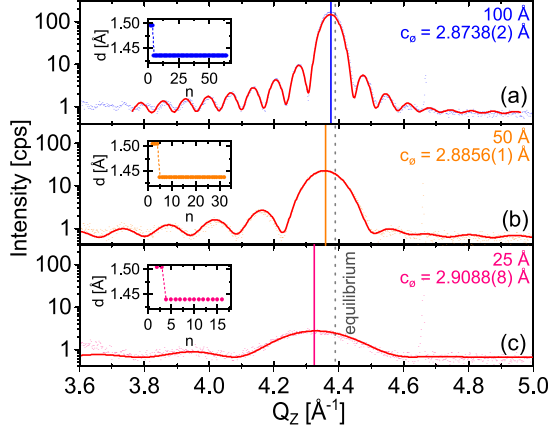


FIG. 1. X-ray diffraction patterns around the Fe (002) Bragg peak of (a) 100-Å-thick, (b) 50-Å-thick, and (c) 25-Å-thick Fe films grown on MgAl_2O_4 (001). Fits are shown as red lines. The corresponding out-of-plane lattice parameter c_θ is shown on the right. Insets: Evolution of the out-of-plane atomic distance d as a function of the number of atomic monolayers n .

provides additional information on the structural coherency. The asymmetry in the intensity of the Laue oscillations around the (002) peak is consistent with the presence of a change in out-of-plane interplanar atomic spacing in the Fe layers [39–42]. To obtain information on the shape of the profile of the interplanar spacing, we performed simulations of the Bragg peak and the Laue oscillations (see the SM [37]) using GENL [39]. The results of the fitting illustrated in Fig. 1 are consistent with the presence of two distinct coherently scattering regions in all samples: 3–4 monolayers (ML) closest to the substrate with large tetragonal out-of-plane distortion ($d = 1.50$ Å), while the rest of the films have a lattice parameter close to unstrained Fe.

In Fig. 2(a) we illustrate a summary of the results from the structural analysis, including asymmetric reflections, namely, the Fe (002) and (112) Bragg peaks (see the SM [37] for details and Refs. [45–48] therein). As seen in the figure, the average out-of-plane lattice parameter c_θ scales with the inverse thickness of the layers. The results were fitted using

$$c_\theta = c_1 \left(1 - \frac{t_\Delta}{t_{\text{Fe}}} \right) + c_2 \frac{t_\Delta}{t_{\text{Fe}}}, \quad (1)$$

where c_1 and c_2 denote the out-of-plane lattice parameters of the two regions, and t_Δ denotes the extension of the region closest to the substrate. The intercept of the y axis corresponds to infinitely thick Fe layers, with negligible contribution from the interface region. From the fitting, we get $c_1 = 2.862(5)$ Å, which is within the uncertainty identical to the unstrained lattice parameter of bcc Fe (2.866 Å) [35]. The slope of the fit in Fig. 2(a) is proportional to the thickness of the interface layers t_Δ and the difference in the lattice parameters of the two regions $(c_2 - c_1)t_\Delta = 0.58(5)$ Å². The corresponding values of $(c_2 - c_1)/t_\Delta$ from the fitting of the diffraction data (see Fig. 1) are 0.56, 0.79, and 0.56 Å² for the 100-, 50-, and 25-Å-thick layers, respectively. The extension of the interface

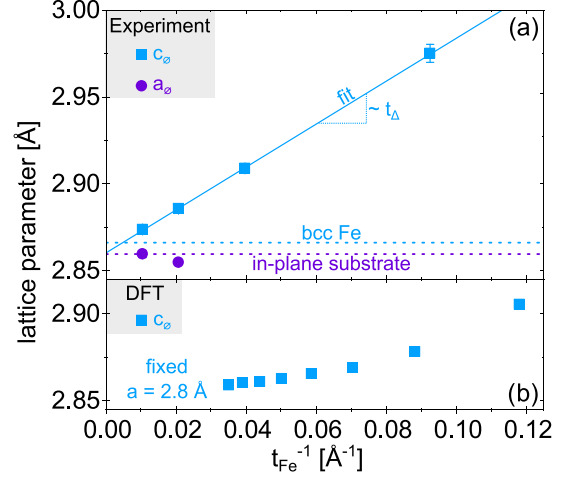


FIG. 2. (a) Experimental in-plane a_θ and out-of-plane c_θ lattice parameters for epitaxial Fe films with different layer thicknesses t_{Fe} . The Fe layers are capped with Pd. The choice of capping material did not affect the results, see the SM [37] (and Refs. [43,44] therein) for details. The dashed lines correspond to the equilibrium values of bcc Fe [35,36] and the MgAl_2O_4 substrate, while the solid line shows the fit of Eq. (1) to the data. (b) DFT calculated average out-of-plane lattice parameter c_θ for a fixed in-plane lattice parameters $a = 2.8$ Å plotted over inverse Fe layer thickness t_{Fe}^{-1} .

layer needs to be < 11 Å, as the data point from that sample is captured by the model in Fig. 2. Thus, the analysis of the diffraction data and the modeling of the shift of the (002) peak are consistent.

For the samples with 100- and 50-Å-thick Fe layers, the average in-plane lattice parameter a_θ was determined to be 2.860(2) and 2.856(3) Å, respectively, which closely matches the substrate (2.859 Å) [49]. Consequently, if the tetragonal distortion of the interface region originated from an elastic response to the biaxial strain, this would correspond to 0.91 in Poisson's ratio equivalent, i.e., the ratio of transverse to longitudinal extension strain, which is not physical for isotropic materials [50,51]. Hence, the tetragonal unit cell distortion is not strain induced, in contrast with other observed nonequilibrium Fe crystal structures like, e.g., body-centered tetragonal (bct) Fe on Ir (001) [52,53] or face-centered cubic (fcc) Fe on Ir (111) [52] or fcc Fe on Cu (001) [54], which are reported to be stabilized through epitaxy.

We used density functional theory (DFT) calculations to explore the contribution of finite-sized effects on the obtained results. Consequently, first, the calculations were performed on freestanding Fe layers. The total energy for a tetragonally distorted bct structure was found to be lower than that obtained for bcc when the thickness was < 9 ML (see the SM [37] and Refs. [55–58] therein). For biaxially clamped Fe layers with $c/a > 1$, corresponding to the same strain state as experimentally determined for Fe on MgAl_2O_4 (001), the calculated average out-of-plane lattice parameter c_θ is plotted as a function of inverse Fe layer thickness in Fig. 2(b). A profound tetragonal distortion is obtained for layers in the

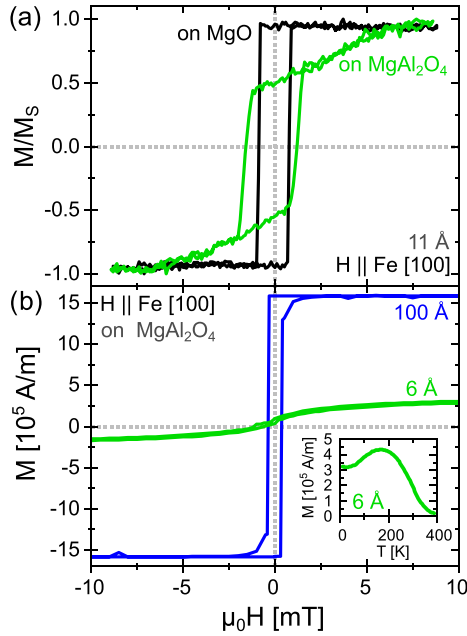


FIG. 3. Easy axis magnetic hysteresis of (a) thin films of 11 Å Fe grown on MgAl₂O₄ (001) and MgO (001), capped with 50 Å Pd and measured using a longitudinal magneto-optical Kerr effect (L-MOKE) setup and (b) 6 and 100 Å Fe grown on MgAl₂O₄ (001) capped with 50 Å Al₂O₃ measured in a superconducting quantum interference device (SQUID). The measurements were conducted at ambient temperature. Inset: Magnetization of the 6 Å Fe layer at a constant applied field of 5 mT as a function of temperature.

few-ML limit, while the obtained effect is thickness dependent. The effect decreases with increasing film thickness, giving rise to a change in slope, as seen in Fig. 2(b). Considering the size of the calculated effect and the observed changes with thickness, we conclude that the contribution from finite size to the experimentally found structural distortion is small, as compared with the interface effect described above.

Having established the presence of an interface layer with a deviating lattice parameter, we now turn our attention to its effects on the magnetic properties. Hysteresis curves that were measured with an applied field along the bulk Fe in-plane magnetic easy axis direction, i.e., Fe [100] of 11 Å Fe layers deposited simultaneously on MgAl₂O₄ (001) and MgO (001), are shown in Fig. 3(a). A square-shaped hysteresis curve is observed for the Fe layer on MgO (001), typical for an easy axis magnetization loop, in stark contrast with the Fe layer deposited on MgAl₂O₄ (001). Measurements with applied field along the bulk Fe in-plane magnetic hard axis direction, i.e., Fe [110], confirm a hard axis behavior for the sample on MgO and an increased remanence for the sample on MgAl₂O₄ (see the SM [37] for details and Ref. [59] therein). These observations are consistent with an exchange of easy and hard axes when Fe is grown on MgAl₂O₄ (001) and MgO (001) substrates, respectively. Measurements of the out-of-plane component of the magnetization do not indicate

an out-of-plane contribution to the magnetization, which can, however, not be excluded as an explanation for the moment reduction. The main effect is attributed to the electronic effects at the boundary in combination with some contribution from the finite size of the layers, which is in line with the sole observation of a reduced magnetic moment for the thinnest, i.e., 6-Å-thick Fe layer.

The contribution of the interface region to the overall magnetic properties can also be inferred by comparing samples with vastly different thicknesses. For instance, Fig. 3(b) displays hysteresis curves measured along the Fe [100] direction for 6 and 100 Å Fe layers deposited on MgAl₂O₄ (001). The absolute magnetization of the sample with 100 Å Fe layer thickness is $M_s = 1.588 \times 10^6$ A/m; $\mu_0 M_s = 1.99$ T, which is slightly smaller than for bulk Fe, where $\mu_0 M_s = 2.15$ T [60]. The difference is attributed to the finite layer thickness. For the thinner 6 Å Fe layer, we observe a reduction in the saturation magnetization, accompanied also by a distinct change in the shape of the hysteresis curve. The temperature-dependent magnetization of the 6 Å Fe layer was determined in an applied magnetic field of 5 mT along the Fe [100] direction. An initial increase with decreasing temperature is observed, followed by a decrease with decreasing temperature <150 K. These observations are consistent with an increase in magnetic anisotropy, exceeding the torque provided by the external field at ~150 K, in line with the conclusions above. The tetragonal distortion at the interface is not the only factor affecting the magnetic properties. For example, Fe forms Fe-O bonds at the MgAl₂O₄ (001) interface [16,31], which can contribute to lower magnetization, a change in the magnetic anisotropy, as well as lower Curie temperature. For the 6 Å Fe layer, the contribution of finite-sized effects on the ordering temperature is nonnegligible and can be determined by empirical models, as seen in Zhang and Willis [61] and Xin *et al.* [62].

In summary, we have identified a boundary-induced state in Fe at the interface with a MgAl₂O₄ (001) substrate. The interface state in Fe is argued to result from an electronic proximity effect with the substrate. The easy axis of the observed bct phase is rotated by $\pi/4$ as compared with bulk Fe, which gives rise to changes in the obtained anisotropy with thickness. These findings add to the understanding and optimal design of ML-thick Fe layers in heterostructures such as Fe/MgO or Fe/MgAl₂O₄, which hold a potential for magnetic tunnel junctions and future three-dimensional memory storage devices.

The data that support the findings of this paper are available from the authors upon reasonable request.

V.K. and P.S. acknowledge financial support from the Swedish Research Council (Projects No. 2019-03581 and No. 2021-04658). G.K.P. acknowledges funding from the Swedish Energy Agency (Project No. 2020-005212). M.W., J.R.G., and J.S.A. acknowledge financial support from the National Science Center Poland under Decisions No. DEC-2018/30/E/ST3/00267 (SONATA-BIS 8) and No. DEC-2019/35/O/ST5/02980 (PRELUDIUM-BIS 1). The authors also acknowledge access to the Swedish National Infrastructure for Advanced Electron Microscopy, ARTEMI, supported

by the Swedish Research Council (VR) and the Foundation for Strategic Research (SSF), through Grants No. 2021-00171 and No. RIF21-0026. J.R. acknowledges financial support from the Swedish Research Council (Grant No. 2021-03848),

Olle Engkvist's Foundation (Grant No. 214-0331) and Knut and Alice Wallenberg Foundation (Grant No. 2022.0079). The authors would like to thank Christina Vantaraki for AFM measurements.

- [1] P. Gospodarič, E. Młyńczak, I. Soldatov, A. Kákay, D. E. Bürgler, L. Plucinski, R. Schäfer, J. Fassbender, and C. M. Schneider, *Phys. Rev. Res.* **3**, 023089 (2021).
- [2] H. J. Elmers and U. Gradmann, *Appl. Phys. A* **51**, 255 (1990).
- [3] R. Allenspach and A. Bischof, *Phys. Rev. Lett.* **69**, 3385 (1992).
- [4] N. Metoki, M. Hofelich, T. Zeidler, T. Mühge, C. Morawe, and H. Zabel, *J. Magn. Magn. Mater.* **121**, 137 (1993).
- [5] B. Khodadadi, A. Rai, A. Sapkota, A. Srivastava, B. Nepal, Y. Lim, D. A. Smith, C. Mewes, S. Budhathoki, A. J. Hauser, M. Gao, J.-F. Li, D. D. Viehland, Z. Jiang, J. J. Heremans, P. V. Balachandran, T. Mewes, and S. Emori, *Phys. Rev. Lett.* **124**, 157201 (2020).
- [6] T. Urano and T. Kanaji, *J. Phys. Soc. Jpn.* **57**, 3403 (1988).
- [7] J. Balogh, I. Dézsi, C. Fetzter, J. Korecki, A. Kozioł-Rachwał, E. Młyńczak, and A. Nakanishi, *Phys. Rev. B* **87**, 174415 (2013).
- [8] F. Ibrahim, A. Hallal, A. Kalitsov, D. Stewart, B. Dieny, and M. Chshiev, *Phys. Rev. Appl.* **17**, 054041 (2022).
- [9] P. Etienne, G. Creuzet, A. Friederich, F. Nguyen-Van-Dau, A. Fert, and J. Massies, *Appl. Phys. Lett.* **53**, 162 (1988).
- [10] S. S. P. Parkin, N. More, and K. P. Roche, *Phys. Rev. Lett.* **64**, 2304 (1990).
- [11] B. Hjörvarsson, J. A. Dura, P. Isberg, T. Watanabe, T. J. Udovic, G. Andersson, and C. F. Majkrzak, *Phys. Rev. Lett.* **79**, 901 (1997).
- [12] A. Fuß, S. Demokritov, P. Grünberg, and W. Zinn, *J. Magn. Magn. Mater.* **103**, L221 (1992).
- [13] J. Faure-Vincent, C. Tiusan, C. Bellouard, E. Popova, M. Hehn, F. Montaigne, and A. Schuhl, *Phys. Rev. Lett.* **89**, 107206 (2002).
- [14] R. Moubah, F. Magnus, T. Warnatz, G. K. Palsson, V. Kapaklis, V. Ukleev, A. Devishvili, J. Palisaitis, P. O. A. Persson, and B. Hjörvarsson, *Phys. Rev. Appl.* **5**, 044011 (2016).
- [15] F. Magnus, T. Warnatz, G. K. Palsson, A. Devishvili, V. Ukleev, J. Palisaitis, P. O. A. Persson, and B. Hjörvarsson, *Phys. Rev. B* **97**, 174424 (2018).
- [16] H. Sukegawa, H. Xiu, T. Ohkubo, T. Furubayashi, T. Niizeki, W. Wang, S. Kasai, S. Mitani, K. Inomata, and K. Hono, *Appl. Phys. Lett.* **96**, 212505 (2010).
- [17] Y. Miura, S. Muramoto, K. Abe, and M. Shirai, *Phys. Rev. B* **86**, 024426 (2012).
- [18] M. Belmoubarik, H. Sukegawa, T. Ohkubo, S. Mitani, and K. Hono, *Appl. Phys. Lett.* **108**, 132404 (2016).
- [19] K. Masuda and Y. Miura, *Phys. Rev. B* **96**, 054428 (2017).
- [20] Q. Xiang, R. Mandal, H. Sukegawa, Y. K. Takahashi, and S. Mitani, *Appl. Phys. Express* **11**, 063008 (2018).
- [21] V. Martin, W. Meyer, C. Giovanardi, L. Hammer, K. Heinz, Z. Tian, D. Sander, and J. Kirschner, *Phys. Rev. B* **76**, 205418 (2007).
- [22] D. Sander, *Rep. Prog. Phys.* **62**, 809 (1999).
- [23] V. L. Moruzzi, P. M. Marcus, and J. Kübler, *Phys. Rev. B* **39**, 6957 (1989).
- [24] S. Andrieu, F. L. Razafindramisa, E. Snoeck, H. Renevier, A. Barbara, J. M. Tonnerre, M. Brunel, and M. Picuch, *Phys. Rev. B* **52**, 9938 (1995).
- [25] M. Friák, M. Šob, and V. Vitek, *Phys. Rev. B* **63**, 052405 (2001).
- [26] T. Burkert, L. Nordström, O. Eriksson, and O. Heinonen, *Phys. Rev. Lett.* **93**, 027203 (2004).
- [27] A. J. Lee, J. T. Brangham, Y. Cheng, S. P. White, W. T. Ruane, B. D. Esser, D. W. McComb, P. C. Hammel, and F. Yang, *Nat. Commun.* **8**, 234 (2017).
- [28] A. L. Ravensburg, G. K. Pálsson, M. Pohlitz, B. Hjörvarsson, and V. Kapaklis, *Thin Solid Films* **761**, 139494 (2022).
- [29] S. M. Hosseini, *Phys. Status Solidi (b)* **245**, 2800 (2008).
- [30] I. Ganesh, *Int. Mater. Rev.* **58**, 63 (2013).
- [31] H. L. Meyerheim, R. Popescu, J. Kirschner, N. Jedrecy, M. Sauvage-Simkin, B. Heinrich, and R. Pinchaux, *Phys. Rev. Lett.* **87**, 076102 (2001).
- [32] T. Mühge, A. Stierle, N. Metoki, H. Zabel, and U. Pietsch, *Appl. Phys. A* **59**, 659 (1994).
- [33] P. F. Fewster, *Rep. Prog. Phys.* **59**, 1339 (1996).
- [34] M. Birkholz, in *Thin Film Analysis by X-Ray Scattering* (John Wiley and Sons, Ltd, Weinheim, 2005), Chap. 1, pp. 1–40.
- [35] J. L. Vassent, M. Dynna, A. Marty, B. Gilles, and G. Patrat, *J. Appl. Phys.* **80**, 5727 (1996).
- [36] G. Chiarotti, *Interaction of Charged Particles and Atoms with Surfaces* (Springer, Berlin, 1995).
- [37] See Supplemental Material at <http://link.aps.org/supplemental/10.1103/PhysRevMaterials.8.L081401> for the detailed description of the methods for data analysis and supporting experimental findings.
- [38] A. J. Ying, C. E. Murray, and I. C. Noyan, *J. Appl. Cryst.* **42**, 401 (2009).
- [39] A. L. Ravensburg, J. Bylin, G. K. Pálsson, and V. Kapaklis, *arXiv:2310.13539*.
- [40] I. Vartanyants, C. Ern, W. Donner, H. Dosch, and W. Caliebe, *Appl. Phys. Lett.* **77**, 3929 (2000).
- [41] I. Robinson and I. Vartanyants, *Appl. Surf. Sci.* **182**, 186 (2001).
- [42] A. M. Miller, M. Lemon, M. A. Choffel, S. R. Rich, F. Harvel, and D. C. Johnson, *Z. Naturforsch. B* **77**, 313 (2022).
- [43] C. T. Campbell, *Surf. Sci. Rep.* **27**, 1 (1997).
- [44] T. P. A. Hase, M. S. Brewer, U. B. Arnalds, M. Ahlberg, V. Kapaklis, M. Björck, L. Bouchenoire, P. Thompson, D. Haskel, Y. Choi, J. Lang, C. Sánchez-Hanke, and B. Hjörvarsson, *Phys. Rev. B* **90**, 104403 (2014).
- [45] M. Björck and G. Andersson, *J. Appl. Cryst.* **40**, 1174 (2007).
- [46] A. Glavic and M. Björck, *J. Appl. Cryst.* **55**, 1063 (2022).
- [47] J. Birch, J. Sundgren, and P. F. Fewster, *J. Appl. Phys.* **78**, 6562 (1995).
- [48] J. Schroeder, A. Ingason, J. Rosén, and J. Birch, *J. Cryst. Growth* **420**, 22 (2015).
- [49] P. Villars, K. Cenzual, J. Daams, R. Gladyshevskii, O. Shcherban, V. Dubenskyy, N. Melnichenko-Koblyuk, O. Pavlyuk, S. Stoiko, and L. Sysa, *Structure Types. Part 1: Space Groups (230)Ia-3d-(219)-F43-c MgAl₂O₄: Datasheet from Landolt-Börnstein—Group III Condensed Matter Volume 43A1* (Springer, Berlin, 2004).
- [50] K. W. Wojciechowski, *J. Phys. Soc. Jpn.* **72**, 1819 (2003).

- [51] C. W. Huang, W. Ren, V. C. Nguyen, Z. Chen, J. Wang, T. Sriharan, and L. Chen, *Adv. Mater.* **24**, 4170 (2012).
- [52] M. Piecuch, S. Andrieu, J. F. Bobo, and P. Bauer, *Magnetism and Structure in Systems of Reduced Dimension*, edited by R. F. C. Farrow, B. Dieny, M. Donath, A. Fert, and B. D. Hermsmeier (Springer, New York, 1993).
- [53] S. Andrieu, M. Piecuch, H. Fischer, J. Bobo, F. Bertran, P. Bauer, and M. Hennion, *J. Magn. Magn. Mater.* **121**, 30 (1993).
- [54] S. Müller, P. Bayer, C. Reischl, K. Heinz, B. Feldmann, H. Zillgen, and M. Wuttig, *Phys. Rev. Lett.* **74**, 765 (1995).
- [55] M. Methfessel and A. T. Paxton, *Phys. Rev. B* **40**, 3616 (1989).
- [56] P. E. Blöchl, O. Jepsen, and O. K. Andersen, *Phys. Rev. B* **49**, 16223 (1994).
- [57] K. Koepernik and H. Eschrig, *Phys. Rev. B* **59**, 1743 (1999).
- [58] J. P. Perdew, K. Burke, and M. Ernzerhof, *Phys. Rev. Lett.* **77**, 3865 (1996).
- [59] Y. Park, E. E. Fullerton, and S. D. Bader, *Appl. Phys. Lett.* **66**, 2140 (1995).
- [60] J. Solano, O. Gladii, P. Kuntz, Y. Henry, D. Halley, and M. Bailleul, *Phys. Rev. Mater.* **6**, 124409 (2022).
- [61] R. Zhang and R. F. Willis, *Phys. Rev. Lett.* **86**, 2665 (2001).
- [62] X. Xin, G. K. Pálsson, M. Wolff, and B. Hjörvarsson, *Phys. Rev. Lett.* **113**, 046103 (2014).

Supplementary: Boundary-induced phase in epitaxial iron layers

Anna L. Ravensburg,¹ Mirosław Werwiński,² Justyna Rychły-Gruszecka,² Justyn
Snarski-Adamski,² Anna Elsukova,³ Per O. Å. Persson,³ Ján Ruzs,¹ Rimantas Brucas,⁴
Björgvin Hjörvarsson,¹ Peter Svedlindh,⁴ Gunnar K. Pálsson,¹ and Vassilios Kapaklis¹

¹Department of Physics and Astronomy,

Uppsala University, Box 516, 75120 Uppsala, Sweden

²Institute of Molecular Physics, Polish Academy of Sciences,

ul. M. Smoluchowskiego 17, 60-179 Poznań, Poland

³Thin Film Physics Division, Department of Physics,

Chemistry and Biology (IFM), Linköping University, 58183 Linköping, Sweden

⁴Department of Materials Science and Engineering,

Uppsala University, Box 35, 75103 Uppsala, Sweden

I. METHODS

A. Growth details

Fe thin films were deposited using direct current (dc) magnetron sputtering on single crystalline MgAl_2O_4 (001) substrates of size $10 \times 10 \text{ mm}^2$ at floating potential. The substrates were annealed at 1273(2) K in vacuum for 600 s prior to growth. The base pressure of the growth chamber was below $5 \times 10^{-7} \text{ Pa}$. In order to prevent surface oxidation of the films due chemical affinity of Fe for oxygen [S1], the samples were capped at ambient temperature ($< 313(2) \text{ K}$) with Pd and selected samples with Pt or Al_2O_3 instead. The capping layer thickness was varied between 10 Å and 50 Å. The depositions were carried out at a power of 50 W in an Ar atmosphere (gas purity $\geq 99.999 \%$, and a secondary getter based purification) from elemental Fe (0.67 Pa Ar, dc), Pd (1.07 Pa Ar, dc), and Pt (1.07 Pa Ar, dc) targets and an Al_2O_3 (0.67 Pa Ar, rf) compound target. The targets were sputter cleaned against closed shutters for 60 s prior to each deposition. The target-to-substrate distance in the deposition chamber was around 0.2 m. The deposition rates (Fe: 0.1 Å/s, Pd: 0.6 Å/s, Pt: 0.8 Å/s, Al_2O_3 : 0.01 Å/s) were calibrated prior to the growth. Details on the optimization of the deposition temperature can be found elsewhere [S2]. In order to ensure thickness uniformity, the substrate holder was rotated at 30 rpm during deposition. Atomic force microscopy (AFM) measurements of a sample with 11(1) Å Fe layer thickness confirmed the presence of a continuous Fe layer.

B. X-ray scattering details

X-ray reflectometry (XRR) and diffraction (XRD) were carried out in a Bede D1 diffractometer equipped with a Cu x-ray source. The setup includes a Göbel mirror and a 2-bounce-crystal on the incidence side. Furthermore, a circular mask with a diameter of 5 mm, an incidence and a detector slit, 0.5 mm each, were used. The scattered x-rays were detected with a Bede EDRC x-ray detector. The instrument angles were aligned to the sample surface for XRR and to the Fe crystal planes for XRD measurements. The measured XRR data was fitted using GENX [S3, S4] enabling the determination of layer thickness and roughness and of the scattering length density (SLD) profile. However, twinning in the substrates, and therefore also in the epitaxially growing Fe layers, may lead to an overestimation of the

layer roughnesses. In diffraction, the samples were measured with a combination of coupled 2θ - θ and rocking curve scans. Incident and reflected angles were converted to momentum transfer Q . Peak positions in Q_z (out-of-plane component) and the width of rocking curves were determined by fitting with a Gaussian and a Lorentzian profile, respectively. All error bars for fits of scattering data are statistical and do not include systematic errors arising from alignment or absorption. X-ray diffraction patterns including Laue oscillations were fitted with GENL [S5]. The fitted parameters relating to the Fe layer were: the average number of coherently scattering planes contributing to the Laue oscillations N_L and the average out-of-plane atomic distance d_{002} . Moreover, a strain profile was fitted within the model to account for strain relaxation [S5]. A contribution of other factors to the asymmetry, e.g., the presence of finite atomic terraces or crystal grains [S6] was omitted. Hence, as the employed model takes into account only strain as a source for the asymmetry in the Laue oscillations, the change in out-of-plane atomic distance over layer thickness might be overestimated.

Reciprocal space mapping (RSM) around the (002) and (112) Fe Bragg reflections was carried out in a Bruker D8 Discover equipped with a Cu x-ray source and a 1D Bruker LynxEye detector. The setup included a Göbel mirror, a 0.2 mm slit, and a Soller slit on the incidence side as well as a 4.6 mm slit, a beam collimator, and a Soller slit on the detector side. The maps were fitted with Gaussian and Lorentzian intensity profiles in Q_z (out-of-plane component) and Q_x (in-plane component) directions, respectively. Out-of-plane and in-plane lattice parameters were extracted according to [S7]. In addition, the accuracy of the determined parameters was confirmed by repeating the measurements with a sample of 100 Å Fe layer thickness on the above mentioned $K_{\alpha 1}$ monochromatic Bede D1 x-ray machine.

The Poisson's ratio equivalent ν was calculated based on the relation between in-plane and out-of-plane distortion of a unit cell due to uniaxial stress [S8]:

$$\frac{2\nu}{1+\nu} = \frac{1 - \frac{a_{eq}}{c}}{\frac{c-a}{a}}, \quad (S1)$$

where a_{eq} , a , and c denote the equilibrium, the strained in-plane, and the strained out-of-plane lattice parameters, respectively.

C. Details on measurements of magnetisation

Magnetisation measurements were performed at ambient temperature using a longitudinal (L-MOKE) and polar (P-MOKE) magneto-optical-Kerr-effect setup with *s*-polarized light. The magnetic response was measured parallel and perpendicular to an in-plane applied magnetic field for L- and P-MOKE, respectively. The data was averaged over 10 full loop recordings. For L-MOKE, the samples were probed along the Fe [100] and [110] directions, hence, along the expected magnetic easy and hard axis, respectively. Selected samples were additionally probed at azimuthal angles between 350 and 190 degrees for the determination of their normalized remanent magnetisation. Displayed error bars correspond to statistical errors only.

The magnetic moment of selected samples was probed in a superconducting quantum interference device (SQUID) at temperatures between 10 and 400 K using a Quantum Design Magnetic Property Measurement System. The magnetic field in these measurements was applied in-plane along the Fe [100] direction.

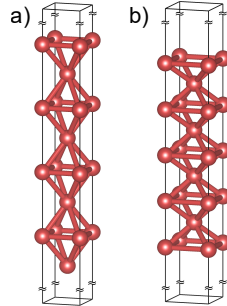
D. Details on transmission electron microscopy

Lattice- and atomic-resolved high-angular annular dark field scanning transmission electron microscopy (HAADF-STEM) imaging were carried out at ambient temperature with double-Cs corrected FEI Titan3 60–300, operated at 300 kV. The samples for TEM analysis were prepared by ion milling in a Gatan precision ion miller after fine mechanical polishing.

E. Details on computations

Density functional theory (DFT) calculations were performed using the full-potential local-orbital scheme (FPLO18.00-52) [S9, S10], employing the generalized gradient approximation (GGA) in the Perdew-Burke-Ernzerhof parametrization [S11]. The calculations were performed on *bcc* Fe model systems with a (001) surface and thicknesses ranging from one to twenty monolayers. We prepared the *bcc* Fe (001) films by duplicating the *bcc* Fe unit cell in one direction an appropriate number of times and then adding a vacuum with a minimum thickness of 13.7 Å, see Supplementary Fig. S1. Preserving the geometry of the square lattice base, we optimized (free-standing Fe) or fixed (clamped Fe) the lattice parameter a

of the base, and using forces, we optimized the distances in the z direction between atomic monolayers. We minimized the forces using a spin-polarized scalar-relativistic approach with a $20 \times 20 \times 1$ k-mesh and a convergence criterion of 10^{-3} eV \AA^{-1} . During force minimization, we used the first-order Methfessel-Paxton method [S12] to integrate the Brillouin zone, with a smearing parameter of 0.136 eV (0.005 hartree) and the convergence criterion for charge density was set to 10^{-6} . After geometry optimization, all scalar-relativistic results were recalculated with the k-mesh increased to $50 \times 50 \times 4$, which leads to convergent magneto-crystalline anisotropy energy (MAE) results. We defined MAE as the difference between the single-iteration fully-relativistic total energies calculated for the [100] and [001] quantization axes. The single fully-relativistic iterations were calculated using the tetrahedron method [S13] for Brillouin zone integration.

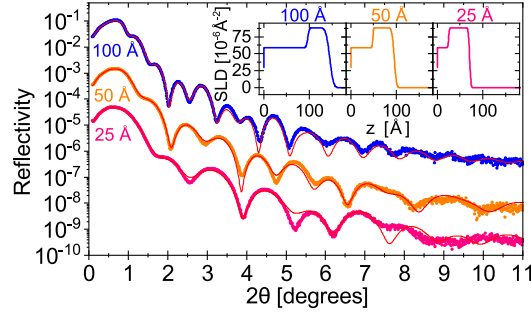


Supplementary FIG. **S1**. Ground state optimized unit cells of the selected considered Fe thin films of a) 8 and b) 9 MLs with body centered tetragonal *bct* and body centered cubic *bcc* phases, respectively, with a (001) surface. The structures are presented on a common scale allowing direct comparison of proportions. In the computational model, the unit cells shown are repeated infinitely in each direction, resulting in the generation of an idealized model of a thin films infinite in the plane.

II. RESULTS

A. Layering

X-ray reflectivity curves for Fe layers grown on MgAl_2O_4 (001) with a nominal thickness of 25, 50, and 100 Å are displayed in Supplementary Fig. S2. The scattering length density profiles corresponding to the displayed reflectivity fits are shown as insets in the respective color. The profiles agree well with the intended layering. The Fe layer thickness of the three thin films displayed in Supplementary Fig. S2 are determined to be 25(1), 48(1), and 96(1) Å. As they lie within 4% of the intended layer thickness, we refer to the nominal layer thickness throughout the text. The Fe layer roughness of the 25, 50, and 100 Å thick Fe layers are 1(1), 1(1), and 3(1) Å, respectively.

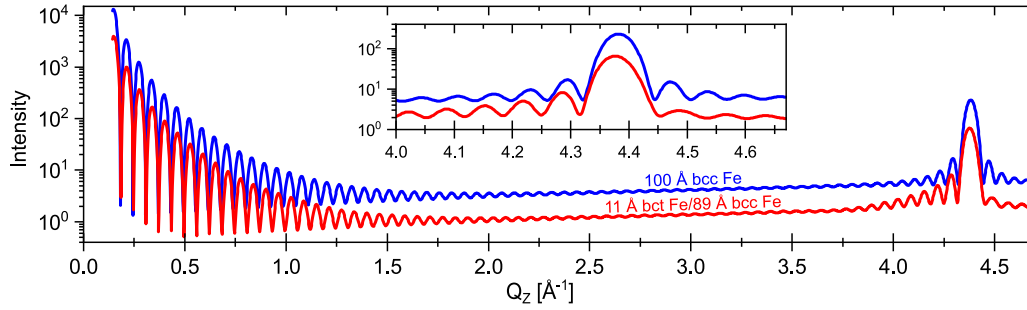


Supplementary FIG. S2. X-ray reflectivity of Fe films of varying thicknesses. Fits are shown as red lines. The curves have been vertically shifted for clarity. The respective scattering length density profiles are shown as insets.

B. Simulations and fittings of Laue oscillations

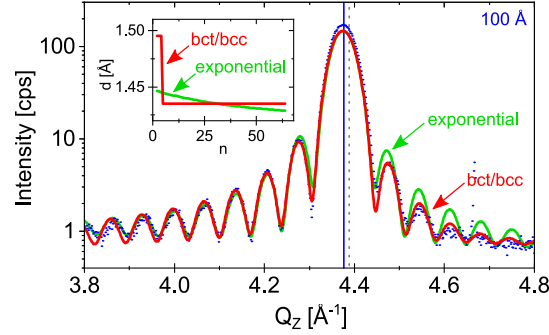
XRD patterns of Fe (001) with different out-of-plane atomic spacing profiles including Laue oscillations have been simulated using GENL [S5]. The results for two 100 Å Fe films are displayed in Supplementary Fig. S3, the first consisting of 11 Å *bct* Fe with out-of-plane $d = 1.5$ Å and 89 Å equilibrium *bcc* Fe $d = 1.433$ Å and the second film consisting of 100 Å equilibrium *bcc* Fe. From the simulations it is evident that the periodicity of the Laue oscilla-

tions is affected by these structural differences, because the spacing between the oscillations around the Fe (002) Bragg peak corresponds to the thickness of the *bcc* Fe layer. Hence, the spacing between two maxima is larger corresponding to smaller real space distances for the *bct/bcc* Fe sample. Furthermore, the oscillations become asymmetric around the Bragg peak, decaying faster on the high angle side, what has also been observed in experimentally measured x-ray diffraction patterns for Fe thin films deposited on MgAl_2O_4 (001), as displayed for a 100 Å Fe layer in Supplementary Fig. S4.



Supplementary FIG. S3. X-ray diffraction pattern simulations using GENL [S5] for 100 Å Fe layers consisting of, first, 11 Å *bct* Fe with $d = 1.5$ Å and 89 Å equilibrium *bcc* Fe (red) and second, 100 Å equilibrium *bcc* Fe (blue). A zoom onto the region around the Fe (002) Bragg peak is displayed in the inset.

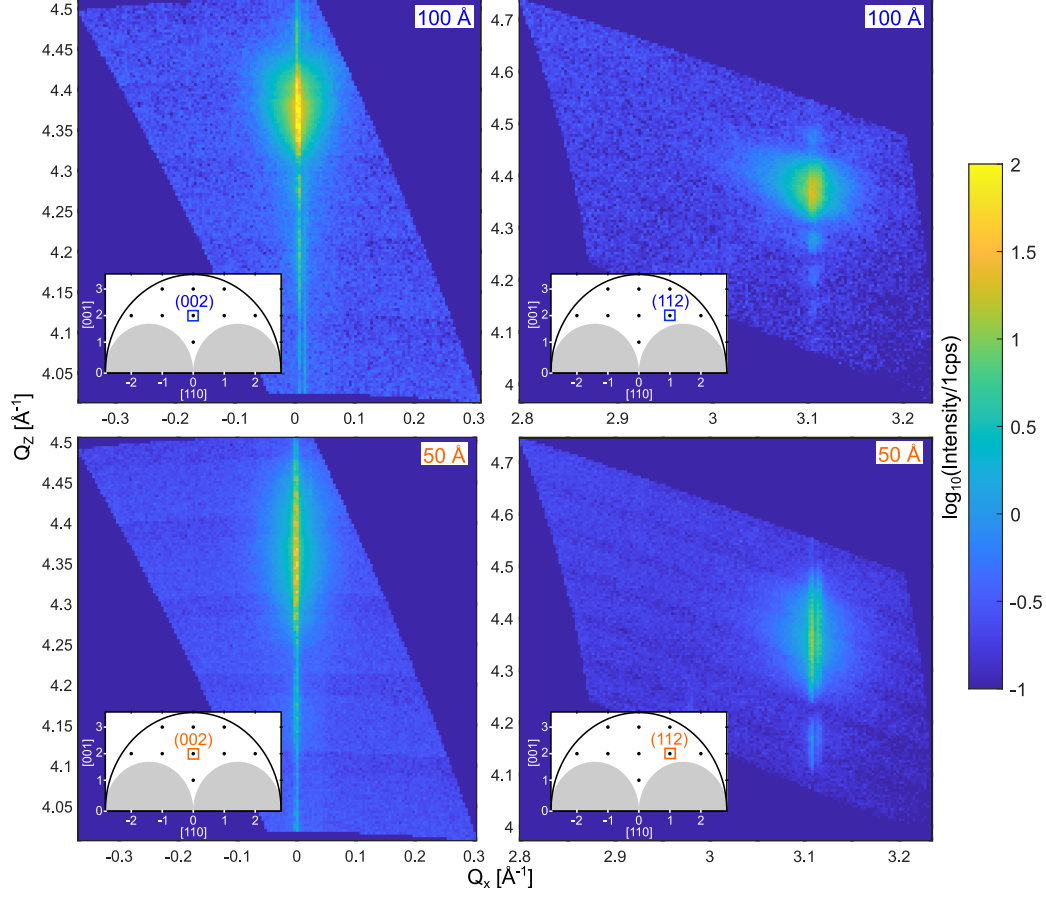
The diffraction data in Supplementary Fig. S4 was fitted using GENL [S5] and employing an exponentially decaying strain profile as well as the profile described above, having a *bct* Fe/*bcc* Fe bilayer out-of-plane interplanar spacing. It is evident that the *bct* Fe/*bcc* Fe bilayer profile captures the faster decay of the oscillations on the high angle side in more detail. As this is valid for all samples within this study, the fit employing the bilayer profile was used for the analysis. Based on the *bct* Fe/*bcc* Fe bilayer fits (displayed in the main text), the thickness of the *bct* Fe layer is about 3, 4, and 3 ML for the samples with 100, 50, and 25 Å Fe layer thickness, having an out-of-plane interplanar spacing of 1.495, 1.504, 1.504 Å, respectively. 94, 93, and 89 % of the 100, 50, and 25 Å samples contribute to coherent scattering, respectively.



Supplementary FIG. S4. X-ray diffraction pattern of a 100 Å Fe layer on MgAl_2O_4 (001). Fits using GENL [S5] are displayed as green and red lines for an exponentially decaying strain profile and a *bct/bcc* grown Fe film, respectively. The respective strain profiles are shown in the inset. The vertical line marks the Bragg peak position. The dotted line indicates the peak position expected for equilibrium *bcc* Fe.

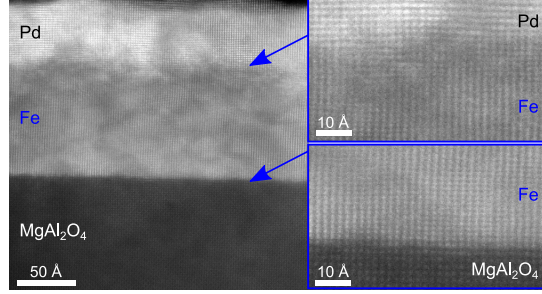
C. Reciprocal space maps

The reciprocal space maps (RSMs) for samples with 100 and 50 Å Fe layer thickness grown on MgAl_2O_4 (001) are displayed in the top and bottom panel of Supplementary Fig. S5, respectively. RSMs of samples with thicknesses below 50 Å Fe layer thickness could not be measured as the Bragg peak intensity was determined to lie below the detector background level of the used diffractometer. Sharp Bragg peaks are observable. The high intensity Fe (002) and (112) Bragg peaks are visible. Their position differs between the samples with 100 and 50 Å Fe layer thickness, in line with the observed peak shift displayed in Fig. 1 and discussed in the main text as an elongation of the out-of-plane atomic distance for thinner films. The corresponding average out-of-plane lattice parameters c_0 based on the RSMs deviate by less than 0.11% from the previously determined values based on specular scans. The corresponding in-plane lattice parameter a_0 were determined to be 2.860(2) and 2.856(3) Å for the samples with 100 and 50 Å thick Fe layers, respectively. The size of the in-plane lattice parameter for the 100 Å thick Fe layer based on fitting of the RSM was confirmed with TEM measurements in diffraction mode. Laue oscillations are observable for both samples for measurements for $Q_X = \text{constant}$, so along Q_Z . The spacing of the



Supplementary FIG. S5. Reciprocal space maps measured around the Fe (002) and (112) Bragg reflections on samples with 100 Å (top) and 50 Å (bottom) Fe layer thickness. Schematic illustrations of the position of the respective peak in reciprocal space are shown as insets.

oscillations is larger for the sample with 50 Å Fe layer thickness, in line with the results from the specular scans displayed in Fig. 1 in the main text. The oscillations are only visible along Q_z as they relate to the finite thickness in out-of-plane direction. While all peaks exhibit a shape which is rather broad along Q_z , it is observed to be significantly narrower along Q_x , in agreement with the observed small FWHM of the rocking curves for both samples. However, two parallel narrow lines are observable with $Q_x = \text{constant}$ corresponding to different crystal twins. Twinning in epitaxial thin films often results from



Supplementary FIG. **S6**. Left: Cross-section HAADF-STEM image of a $\text{MgAl}_2\text{O}_4/100 \text{ Å Fe}/50 \text{ Å Pd}$ film. Right: Magnifications on the Fe/Pd interface (top) and the substrate/Fe interface (bottom).

substrate twinning, which is common for this type of substrates [S14].

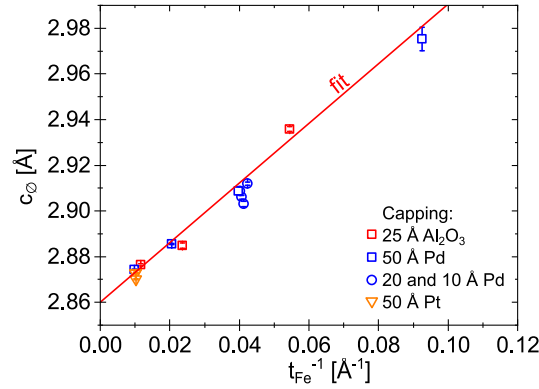
D. Real space imaging

Lattice- and atomic-resolved high-angular annular dark field scanning transmission electron microscopy (HAADF-STEM) results from the 100 Å Fe sample is displayed in Supplementary Fig. **S6**. Epitaxial registry of Fe (001) and MgAl_2O_4 (001) is clearly observed. The atoms at the interfaces grow in registry with low defect density in the distinct layers, whereby the substrate/Fe interface is sharper with improved layering compared to the Fe/Pd interface. Hence, x-ray diffraction and STEM measurements confirm almost defect-free growth of Fe (001) on MgAl_2O_4 (001), in line with the reported critical thickness of 785 Å of Fe (001) on MgAl_2O_4 (001) [S2].

E. Study of the influence of the capping layer

A possible physical origin of the observed tetragonal distortion of Fe on MgAl_2O_4 (001) might be a change of spin-orbit coupling in Fe layers at the thin film limit, due to the strong correlation of the structural and magnetic properties of Fe [S15–S17]. One possible cause for a change in spin-orbit coupling for thin Fe layers might be the large susceptibility of the 50 Å Pd capping layer [S18]. Hence, the influence of the capping layer on the Fe

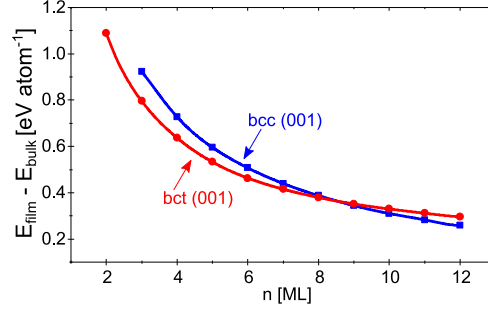
average out-of-plane lattice parameter c_ϕ was investigated and the results are displayed in Supplementary Fig. S7. First, 25 Å Fe thin films were grown on MgAl_2O_4 (001) with a variable Pd capping layer thickness of 10, 20, and 50 Å. Second, 100 Å Fe thin films were grown on MgAl_2O_4 (001) with a Pt capping layer thickness of 50 Å. Finally, 25, 50, and 100 Å thick Fe layers were grown on MgAl_2O_4 (001) with a 25 Å thick Al_2O_3 capping layer. The Fe out-of-plane lattice parameter c_ϕ of all samples shows the same linear increase with inverse Fe layer thickness independent of the choice of capping layer material or thickness. Therefore, an influence of the capping layer on the spin-orbit coupling of Fe layers at the thin film limit is excluded.



Supplementary FIG. S7. Average out-of-plane lattice parameter c_ϕ of Fe plotted over inverse Fe layer thickness for samples with different capping layers. A fit is shown in red.

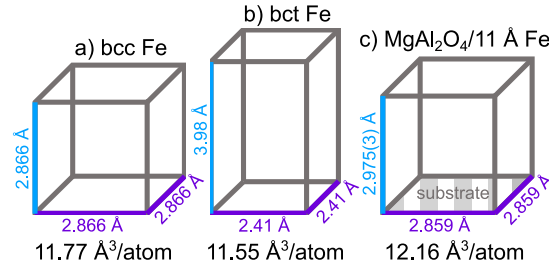
F. Results of DFT calculations and schematic illustration of Fe unit cells

Density functional theory (DFT) calculations at 0 K have indicated that below an Fe layer thickness of 9 ML a *bct* crystal structure with an elongated out-of-plane interplanar spacing is energetically more favorable compared to the equilibrium Fe *bcc* crystal structure, as can be seen in Supplementary Fig. S8. The calculations were performed for a [001] *bct* growth direction of free-standing layers, i.e., in vacuum. If the Fe lattice parameters a and c are not both relaxed but a is fixed, the calculated total energy is higher. Schematic illustrations of the Fe *bcc* and *bct* cells are displayed in Supplementary Fig. S9a and b,



Supplementary FIG. S8. Total energies (E_{film}) of free-standing *bcc* and *bct* Fe (001) thin films as a function of number of Fe atomic ML n . The results converge to the total energy of the bulk Fe (E_{bulk}). The curves are guides to the eye.

respectively. The observed tetragonally distorted Fe unit cell in thin Fe films grown on MgAl_2O_4 (001) is schematically displayed in Supplementary Fig. S9c for the 11 Å thick Fe thin film. The dimensions are based on the determined average out-of-plane lattice parameter c_ϕ . Based on the magnetic phase diagram calculated by Moruzzi *et al.* [S15],

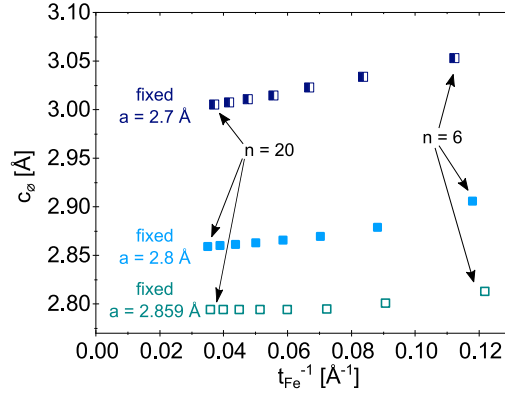


Supplementary FIG. S9. Schematic display of Fe unit cells with different crystal structures: a) *bcc* Fe equilibrium structure with a cubic lattice parameter of 2.866 Å [S19, S20], b) theoretically calculated Fe *bct* crystal structure, and c) experimentally determined crystal structure in 11 Å Fe thin films grown on MgAl_2O_4 (001) assuming fully strained epitaxial growth with clamping at the substrate. Unit cell volumes per atom are displayed below each structure.

ferromagnetism is expected for the *bct* Fe structures observed experimentally and in DFT. The calculated Fe *bct* structure, and the experimentally determined average Fe structure for

11 Å layer thickness have unit cell volumes of 11.55, and 12.16 Å³/atom and c/a ratios of 1.65, and 1.04, respectively and are, hence, well within the ferromagnetic regime [S15, S21].

If the Fe is not calculated free-standing but clamped, i.e., having a fixed in-plane lattice parameter a , the calculated average out-of-plane lattice parameter c_ϕ is shown in Supplementary Fig. S10 for $a = 2.859$, 2.8, and 2.7 Å. The in-plane lattice parameter $a = 2.859$ Å corresponds to the in-plane atomic distance in the MgAl₂O₄ (001) substrate at ambient temperature. Due to thermal expansion, at 0 K this parameter relates however to $c/a < 1$. Nevertheless, for all selected a a profound increase in average out-of-plane lattice parameter c_ϕ is observed for thinner films.



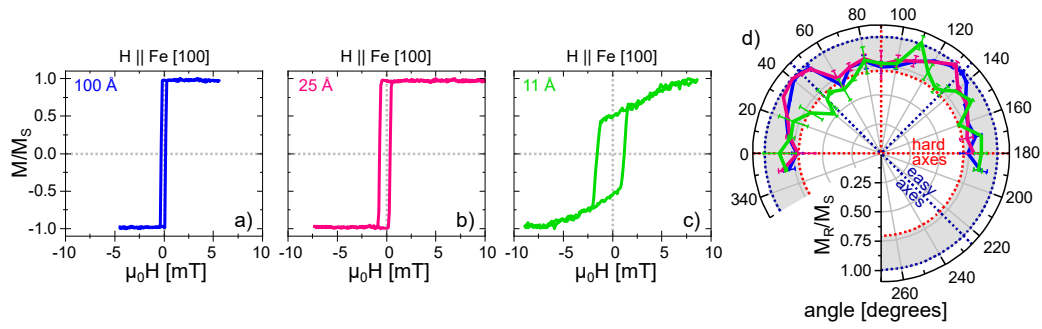
Supplementary FIG. S10. DFT calculated average out-of-plane lattice parameter c_ϕ for fixed in-plane lattice parameters a plotted over inverse Fe layer thickness.

G. Measurements of the magnetic properties at ambient temperature

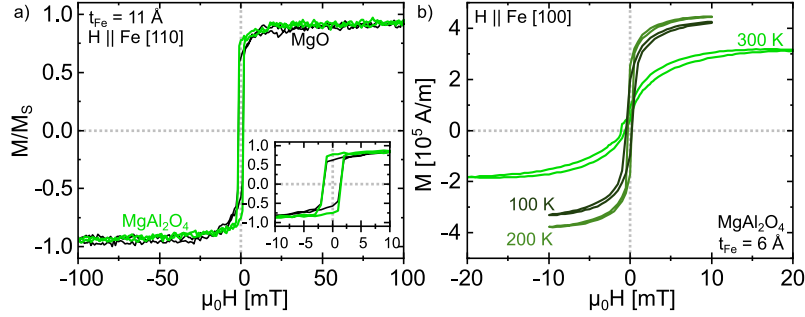
The magnetic properties of Fe thin films with variable thickness grown on MgAl₂O₄ (001) substrates were investigated in a MOKE and a SQUID setup. L-MOKE hysteresis loops of samples with 100, 25, and 11 Å Fe layer thickness for applied fields along Fe [100] are displayed in Supplementary Fig. S11a, b, and c, respectively. While the loops for 100 and 25 Å Fe layer thickness are square-shaped, the loop for the sample with 11 Å Fe layer thickness exhibits a rhombic shape with significantly larger coercivity of around 1.6 mT and higher saturation field hinting towards a change in magnetocrystalline anisotropy, in line

with results reported in literature for structures with from cubic distorted Fe unit cells. For example, tetragonally distorted Fe in MgO/Fe/MgO heterostructures exhibits a growth-induced uniaxial in-plane magnetic anisotropy [S22], in contrast to the fourfold in-plane magnetic anisotropy in *bcc* Fe originating from spin-orbit coupling in combination with the crystalline symmetry. The fourfold crystalline symmetry and 45 degree in-plane rotation of the Fe (001) and MgAl₂O₄ (001) unit cells relative to each other were confirmed for a sample with 144(5) Å Fe layer thickness in polar XRD measurements of MgAl₂O₄ (440) and Fe (110). L-MOKE measurements of the remanent to saturation magnetisation ratio M_R/M_S for samples with 100, 25, and 11 Å Fe layer thickness are shown in Supplementary Fig. S11d. The samples with 25 and 100 Å Fe thickness show both a bulk-like fourfold magnetocrystalline anisotropy. However, the azimuthal angle-dependent remanent state of the sample with 11 Å Fe layer thickness does not show the same behavior, in particular for applied magnetic fields along the expected Fe easy axes, i.e., Fe [100].

At remanence, the magnetisation is not entirely pointing along the expected Fe magnetic easy axis direction for Fe layers of this thickness. To exclude that the magnetisation starts pointing out-of-plane, p-MOKE (magnetic field range up to 1.2 T) and out-of-plane SQUID



Supplementary FIG. S11. a-c) Magnetic hysteresis loops measured with an applied field along [100] direction (one of the magnetic easy axis of bulk Fe) on Fe thin films of different layer thickness grown on MgAl₂O₄ (001) substrates. All samples were capped with 50 Å Pd. d) Azimuthal dependence of the remanent magnetisation for the same samples with 100, 25, and 11 Å Fe layer thickness. The grey shaded area marks the ratios of $M_R/M_S = \sqrt{2}/2$ for a field along a hard axis and $M_R/M_S = 1$ for an easy axis.



Supplementary FIG. S12. Magnetic hysteresis loops a) of 11 Å Fe on MgAl_2O_4 (001) and MgO (001) with an applied field along Fe [100]. Both measurements were performed at ambient temperature. b) Temperature dependent magnetic hysteresis loops measured with an applied field along Fe [100] using SQUID on a 6 Å thick Fe thin film grown on MgAl_2O_4 (001). The samples were capped with a) 50 Å Pd and b) 50 Å Al_2O_3 .

measurements (magnetic field range: 10 mT) were performed. Using SQUID, the Fe magnetic moment was small and of similar magnitude as the diamagnetic contribution due to the substrate, which suggests that the preferred direction of the magnetisation is in-plane (the Fe magnetic moment in the in-plane SQUID measurement is substantially larger using the same magnetic field range). No sign of an out-of-plane magnetisation was found in either of the measurements. However, the existence of an out-of-plane magnetisation component, possibly accounting for the observed reduction in remanent magnetisation for in-plane easy and hard axis measurements of the samples with 6 Å and 11 Å Fe layers, cannot be excluded.

The change in magnetocrystalline anisotropy for thin Fe layers grown on MgAl_2O_4 (001) can be observed in comparison to Fe layers grown on MgO (001) instead (see Supplementary Fig. S12a). For applied fields along Fe [110] hysteresis loops of 11 Å on both substrates exhibit a similar shape, but the sample on MgAl_2O_4 (001) has a higher relative remanence magnetisation M_R/M_S , indicating that the magnetic hard axis in this sample corresponds to a different direction.

H. Temperature dependent measurements of the magnetic properties

The temperature dependence of the measured magnetisation of a sample with 6 Å Fe layer thickness is displayed in the main text and revealed a lowered Curie temperature compared to equilibrium *bcc* Fe. The hysteresis loops measured at 100, 200, and 300 K and displayed in Supplementary Fig. **S12b** confirm the observed change in magnetisation for fields applied along Fe [100], which at an external field of 5 mT is first increasing with decreasing temperature but showing a maximum at around 150 K. Furthermore, a qualitatively similar change in remanence/coercive squareness with temperature is observable.

-
- [S1] C. T. Campbell, *Surf. Sci. Rep.* **27**, 1 (1997).
 - [S2] A. L. Ravensburg, G. K. Pálsson, M. Pohlit, B. Hjörvarsson, and V. Kapaklis, *Thin Solid Films* **761**, 139494 (2022).
 - [S3] M. Björck and G. Andersson, *J. Appl. Crystallogr.* **40**, 1174 (2007).
 - [S4] A. Glavic and M. Björck, *J. Appl. Crystallogr.* **55**, 1063 (2022).
 - [S5] A. L. Ravensburg, J. Bylin, G. K. Pálsson, and V. Kapaklis, arXiv e-prints , arXiv:2310.13539 (2023), arXiv:2310.13539 [cond-mat.mtrl-sci].
 - [S6] A. M. Miller, M. Lemon, M. A. Choffel, S. R. Rich, F. Harvel, and D. C. Johnson, *Z. Naturforsch. B* **77**, 313 (2022).
 - [S7] J. Birch, J. Sundgren, and P. F. Fewster, *J. Appl. Phys.* **78**, 6562 (1995).
 - [S8] M. Birkholz, Principles of X-ray Diffraction, in *Thin Film Analysis by X-Ray Scattering* (John Wiley and Sons, Ltd, 2005) Chap. 1, pp. 1–40.
 - [S9] K. Koepernik and H. Eschrig, *Phys. Rev. B* **59**, 1743 (1999).
 - [S10] H. Eschrig, M. Richter, and I. Opahle, in *Theoretical and Computational Chemistry*, Vol. 14 (Elsevier, 2004) pp. 723–776.
 - [S11] J. P. Perdew, K. Burke, and M. Ernzerhof, *Phys. Rev. Lett.* **77**, 3865 (1996).
 - [S12] M. Methfessel and A. T. Paxton, *Phys. Rev. B* **40**, 3616 (1989).
 - [S13] P. E. Blöchl, O. Jepsen, and O. K. Andersen, *Phys. Rev. B* **49**, 16223 (1994).
 - [S14] J. Schroeder, A. Ingason, J. Rosén, and J. Birch, *J. Cryst. Growth* **420**, 22 (2015).
 - [S15] V. L. Moruzzi, P. M. Marcus, and J. Kübler, *Phys. Rev. B* **39**, 6957 (1989).

- [S16] S. Andrieu, F. L. Razafindramisa, E. Snoeck, H. Renevier, A. Barbara, J. M. Tonnerre, M. Brunel, and M. Piecuch, *Phys. Rev. B* **52**, 9938 (1995).
- [S17] M. Friák, M. Šob, and V. Vitek, *Phys. Rev. B* **63**, 052405 (2001).
- [S18] T. P. A. Hase, M. S. Brewer, U. B. Arnalds, M. Ahlberg, V. Kapaklis, M. Björck, L. Bouchenoire, P. Thompson, D. Haskel, Y. Choi, J. Lang, C. Sánchez-Hanke, and B. Hjörvarsson, *Phys. Rev. B* **90**, 104403 (2014).
- [S19] J. L. Vassent, M. Dynna, A. Marty, B. Gilles, and G. Patrat, *J. Appl. Phys.* **80**, 5727 (1996).
- [S20] G. Chiarotti, 1.6 Crystal structures and bulk lattice parameters of materials quoted in the volume: Datasheet from Landolt-Börnstein - Group III Condensed Matter · Volume 24B: “Electronic and Vibrational Properties” in SpringerMaterials (1994), Springer-Verlag Berlin Heidelberg.
- [S21] V. Martin, W. Meyer, C. Giovanardi, L. Hammer, K. Heinz, Z. Tian, D. Sander, and J. Kirschner, *Phys. Rev. B* **76**, 205418 (2007).
- [S22] Y. Park, E. E. Fullerton, and S. D. Bader, *Appl. Phys. Lett.* **66**, 2140 (1995).



Contents lists available at ScienceDirect

Ultramicroscopy

journal homepage: www.elsevier.com/locate/ultramic



Simulations of magnetic Bragg scattering in transmission electron microscopy

Justyn Snarski-Adamski ^{a,*}, Alexander Edström ^b, Paul Zeiger ^c, José Ángel Castellanos-Reyes ^c, Keenan Lyon ^c, Mirosław Werwiński ^a, Ján Rusz ^c

^a Institute of Molecular Physics, Polish Academy of Sciences, M. Smoluchowskiego 17, 60-179 Poznań, Poland

^b Department of Applied Physics, School of Engineering Sciences, KTH Royal Institute of Technology, AlbaNova University Center, 10691 Stockholm, Sweden

^c Division of Materials Theory, Department of Physics and Astronomy, Uppsala University, Box 516, SE-751 20 Uppsala, Sweden

ARTICLE INFO

Keywords:

Multislice calculations
Antiferromagnetism
Bragg scattering
Transmission electron microscopy
Magnetism

ABSTRACT

We have simulated the magnetic Bragg scattering in transmission electron microscopy in two antiferromagnetic compounds, NiO and LaMnAsO. This weak magnetic phenomenon was experimentally observed in NiO by Loudon (2012). We have computationally reproduced Loudon's experimental data, and for comparison we have performed calculations for the LaMnAsO compound as a more challenging case, containing lower concentration of magnetic elements and strongly scattering heavier non-magnetic elements. We have also described thickness and voltage dependence of the intensity of the antiferromagnetic Bragg spot for both compounds. We have considered lattice vibrations within two computational approaches, one assuming a static lattice with Debye–Waller smeared potentials, and another explicitly considering the atomic vibrations within the quantum excitations of phonons model (thermal diffuse scattering). The structural analysis shows that the antiferromagnetic Bragg spot appears in between (111) and (000) reflections for NiO, while for LaMnAsO the antiferromagnetic Bragg spot appears at the position of the (010) reflection in the diffraction pattern, which corresponds to a forbidden reflection of the crystal structure. Calculations predict that the intensity of the magnetic Bragg spot in NiO is significantly stronger than thermal diffuse scattering at room temperature. For LaMnAsO, the magnetic Bragg spot is weaker than the room-temperature thermal diffuse scattering, but its detection can be facilitated at reduced temperatures.

1. Introduction

The rapid development in nanoengineering of magnetic materials calls for characterization methods at high spatial resolutions describing magnetic phenomena down to the atomic scale. Transmission electron microscopy (TEM) is among the natural choices for such high-resolution characterization of materials. There are many variations of TEM techniques, including high resolution TEM (HRTEM) [1], differential phase contrast (DPC) [2], elemental mapping using electron energy-loss spectroscopy (EELS) [3], scanning transmission electron microscopy (STEM) [4], and Lorentz STEM [5,6]. The study of the magnetic properties of materials can be done using various other techniques, including electron magnetic circular dichroism (EMCD) [7], which is a special case of EELS, magnetic electron holography [8], and recently also magnetic DPC at atomic scale [9–11], among others.

The electron beam consists of moving charged particles, i.e. an electrical current, which is susceptible to the electric and magnetic fields in the sample. By utilizing this interaction, it can be used for

imaging the magnetic structure of materials. In absence of dynamical effects, theoretical understanding of imaging the magnetic structure in DPC method is based on Ehrenfest's theorem [12,13].

With the miniaturization of magnetic technology, there has been recent interest in thin film materials, especially antiferromagnetic materials (AFM) with collinear magnetic moments in light of their potential spintronic applications [14,15]. In Loudon's work [16], it was shown that observation of an antiferromagnetic Bragg spot in TEM is possible in NiO thin films. The antiferromagnetic reflection of magnetic Bragg scattering was found to be 10^4 times less intense than Bragg peaks derived from the structure and was found to clearly stand out from the thermal diffuse scattering (TDS) background. Using a two-beam model, Loudon furthermore estimated the oscillation period of the magnetic reflection to be about 236 nm. These results call for an investigation using a more elaborate computational model in order to understand the visibility of antiferromagnetic Bragg spots as a function of thickness and non-zero temperature.

* Corresponding author.

E-mail addresses: justyn.snarski-adamski@ifmpan.poznan.pl (J. Snarski-Adamski), jan.rusz@physics.uu.se (J. Rusz).

<https://doi.org/10.1016/j.ultramic.2023.113698>

Received 14 October 2022; Received in revised form 19 January 2023; Accepted 2 February 2023

Available online 6 February 2023

0304-3991/© 2023 The Author(s). Published by Elsevier B.V. This is an open access article under the CC BY license (<http://creativecommons.org/licenses/by/4.0/>).

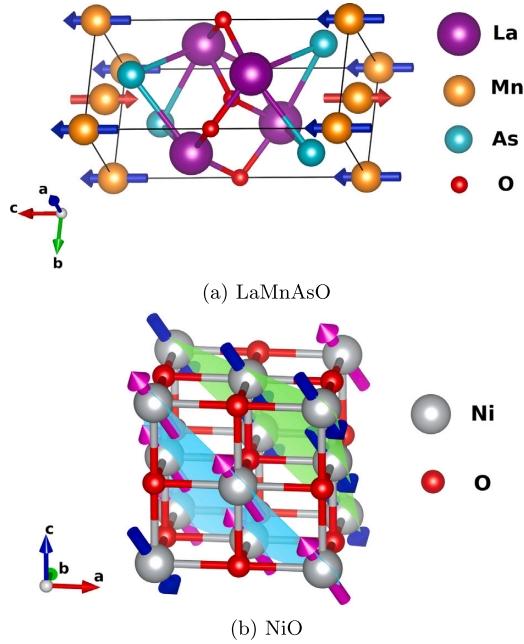


Fig. 1. Crystal structure of (a) LaMnAsO (space group $P4/nmm$) and (b) NiO (space group $Fm\bar{3}m$) with directions of the magnetic moments along one of the easy directions in the light-green and light-blue colored (111)-planes.

In this work, we use a multislice simulation framework based on the paraxial Pauli equation [17,18] to explore the dependence of the intensity of antiferromagnetic Bragg spots both in LaMnAsO (space group $P4/nmm$) and NiO (space group $Fm\bar{3}m$) on sample thickness and acceleration voltage. The lattice parameters of LaMnAsO were set to $a = b = 4.12 \text{ \AA}$, $c = 9.05 \text{ \AA}$, and for NiO $a = b = c = 4.17 \text{ \AA}$ [19,20]. For a selected sample thickness of 123 nm and an acceleration voltage equal to 300 kV, these simulations were also performed with the explicit inclusion of atomic vibrations, leading to thermal diffuse scattering (TDS), in order to compare the intensity of magnetic Bragg spots to the intensity of the TDS background.

Our motivation in choosing NiO for our computational study is largely driven by the experimental results obtained by Loudon [16] and the questions we posed earlier. The choice of the second antiferromagnetic material LaMnAsO in our calculations was motivated by the presence of heavier elements in this compound (La and As), and as a result of that, we expect stronger TDS, potentially making detection of a weak Bragg spot more challenging. In this way, we can qualitatively benchmark the feasibility to detect the magnetic Bragg spot in experiments across a wide range of material compositions and experimental conditions.

2. Computational details

The Pauli multislice method used in this work was described in detail by Edström et al. [17,18] and is based on a paraxial approximation to Pauli's equation,

$$\frac{\partial \Psi}{\partial z} = \frac{im}{\hbar} (\hbar k + eA_z)^{-1} \left\{ \frac{\hbar^2 \nabla_{xy}^2}{2m} + \frac{ie\hbar}{m} \mathbf{A}_{xy} \cdot \nabla_{xy} - \frac{\hbar k e A_z}{m} - \frac{e\hbar}{2m} \boldsymbol{\sigma} \cdot \mathbf{B} + eV \right\} \Psi, \quad (1)$$

instead of Schrödinger's equation used in the standard multislice method [21]. In this equation, V is the electrostatic potential, ∇_{xy} is the in-plane gradient operator, Ψ is a wave function including both spin up and down components (Pauli spinor), and k and m are the relativistic values of the wavenumber and mass of the electron, respectively [22]. The wavefunction is normalized to one, therefore intensities shown in the plots below refer to a fraction of incoming beam intensity.

We note that magnetic Bragg spot intensities calculated for spin-up vs spin-down polarized electron beams differ negligibly. This is because typically the strongest contribution due to magnetism comes from the term $\frac{\hbar k e A_z}{m}$ [13,16], which is insensitive to the spin of the electron beam. Nevertheless, in our simulations we evaluate all terms according to Eq. (1).

The microscopic magnetic vector potential $\mathbf{A}(\mathbf{r})$ and microscopic magnetic field $\mathbf{B}(\mathbf{r})$ were generated using a parametrization described by Lyon and Rusz [23]. This process is based on the superposition of the microscopic magnetic fields and vector potentials, obtained by fitting a quasi-dipole model to the fields obtained via density functional theory for single atoms. It is worth underlining that for TDS calculations we are using Kirkland's parametrization [22], while for static model with included Debye-Waller factors (DWF) Peng's parametrization [24] is implemented. Kirkland's parametrization is using a combination of Gaussians and Lorentzians fitted against tabulated electron scattering data, while Peng's parametrization is based purely on Gaussians, which is particularly convenient for a real-space implementation of the DWF. The main difference between the parametrizations lies in an asymptotic behavior of electron form factors for large scattering angles [25] and that is not affecting our calculations, since the object of our interest — magnetic Bragg spots — are located at low scattering angles (below 10–20 mrad). The cut-off distance of atomic magnetic fields as well as atomic Coulomb potentials both in Kirkland's and Peng's parametrization was set to 4 Å.

We have performed calculations both for a static and a vibrating lattice using a parallel beam (plane-wave) incident orthogonal to the direction of the magnetic moments. This is qualitatively motivated by the Lorentz force, which is maximal when the magnetic field is perpendicular to the beam current, see also Eq. (1) in Ref. [16]. It should be noted that the computational method based on Eq. (1) is generally applicable to describe elastic scattering of paraxial electrons in electric and magnetic fields, and also allows one to simulate other electron microscopy imaging techniques, such as the differential phase contrast microscopy [10,11] or simulate propagation of vortex beams through magnetic materials [17,18].

In our calculations, we use the LaMnAsO and NiO structures shown in Figs. 1(a) and 1(b). The structures were oriented so that the incident beam propagating along the z -axis was orthogonal to the magnetic moment directions parallel to the x -axis in LaMnAsO and y -axis in NiO, respectively. For LaMnAsO, this corresponds to a beam direction [100], while for NiO it is [112]. The LaMnAsO compound, with space group $P4/nmm$ and Néel temperature of $T_N = 360 \text{ K}$, contains magnetic moments only on Mn atoms parallel to c -axis in a so called C-type antiferromagnetic structure [19] (magnetic space group $P4'/n'mm'$), while the NiO (magnetic space group C_2/c) contains an antiferromagnetic distribution of the spin magnetic moments only on Ni atoms. We consider $2.4 \mu_B$ [26] for the magnetic moment of Mn atoms, and $1.7 \mu_B$ [27] for Ni atoms. NiO has a relatively high Néel temperature of $T_N = 523 \text{ K}$ [28]. Directions of magnetic moments in NiO were assumed parallel and anti-parallel to $[1\bar{1}0]$ direction, which corresponds to a spin-flopped configuration [16].

¹ McGuire and Garlea [19] report a different magnetic space group $P4'/n'm'm$, but this is likely a typo, because symmetry operations of $P4'/n'm'm$ are not consistent with C-type antiferromagnetic LaMnAsO having Mn magnetic moments parallel to c -axis.

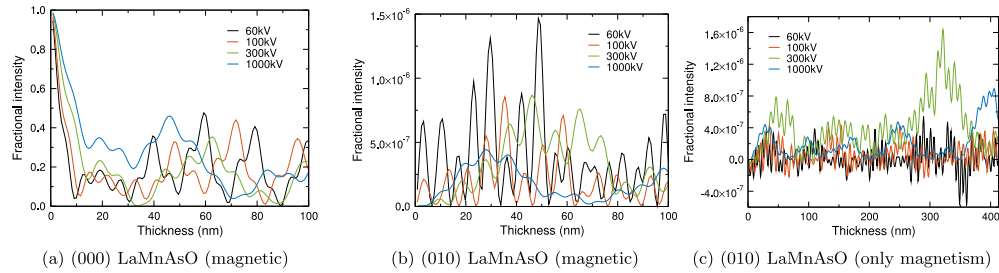


Fig. 2. Voltage and thickness dependence in the static model of (a) the intensity of the direct beam (000), and (b) the magnetic Bragg spots (010) in LaMnAsO. (c) The same as (b), but with subtracted forbidden beam reflections from non-magnetic calculations.

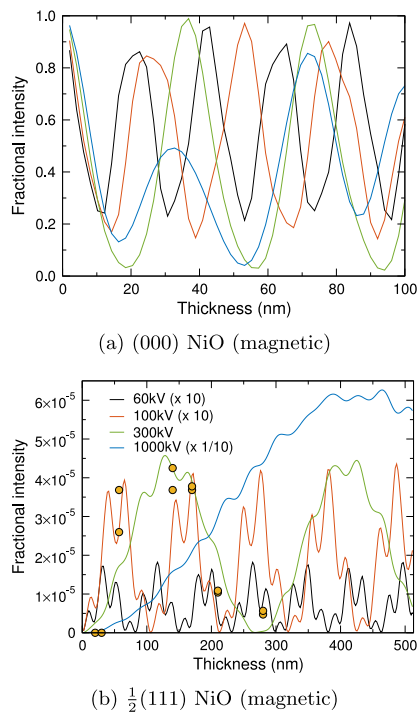


Fig. 3. Voltage and thickness dependence in the static model of (a) the intensity of the direct beam (000), and (b) the intensity of magnetic Bragg spots $\frac{1}{2}(111)$ in NiO. Scaled experimental data (circles) are reproduced from Ref. [16].

Static lattice calculations, where the crystal potential is smeared by DWF, were done both with and without magnetic fields (the latter implemented by setting the **A**- and **B**-fields to zero). In the text below, we refer to these calculations as “static model”. We have done calculations for acceleration voltages of 60, 100, 300, and 1000 kV, respectively. These calculations serve as a qualitative pre-screening of the intensity of the magnetic Bragg spot as a function of acceleration voltage and sample thickness.

LaMnAsO static model calculations were carried out on a grid $184 \times 84 \times 16$ per $9.05 \times 4.12 \times 4.12 \text{ \AA}^3$ unit cell repeated $6 \times 13 \times 300$ times in the *x*, *y*, and *z* directions. For NiO the grid was set to $288 \times 120 \times 48$ pixels per orthogonal supercell of dimensions $14.46 \times 5.90 \times 10.23 \text{ \AA}^3$, which was repeated $2 \times 5 \times 120$ times in the corresponding directions.

To simulate the thermal diffuse scattering (TDS), we have done calculations explicitly including atomic displacements as well as magnetic interactions. These calculations treat both phenomena (vibrations and

Table 1

Experimentally measured mean squared displacement (MSD) at room temperature for LaMnAsO by X-ray powder diffraction [26] and for NiO by neutron powder diffraction [29].

LaMnAsO		NiO	
Atom	MSD [\AA^2]	Atom	MSD [\AA^2]
La	0.00589	Ni	0.00367
Mn	0.00740	O	0.00494
As	0.00680		
O	0.00494		

magnetism) simultaneously and allow for a quantitative comparison of intensities of magnetic Bragg spots and the TDS background, thus offering a quantitative way to assess the feasibility of detecting the magnetic Bragg spots in terms of signal-to-noise ratios (SNR). We assume that the magnetic moments in these calculations remain ordered and oriented perpendicular to the beam, i.e., the effect of temperature on the magnetic moments is not included.

To simulate diffraction patterns, we use an approach based on quantum excitation of phonon (QEP) theory [30] within the Einstein model, where an inelastic signal due to atomic vibrations can be obtained by sampling over possible atomic displacement configurations. The mean squared displacements for each atom in the two compounds analyzed here are specified in Table 1 according to experimental data.

We have generated 250 snapshots with normally distributed (Gaussian) random displacements according to experimental values of MSD. Averaging over intensities of exit wave functions calculated for each of these snapshots results in an incoherent scattering intensity. The exit wave functions were obtained by the paraxial Pauli equation, Eq. (1) above.

The supercell for TDS calculations for LaMnAsO was the size of $18.10 \times 16.49 \times 1236.75 \text{ \AA}^3$ containing 19 200 atoms, and for NiO $28.93 \times 29.52 \times 1227.19 \text{ \AA}^3$ containing 115 200 atoms. Dimensions of these supercells differ from their static counterparts in order to avoid artificial periodicity along the *z*-axis, while keeping the computing costs manageable.

On the same structure models, we have also done calculations excluding magnetic fields, but with atomic vibrations included, in order to estimate the net TDS background.

3. Results

3.1. Static model calculations of thickness and voltage dependence of the intensity of magnetic Bragg scattering

In the first step of our calculations, we have considered the static model including magnetism and tabulated Coulomb potentials smeared by DWF. As mentioned in the previous section, we have tested the influence of the acceleration voltage in the range from 60 to 1000 kV on the intensity of magnetic Bragg scattering and its thickness dependence.

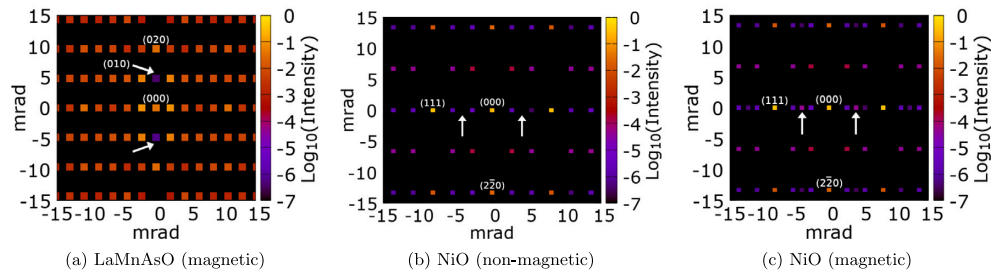


Fig. 4. (a) Diffraction pattern for magnetic LaMnAsO at 300 kV and 123 nm thickness. Diffraction patterns at 300 kV and 123 nm thickness for (b) non-magnetic and (c) magnetic NiO.

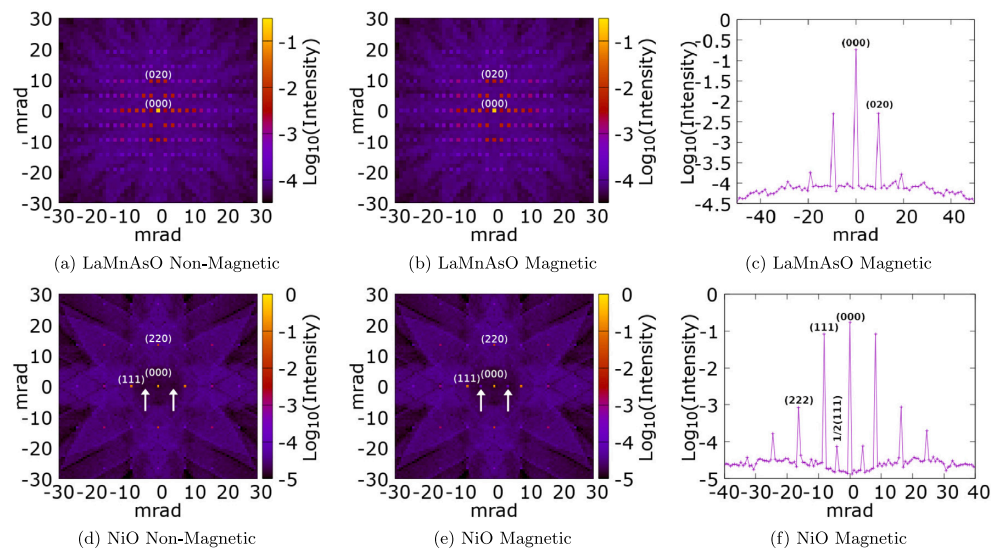


Fig. 5. Quantum excitation of phonon (QEP) calculations with thermal diffuse scattering made for room temperature in (a–c) LaMnAsO and (d–f) NiO. The left column, panels (a) and (d), shows diffraction patterns calculated with zero magnetic fields. Panels (b) and (e) show results with magnetic fields included. Plots (c) and (f) show linear profiles through the diffraction patterns calculated with magnetic fields taken at $\theta_x = 0$ mrad for LaMnAsO and $\theta_y = 0$ mrad for NiO, respectively.

The calculated intensities of the direct beam and at the position of antiferromagnetic Bragg spots are summarized in Figs. 2(a), 2(b), 3(a), and 3(b). For clarity, these results are shown only for samples up to 100 nm thick, except for panel Fig. 3(b), where we include comparison with experiments. Particularly in Fig. 2(b) we see intense oscillations with a relatively short period in thickness. They are remarkably strong at the lowest acceleration voltage of 60 kV. However, these intensities can not be solely ascribed to a magnetic signal. One should note that in the static model calculations, at the position of magnetic Bragg spots, there will generally be a nonzero intensity contribution due to forbidden reflections. Structurally forbidden reflections can have a nonzero intensity in diffraction pattern, when several atomic planes along the beam direction should contribute to achieve the destructive interference [31]. The reason lies in slight changes of the electron beam wave function when propagating through each of these atomic planes. When studying such weak signals as the antiferromagnetic Bragg spots, contributions of forbidden reflections can be, in relative terms, non-negligible. Therefore, we have also recalculated the static model without considering magnetism, and subtracted the obtained forbidden beam reflection intensities from those obtained by magnetic calculations. The results for LaMnAsO (Fig. 2(c); note the extended thickness range) now show a dramatically different picture. The

difference signal becomes strongest for higher acceleration voltages. Occasional negative intensities show that considering the magnetic Bragg peak intensity as an additive signal can only be done approximately. For NiO, the forbidden beam reflections at the position of the magnetic Bragg spot were of much lower intensity than the magnetic signal, so the results in Fig. 3(b) remained visually unchanged by taking the difference (figure not shown).

As can be seen in Fig. 3(b), the magnetic Bragg spot intensity in NiO is significantly lower at acceleration voltages of 60 kV and 100 kV, when compared to 300 kV and, particularly, 1000 kV. However, at 1000 kV, the intensity of the magnetic Bragg spot becomes high only for very large sample thicknesses, which is a disadvantage from the practical point of view. Overall, our results support the choice made by Loudon to use 300 kV acceleration voltage for NiO. Moreover, we note that our simulations at 300 kV show oscillations with the main period of approximately 265 nm, which is in good agreement with experimental data of Loudon [16].

For LaMnAsO the difference between the magnetic and non-magnetic intensity of the Bragg spot, Fig. 2(c), suggests that the acceleration voltage of 300 kV provides an advantage also here. Comparing these results with Fig. 2(b), we note that the intensity of forbidden reflections decreases as the acceleration voltage increases, which can

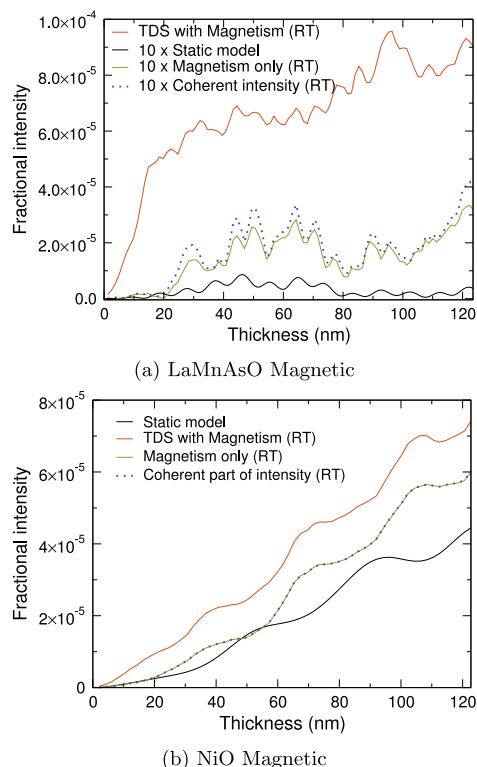


Fig. 6. Plots (a) and (b) show the intensity of the antiferromagnetic Bragg spot for LaMnAsO and NiO, respectively, as a function of the thickness in the static model (black line), from calculations with atomic displacements (orange line), and from the magnetic contribution in the TDS calculations (green line), where the TDS intensity was subtracted. The dark dotted line is obtained as the coherent intensity at the magnetic Bragg spot, calculated from the averaged exit function.

be qualitatively understood, because the modification of the electron beam wave function by a single atomic plane reduces with increasing acceleration voltage.

Figs. 2(a) and 3(a) show, for reference, the thickness dependence of the direct beam (000) in both compounds. Overall, we can see that in relative terms, the magnetic Bragg spot is less intense in LaMnAsO in comparison to NiO. This is likely due to the presence of heavier elements in LaMnAsO, which leads to a stronger Coulomb potential in comparison to NiO and therefore weaker magnetic fields in the relative sense.

Figs. 4(a) and 4(c) show diffraction patterns of the two compounds, including relevant Miller indices and expected positions of magnetic Bragg spots. For NiO we observe in Fig. 4(c) a number of additional spots due to forbidden beam reflections. However, as Fig. 4(b) shows using the calculation excluding magnetic fields, the forbidden beam reflections at the position of the magnetic Bragg spots are of much lower intensity (as was pointed out above) and thus not visible at the chosen color scale.

From the static model calculations, we conclude that in order to detect the magnetic Bragg spots, it appears to be advantageous to use higher acceleration voltages and sample thicknesses of around 100 nm. Motivated by these results, we have chosen 300 kV acceleration voltage and a sample thickness of 123 nm for both systems in calculations that include the atomic displacements.

3.2. Non-magnetic TDS simulations of NiO and LaMnAsO

As a reference for calculations that consider magnetism and atomic vibrations simultaneously, we have performed TDS calculations within Einstein's model approximation, including tabulated Coulomb potentials with zero magnetic fields for both compounds.

TDS calculations are important in the context of estimating the influence of atomic motion and its resulting effects on the diffraction pattern, including the intensities of Bragg spots. Taking this fact into account will help in defining the actual intensity of the antiferromagnetic Bragg spot in relation to the thermal effects overlapping with this weak phenomenon. Knowing these values will also be needed to calculate the acquisition time under which the sample will need to be exposed to the incident electron beam, such that the transmitted electron counts are sufficient to distinguish the antiferromagnetic Bragg spot from the TDS background in the diffraction pattern.

In the case of TDS calculations (at 123 nm and 300 kV) for the LaMnAsO compound, shown in Fig. 5(a), the magnetic (010) reflection is not visible (as expected in these non-magnetic calculations). Similarly, the TDS calculations for NiO are shown in Fig. 5(d), where we can see that without magnetism the $\frac{1}{2}(111)$ reflection is not visible. Both calculations show well-resolved Kikuchi patterns arising from TDS at a relatively large sample thickness. The intensities of the direct beam (000) in these calculations are 0.13 and 0.18 for LaMnAsO and NiO, respectively, with the total intensity normalized to 1.

3.3. TDS simulations of NiO and LaMnAsO including magnetic fields

In this section, we present TDS calculations within Einstein's model approximation, including both electrostatic potentials and magnetic fields.

In the case of NiO we can observe the antiferromagnetic Bragg spot appearing in the $\frac{1}{2}(111)$ spot, see Fig. 5(e). The total intensity of the antiferromagnetic Bragg spot in NiO (at 123 nm and 300 kV) is 7.42×10^{-5} , meaning that approximately 7 electrons for every 100 000 are scattered in the $\frac{1}{2}(111)$ direction. The above value includes the TDS background, whose value was estimated to be 1.41×10^{-5} from a non-magnetic calculation, and 1.51×10^{-5} , within the magnetic calculation from neighboring pixels in the diffraction pattern. These two values are close to each other, as could be expected. Consequently, the signal-to-noise ratio (SNR) for beam current 1 pA and time of the sample exposure 0.1 s is estimated to be above 12, this high value suggesting that the detection of magnetic Bragg spot in NiO at room temperature and a suitable thickness and acceleration voltage is feasible.

In Fig. 6(b) we show the comparison of the thickness dependence in TDS and static model calculations. The two curves show a semi-quantitative agreement, supporting the use of static calculations for a pre-screening of the dependence of the intensity of magnetic Bragg spot on acceleration voltage and sample thickness. In addition, we have used the exit wavefunctions calculated for all structure snapshots to construct an averaged wavefunction. According to the QEP model [30], the averaged exit wavefunction represents a coherent elastic scattering and thus its amplitude squared offers an alternative route to extract the intensity of the magnetic Bragg spot. The result is shown using a dark dotted line and for NiO it is in a very close agreement with the intensity extracted as a difference of magnetic and non-magnetic TDS calculation. The agreement remains excellent also in the LaMnAsO case discussed below.

In the LaMnAsO case, the (010) antiferromagnetic Bragg spot at room temperature is thoroughly covered with TDS intensity, which is stronger than in NiO due to the presence of heavier elements such as La and As in its composition, see Fig. 5(b). Neither the diffraction pattern nor the linear profile passing through the (010) spots (Fig. 5(c)) reveals any peak at the (010) position.

For this reason, we have performed calculations with artificially reduced TDS by decreasing the MSD values by a factor of 10 for each

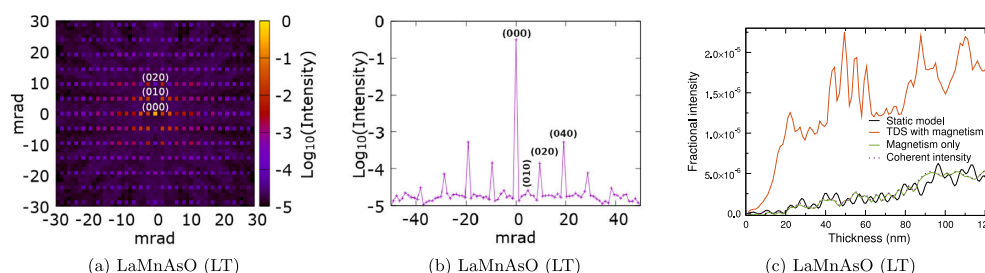


Fig. 7. Panels (a–c) replicate Fig. 5 panels (b–c) and Fig. 6(a), calculated for 10-times reduced mean squared displacement of all atoms, a proxy for low-temperature (LT) calculations.

atom as a simplified model of LaMnAsO at a low temperature. In the harmonic approximation and classical statistical mechanics, that would correspond to a temperature of 30 K. However, this estimate neglects the influence of nuclear quantum effects [32], which eventually become the main contribution to MSD at the lowest temperatures. Based on the actual strength of nuclear quantum effects in LaMnAsO (evaluation of which is outside the scope of this work), the ten-fold reduced MSD would correspond to a temperature below 30 K, though potentially such low MSD might even not be reachable at absolute zero. For the purposes of this work, we consider the ten-fold reduced MSDs as a model for exploring effects of reduced temperature. Results are summarized in Fig. 7.

The resulting reduction of TDS led to an observation of the (010) antiferromagnetic Bragg spot with the total intensity (including the TDS background) equal to 2.64×10^{-5} for the sample thickness 123 nm, making it visible on top of the TDS background intensity. The TDS intensity of 2.12×10^{-5} was extracted from a non-magnetic calculation. The value is again similar to the average intensity of the surrounding pixels (1.93×10^{-5}) in a magnetic calculation. Based on these values, at the same conditions as above (1 pA beam current and 0.1 s dwell time) the SNR would be only slightly above 1. Raising the beam current to 50 pA and keeping the sample exposure time at 0.1 s, the SNR would become larger than 8. Overall, the simulations suggest that the detection of a magnetic Bragg spot in LaMnAsO is substantially more challenging, requiring reduced temperatures, larger beam currents, and/or extended acquisition times than a similar experiment in NiO.

Returning to the room temperature calculation, we can make a simplifying assumption that the magnetic contribution to the intensity of the antiferromagnetic Bragg spot will be approximately the same as in the calculation with reduced MSD — in this way, we would obtain a magnetic signal intensity of 0.53×10^{-5} . For the TDS, we obtain from a non-magnetic calculation 8.7×10^{-5} at this scattering angle. At 1 pA beam current and 0.1 s exposure time, this would lead to a very low SNR of 0.45, well below any detection criterion. One could make the signal detectable by, for example, increasing the beam current to 100 pA, by which the SNR would be raised to about 4.5.

In Fig. 7(c) we compare the thickness dependence of the magnetic Bragg spot intensity obtained in calculations including TDS as well as those from static model calculations. As in Figs. 6(a) and 6(b), we see that the static calculation semi-quantitatively agrees with the calculation including TDS. The agreement between static and QEP calculation is better here than in the aforementioned Figures, which is likely linked to a lower total TDS intensity, since these electrons are effectively removed from the elastic channel and the inclusion of such effect on the intensities of Bragg reflections would require the use of absorptive potentials in the static calculation [33]. On the other hand, the QEP calculation and the difference of magnetic and non-magnetic TDS intensities are both based on a set of calculations with atomic displacements, where the absorption effects are implicitly included. This likely explains their close agreement.

4. Summary and conclusions

We have performed multislice simulations based on the paraxial Pauli equation to investigate the influence of magnetic properties, constituents of the material, and other experimental parameters including acceleration voltage and sample thickness, in antiferromagnetic materials (LaMnAsO and NiO) on their electron diffraction patterns, which can be observed experimentally using transmission electron microscopes.

From our calculations, we observed that for NiO it is quite possible to observe the $\frac{1}{2}(111)$ antiferromagnetic Bragg spot at room temperature as was shown experimentally by Loudon. We have verified that the antiferromagnetic Bragg spot intensity is significantly stronger than the thermal diffuse scattering intensity. Our calculations also provide a good agreement with the measured thickness dependence of the magnetic Bragg spot intensity.

Our simulations for LaMnAsO, containing heavier elements than NiO, suggested that for systems with strong thermal diffuse scattering it can be challenging to detect the magnetic Bragg spots. For such systems, it might be necessary to work at reduced temperatures and/or to perform data acquisition for an extended time with a sufficiently high beam current. The results also indicate the need to select an appropriate acceleration voltage, which for the materials studied here is found to be 300 kV. The simulation methods presented will be valuable in finding favorable experimental settings, paving the way to use TEM for high resolution detection of complex magnetic orders.

CRedit authorship contribution statement

Justyn Snarski-Adamski: Conception and design, Analysis and interpretation of the data, Writing – original draft, Writing – review & editing. **Alexander Edström:** Conception and design, Analysis and interpretation of the data, Writing – original draft, Writing – review & editing. **Paul Zeiger:** Conception and design, Analysis and interpretation of the data, Writing – original draft, Writing – review & editing. **José Ángel Castellanos-Reyes:** Conception and design, Analysis and interpretation of the data, Writing – original draft, Writing – review & editing. **Keenan Lyon:** Conception and design, Analysis and interpretation of the data, Writing – original draft, Writing – review & editing. **Miroslaw Werwiński:** Conception and design, Analysis and interpretation of the data, Writing – original draft, Writing – review & editing. **Ján Rusz:** Conception and design, Analysis and interpretation of the data, Writing – original draft, Writing – review & editing.

Declaration of competing interest

The authors declare that they have no known competing financial interests or personal relationships that could have appeared to influence the work reported in this paper.

Data availability

Data will be made available on request.

Acknowledgments

J.S.-A. gratefully acknowledges financial support from the National Science Center Poland under decision DEC-2019/35/O/ST5/02980 (PRELUDIUM-BIS 1) and National Agency for Academic Exchange Poland under decision PPN/STA/2021/1/00014/U/00001. J.R., P.Z., J.A.C.R., and K.L. acknowledge Swedish Research Council, Olle Engkvist's foundation, Sweden, and Carl Tryggers foundation, Sweden for financial support. A.E. acknowledges Swedish Research Council (2018-06807 and 2022-04720) and the Göran Gustafsson foundation, Sweden for financial support. Part of the calculations was enabled by resources provided by the Swedish National Infrastructure for Computing (SNIC), partially funded by the Swedish Research Council through grant agreement no. 2018-05973. M.W. acknowledges financial support from the National Science Center Poland under decision DEC-2018/30/E/ST3/00267 (SONATA-BIS 8). All authors have approval of the final version.

References

- H.H. Rose, Optics of high-performance electron microscopes, *Sci. Technol. Adv. Mater.* 9 (1) (2008) 014107, <http://dx.doi.org/10.1088/0031-8949/9/1/014107>.
- N. Shibata, S.D. Findlay, Y. Kohno, H. Sawada, Y. Kondo, Y. Ikuhara, Differential phase-contrast microscopy at atomic resolution, *Nat. Phys.* 8 (8) (2012) 611–615, <http://dx.doi.org/10.1038/nphys2337>.
- S.J. Pennycook, M. Varela, A.R. Lupini, M.P. Oxley, M.F. Chisholm, Atomic-resolution spectroscopic imaging: Past, present and future, *J. Electron. Microsc.* (Tokyo) 58 (3) (2009) 87–97, <http://dx.doi.org/10.1093/jmicro/dfn030>.
- R.D. Leapman, Scanning transmission electron microscope (STEM) elemental mapping by electron energy-loss spectroscopy, *Ann. New York Acad. Sci.* 483 (1) (1986) 326–338, <http://dx.doi.org/10.1111/j.1749-6632.1986.tb34539.x>.
- P. Grundy, R. Tebble, Lorentz electron microscopy, *Adv. Phys.* 17 (66) (1968) 153–242, <http://dx.doi.org/10.1080/00018736800101286>.
- K. Harada, K. Shimada, Y. Takahashi, Lorentz scanning electron/ion microscopy, *Microscopy* 71 (2) (2022) 93–97, <http://dx.doi.org/10.1093/jmicro/dfab054>.
- P. Schattschneider, S. Rubino, C. Hébert, J. Ruzs, J. Kuneš, P. Novák, E. Carlino, M. Fabrizio, G. Panaccione, G. Rossi, Detection of magnetic circular dichroism using a transmission electron microscope, *Nature* 441 (7092) (2006) 486–488, <http://dx.doi.org/10.1038/nature04778>.
- J.M. Thomas, E.T. Simpson, T. Kasama, R.E. Dunin-Borkowski, Electron holography for the study of magnetic nanomaterials, *Acc. Chem. Res.* 41 (5) (2008) 665–674, <http://dx.doi.org/10.1021/ar700225v>.
- A. Edström, A. Lubk, J. Ruzs, Quantum mechanical treatment of atomic-resolution differential phase contrast imaging of magnetic materials, *Phys. Rev. B* 99 (17) (2019) 174428, <http://dx.doi.org/10.1103/PhysRevB.99.174428>.
- F. Krizek, S. Reimers, Z. Kašpar, A. Marmodoro, J. Michalička, O. Man, A. Edström, O.J. Amin, K.W. Edmonds, R.P. Campion, F. Maccheronzi, S.S. Dhesi, J. Zubáč, D. Kriegner, D. Carbone, J. Železný, K. Výborný, K. Olejník, V. Novák, J. Ruzs, J.-C. Idrobo, P. Wadley, T. Jungwirth, Atomically sharp domain walls in an antiferromagnet, *Sci. Adv.* 8 (13) (2022) eabn3535, <http://dx.doi.org/10.1126/sciadv.abn3535>.
- Y. Kohno, T. Seki, S.D. Findlay, Y. Ikuhara, N. Shibata, Real-space visualization of intrinsic magnetic fields of an antiferromagnet, *Nature* 602 (7896) (2022) 234–239, <http://dx.doi.org/10.1038/s41586-021-04254-z>.
- K. Müller, F.F. Krause, A. Béché, M. Schowalter, V. Galioit, S. Löffler, J. Verbeeck, J. Zweck, P. Schattschneider, A. Rosenauer, Atomic electric fields revealed by a quantum mechanical approach to electron picodiffraction, *Nature Commun.* 5 (1) (2014) 5653, <http://dx.doi.org/10.1038/ncomms6653>.
- A. Lubk, J. Zweck, Differential phase contrast: An integral perspective, *Phys. Rev. A* 91 (2) (2015) 023805, <http://dx.doi.org/10.1103/PhysRevA.91.023805>.
- T. Jungwirth, X. Marti, P. Wadley, J. Wunderlich, Antiferromagnetic spintronics, *Nat. Nanotechnol.* 11 (3) (2016) 231–241, <http://dx.doi.org/10.1038/nnano.2016.18>.
- P. Wadley, B. Howells, J. Železný, C. Andrews, V. Hills, R.P. Campion, V. Novák, K. Olejník, F. Maccheronzi, S.S. Dhesi, S.Y. Martin, T. Wagner, J. Wunderlich, F. Freimuth, Y. Mokrousov, J. Kuneš, J.S. Chauhan, M.J. Grzybowski, A.W. Rushforth, K.W. Edmonds, B.L. Gallagher, T. Jungwirth, Electrical switching of an antiferromagnet, *Science* 351 (6273) (2016) 587–590, <http://dx.doi.org/10.1126/science.aab1031>.
- J.C. Loudon, Antiferromagnetism in NiO Observed by transmission electron diffraction, *Phys. Rev. Lett.* 109 (26) (2012) 267204, <http://dx.doi.org/10.1103/PhysRevLett.109.267204>.
- A. Edström, A. Lubk, J. Ruzs, Elastic Scattering of Electron Vortex Beams in Magnetic Matter, *Phys. Rev. Lett.* 116 (12) (2016) 127203, <http://dx.doi.org/10.1103/PhysRevLett.116.127203>.
- A. Edström, A. Lubk, J. Ruzs, Magnetic effects in the paraxial regime of elastic electron scattering, *Phys. Rev. B* 94 (17) (2016) 174414, <http://dx.doi.org/10.1103/PhysRevB.94.174414>.
- M.A. McGuire, V.O. Garlea, Short- and long-range magnetic order in LaMnAsO, *Phys. Rev. B* 93 (5) (2016) 054404, <http://dx.doi.org/10.1103/PhysRevB.93.054404>.
- R.W. Cairns, E. Ott, X-Ray studies of the system Nickel–Oxygen–Water. I. Nickelous oxide and Hydroxide1, *J. Am. Chem. Soc.* 55 (2) (1933) 527–533, <http://dx.doi.org/10.1021/ja01329a013>.
- J.M. Cowley, A.F. Moodie, The scattering of electrons by atoms and crystals. I. A new theoretical approach, *Acta Crystallogr.* 10 (10) (1957) 609–619, <http://dx.doi.org/10.1107/S0365110X57002194>.
- E.J. Kirkland, *Advanced Computing in Electron Microscopy*, Springer US, Boston, MA, 2010, <http://dx.doi.org/10.1007/978-1-4419-6533-2>.
- K. Lyon, J. Ruzs, Parameterization of magnetic vector potentials and fields for efficient multislice calculations of elastic electron scattering, *Acta Crystallogr. Sect. Found. Adv.* 77 (6) (2021) 509–518, <http://dx.doi.org/10.1107/S2053273321008792>.
- L.-M. Peng, G. Ren, S.L. Dudarev, M.J. Whelan, Robust Parameterization of Elastic and Absorptive Electron Atomic Scattering Factors, *Acta Crystallogr. A* 52 (2) (1996) 257–276, <http://dx.doi.org/10.1107/S0108767395014371>.
- I. Lobato, D. Van Dyck, An accurate parameterization for scattering factors, electron densities and electrostatic potentials for neutral atoms that obey all physical constraints, *Acta Crystallogr. A* 70 (6) (2014) 636–649, <http://dx.doi.org/10.1107/S205327331401643X>.
- N. Emery, E.J. Wildman, J.M.S. Skakle, A.C. McLaughlin, R.I. Smith, A.N. Fitch, Variable temperature study of the crystal and magnetic structures of the giant magnetoresistant materials LMnAsO (L=La, Nd), *Phys. Rev. B* 83 (14) (2011) 144429, <http://dx.doi.org/10.1103/PhysRevB.83.144429>.
- S.K. Kwon, B.I. Min, Unquenched large orbital magnetic moment in NiO, *Phys. Rev. B* 62 (1) (2000) 73–75, <http://dx.doi.org/10.1103/PhysRevB.62.73>.
- W.L. Roth, Magnetic Structures of MnO, FeO, CoO, and NiO, *Phys. Rev.* 110 (6) (1958) 1333–1341, <http://dx.doi.org/10.1103/PhysRev.110.1333>.
- S. Lee, Y. Ishikawa, P. Miao, S. Torii, T. Ishigaki, T. Kamiyama, Magnetoelastic coupling forbidden by time-reversal symmetry: Spin-direction-dependent magnetoelastic coupling on MnO, CoO, and NiO, *Phys. Rev. B* 93 (6) (2016) 064429, <http://dx.doi.org/10.1103/PhysRevB.93.064429>.
- B.D. Forbes, A.V. Martin, S.D. Findlay, A.J. D'Alfonso, L.J. Allen, Quantum mechanical model for phonon excitation in electron diffraction and imaging using a Born-Oppenheimer approximation, *Phys. Rev. B* 82 (10) (2010) 104103, <http://dx.doi.org/10.1103/PhysRevB.82.104103>.
- K. Nishio, T. Isshiki, H. Saijo, M. Shiojiri, Multi-slice calculation for InP crystals using different slices, *Ultramicroscopy* 54 (2) (1994) 301–309, [http://dx.doi.org/10.1016/0304-3991\(94\)90130-9](http://dx.doi.org/10.1016/0304-3991(94)90130-9).
- A. Löfgren, P. Zeiger, V. Kocovski, J. Ruzs, Influence of nuclear quantum effects on frozen phonon simulations of electron vortex beam HAADF-STEM images, *Ultramicroscopy* 164 (2016) 62–69, <http://dx.doi.org/10.1016/j.ultramic.2016.01.007>.
- A. Weickenmeier, H. Kohl, Computation of absorptive form factors for high-energy electron diffraction, *Acta Crystallogr. A* 47 (5) (1991) 590–597, <http://dx.doi.org/10.1107/S0108767391004804>.



Contents lists available at ScienceDirect

Journal of Magnetism and Magnetic Materials

journal homepage: www.elsevier.com/locate/jmmm



Research articles

Effect of transition metal doping on magnetic hardness of CeFe₁₂-based compounds

Justyn Snarski-Adamski^{*}, Mirosław Werwiński

Institute of Molecular Physics, Polish Academy of Sciences, M. Smoluchowskiego 17, 60-179 Poznań, Poland



ARTICLE INFO

Keywords:

Magnetic anisotropy
FPLO
Rare-earth alloys
Density functional theory
ThMn₁₂, CeFe₁₂

ABSTRACT

ThMn₁₂-type ternary cerium alloys with tetragonal structure (Pearson symbol tI26, space group *I4/mmm*) are considered as promising materials for permanent magnets. In this work, compositions of CeFe₁₁X (s.g. *Pmmn*, No. 59) and CeFe₁₀X₂ (s.g. *P4/mmm*, No. 123) with all 3d, 4d, and 5d transition metal substitutions are considered. Since many previous studies have focused on the CeFe₁₁Ti compound, this particular case became the starting point of our considerations and we gave it special attention. We first determined the optimal symmetry of the simplest CeFe₁₁Ti structure model. We then observed that the calculated magnetocrystalline anisotropy energy (MAE) correlates with the magnetic moment, which in turn strongly depends on the choice of the exchange–correlation potential. MAE, magnetic moments, and magnetic hardness were determined for all compositions considered. Moreover, the calculated dependence of the MAE on the spin magnetic moment allowed us to predict the upper limits of the MAE. We also showed that it does not depend on the choice of the exchange–correlation potential form. The economically justifiable compositions with the highest magnetic hardness values are CeFe₁₁W, CeFe₁₀W₂, CeFe₁₁Mn, CeFe₁₀Mn₂, CeFe₁₁Mo, CeFe₁₀Mo₂, and CeFe₁₀Nb₂. However, calculations suggest that, like CeFe₁₂, these compounds are not chemically stable and could require additional treatments to stabilize the composition. Further alloying of the selected compositions with light elements embedded in interstitial positions confirms the positive effect of such dopants on hard magnetic properties. Subsequent calculations performed for comparison for selected isostructural La-based compounds lead to similar MAE results as for Ce-based compounds, suggesting a secondary effect of 4f electrons. Our preliminary results obtained using the intra-atomic Hubbard repulsion term showed a relatively small difference for CeFe₁₂ compared to the results without this correction. Calculations were performed using the full-potential local-orbital electronic structure code FPLO18, whose unique fully relativistic implementation of the fixed spin moment method allowed us to calculate the MAE dependence of the magnetic moment.

1. Introduction

Rare-earth permanent magnets are used in industries such as automotive, aerospace, electronics, and renewable energy. They are alloys consisting mainly of transition metals and rare-earth elements. They have remarkable magnetic properties, such as very high energy density $[BH]_{max}$ and the ability to operate at high temperatures. Of particular interest are rare-earth compounds such as Nd₂Fe₁₄B [1] and SmCo₅ [2], which exhibit extremely high values of magnetocrystalline anisotropy. However, the high volatility of rare-earth prices, which became clearly evident during the so-called *rare-earth crisis* in 2011 [3], has mobilized the international research community to search for a new generation of hard magnetic materials with reduced rare-earth content [4–10]. This search, although mainly performed by experimental methods, is complemented by groups conducting first-principles calculations of

intrinsic properties and magnetic simulations at the microstructural level.

In the ongoing search for new permanent magnets, special attention is being given to magnetic compounds with ThMn₁₂-type structures based on Nd, Sm, but also less expensive Ce [11,12,12–15]. For example, SmFe₁₁Ti and SmFe₁₁V systems have been found to exhibit uniaxial magnetocrystalline anisotropy [15]. Whereas, the Curie temperature (T_C) measured for SmFe₁₁V is equal to 634 K, the saturation magnetization is 11.2 kG (1.12 T), and the anisotropy field is 8.7 MA m^{−1} [15]. Among Ce compounds with ThMn₁₂-type structure, CeFe₁₁Ti and CeFe_{12−x}Mo_x are particularly interesting. The experimental magnetocrystalline anisotropy energy (MAE) measured at 300 K for CeFe₁₁Ti range from 0.62 to 1.1 MJ m^{−3} [16,17], while the MAE measured at 1.5 K is 1.78 MJ m^{−3} ($H_a = 35$ kOe) [16]. The magnetic moment (m) measured experimentally at 1.5 K is equal to 18.62 μ_B f.u.^{−1} ($\sigma_S = 129.6$ emu g^{−1}) [16], and at 4.5 K is equal to 17.46 μ_B f.u.^{−1} [18],

^{*} Corresponding author.

E-mail address: justyn.snarski-adamski@ifmpan.poznan.pl (J. Snarski-Adamski).

<https://doi.org/10.1016/j.jmmm.2022.169309>

Received 14 October 2021; Received in revised form 22 March 2022; Accepted 22 March 2022

Available online 30 March 2022

0304-8853/© 2022 Elsevier B.V. All rights reserved.

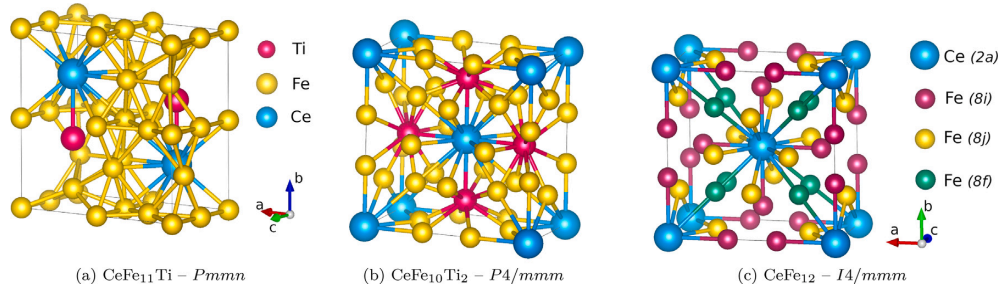


Fig. 1. Crystal structure models of (a) CeFe₁₁Ti (s.g. *Pmmn*, No. 59), (b) CeFe₁₀Ti₂ (s.g. *P4/mmm*, No. 123), and (c) CeFe₁₂ (s.g. *I4/mmm*, No. 139). CeFe₁₂ structure is a superstructure of the ThMn₁₂ type with 2a, 8i, 8j, and 8f Wyckoff positions. The lattice parameters of all models ($a = 8.539$, $c = 4.780$ Å) were adopted from CeFe₁₁Ti [18].

23.14 μ_B f.u.⁻¹ ($\sigma_S = 1.55$ T) [17], while T_C is equal to 487 K [16,18]. Example values of magnetocrystalline anisotropy energy for CeFe₁₁Ti obtained from first-principles calculations are equal to 1.19, 1.50, 1.57, and 1.98 MJ m⁻³ [17,19,20]. For CeFe₁₁Ti, the formation of a hard magnetic phase between the range from 700 and 1100 K has also been both theoretically and experimentally determined [13,21]. Furthermore, experimental analysis of Mo concentration in CeFe_{12-y}Mo_y, where $y = 1, 1.5$, and 2, showed that the T_C for CeFe₁₁Mo is 421 K and decreases with Mo content, while for the nitrided counterpart the T_C is 643 K [14]. $|\text{BH}|_{\text{max}}$ takes the highest value for CeFe₁₁Mo equal to 2.39 kJ m⁻³ after annealing [14].

The aim of this study is to theoretically determine the amount and type of dopants in CeFe₁₂-based alloys that will lead to maximizing their magnetic hardness. The CeFe₁₁X and CeFe₁₀X₂ compositions (X = 3d, 4d, 5d elements) and, for comparison, the thermodynamically unstable CeFe₁₂ compound will be considered.

For rare-earth materials, the simplest theoretical approaches (local-density approximations (LDA)/generalized gradient approximation (GGA)) based on density functional theory (DFT) are often insufficient. Even simple rare earth metals, such as α and γ Ce phases, have recently been extensively studied to identify optimal methods that lead to credible results [22]. Although it is known that LDA/GGA alone usually does not reproduce the properties of Ce compounds well, in this work we chose to use GGA specifically. There are several reasons behind our choice. (1) Our initial calculations going beyond GGA using the intra-atomic Hubbard repulsion term U (GGA + U) showed for CeFe₁₂ relatively good agreement with the GGA results. (2) Complementary calculations for isostructural systems with La (not containing f electrons) in place of Ce, confirmed the dominant effect of Fe on the magnetic properties of the considered compounds. (3) Remaining with GGA, we avoided the computational difficulties associated with more advanced approaches, such as multiple magnetic solutions, and effectively analyzed the MAE dependence on the spin magnetic moment together with the effect of doping on the magnetic properties of CeFe₁₂-based compounds. Recently we also presented a detailed analysis of the effect of the Hubbard U correction on the electronic configuration of Ce in work on the Ce_{1-x}Pr_xCoGe₃ system [23].

Theoretically predicted intrinsic magnetic properties such as magnetization and magnetocrystalline anisotropy energy (MAE) can be used to estimate the upper limits of coercivity and energy product ($|\text{BH}|_{\text{max}}$) [24,25]. The upper coercivity limit is determined by the anisotropy field defined by the formula $H_a = 2 K_1/(\mu_0 M)$, where μ_0 is the free space permeability, M is the magnetization, and K_1 is the anisotropy constant — often approximated as the calculated MAE. In turn, the upper limit of the energy product can be estimated from the formula $|\text{BH}|_{\text{max}} = M^2/(4 \mu_0)$.

While hard magnetic materials typically operate at room temperature and above, the DFT results presented here are calculated for a temperature of 0 K. Therefore, the magnetic moments, magnetocrystalline anisotropy energies, and magnetic hardnesses determined from the calculations should be seen as their upper limits, which typically decrease with increasing temperature.

Table 1

Structural parameters of CeFe₁₂ (s.g. *I4/mmm*, No. 139). In our calculations for the CeFe₁₂ compound, we used the lattice parameters measured for CeFe₁₁Ti, which are $a = 8.539$ and $c = 4.78$ Å, see Ref. [18].

Site	x	y	z
Ce (2a)	0	0	0
Fe (8i)	0.360	0	0
Fe (8j)	0.265	0.5	0
Fe (8f)	0.25	0.25	0.25

2. Computational details

Calculations were performed using the full-potential local-orbital electronic structure code FPLO18 with a fixed atomic-like basis set [26]. The supercell method was used to model all CeFe₁₁X and CeFe₁₀X₂ systems (X = 3d, 4d, and 5d elements). The generalized gradient approximation (GGA) was used in the Perdew–Burke–Ernzerhof (PBE) form [27]. The local spin density approximation (LSDA) in the forms of von Barth and Hedin (BH) [28], Perdew and Zunger (PZ) [29], and Perdew and Wang (PW92) [30] were also used to analyze the effect of the exchange–correlation potential form on the magnetocrystalline anisotropy energy (MAE). A $12 \times 12 \times 12$ k-mesh was found to lead to well converged MAE results. The density convergence criterion was set to 10^{-6} . In all cases, we optimized the geometry with a force convergence criterion of 10^{-3} eV Å⁻¹. A similar systematic supercell approach has been previously applied to model (Fe, Co, X)₂B and (Fe, Co, X)₅PB₂ alloys [31,32].

In addition to the more general rule indicating the choice of PBE among the PBE/LDA exchange–correlation potentials for Fe bcc and Fe compounds with transition metals [33–35], the comparison of magnetic moments obtained by different approximations with experimentally obtained values should be another criterion for making an optimal choice. In the present work the choice of PBE appears to be optimal. However, it should be kept in mind that the results presented in this work, apart from the limitations related to performing calculations for the ground state (0 K), using the supercell method to model chemical disorder, and using a single experimental lattice parameter to model different compounds, may also be affected by the error resulting from the nature of the PBE approximation, which tends to slightly overestimate the obtained values of magnetic moments, which, as we will show, may have some influence on the MAE values obtained.

CeFe₁₂ is expected to crystallize in a tetragonal structure with space group *I4/mmm* [14,15,36], see Table 1 and Fig. 1(c). For all considered models, we assumed lattice parameters as measured for CeFe₁₁Ti [18], while the Wyckoff positions were optimized using a spin-polarized scalar-relativistic approach. For CeFe₁₂, we optimize the atomic positions using various exchange–correlation functionals available in FPLO. For CeFe₁₁Ti, we considered some of the simplest

supercell models with an ideal arrangement of dopant atoms and determined the structure with the lowest total energy (*Pmmn*), see Fig. 1(a). In the case of CeFe₁₀Ti₂ with Ti atoms at 8i sites, there is only one possible crystallographic configuration, with a space group *P4/mmm* (No. 123), see Fig. 1(b). In the case of the presented calculations for “1-11-1” systems doped with light atoms such as C, H, B, and N, we assumed that they occupy 2b sites.

For the “1-10-2” tetragonal system, the MAE was determined as the difference between the fully relativistic total energies calculated for the quantization axes [100] and [001]. For the “1-11-1” system, the MAE was evaluated as the difference between the energies calculated for the orthogonal axes [101] and [010]. We chose the unconventional [101] axis because the space group under consideration (*Pmmn*, No. 59) is orthorhombic. We interpret the energy value obtained for [101] axis as the value averaged between axes [100] and [001]. In the adopted sign convention, the positive sign of the MAE is consistent with an easy axis of magnetization along the [010] direction, and the negative sign is consistent with in-plane anisotropy. Furthermore, we determined the MAE values from a single iteration of the fully-relativistic approach. Using the fully relativistic fixed spin moment scheme [37], we also study the MAE as a function of the total spin magnetic moment (m_S). Tables with the atomic positions of the investigated compounds can be found in the Appendix section. The VESTA code was used to visualize the crystal structures [38].

Another important parameter in the context of permanent magnets is the magnetic hardness, defined as:

$$\kappa = \sqrt{\frac{|K|}{\mu_0 M_S^2}}, \quad (1)$$

where K is the magnetocrystalline anisotropy constant, M_S is the saturation magnetization, and μ_0 is the vacuum permeability. The empirical rule $\kappa > 1$ specifies whether the material will resist self-demagnetization [8]. In determining the theoretical value of κ , we assume that the anisotropy constant K is equal to MAE, and M_S is evaluated from the calculated total magnetic moment and unit cell volume. It is worth noting that the magnetic hardness makes sense only for materials that are proper permanent magnets, and thus have an easy-axis of magnetization rather than an easy-plane. Thus, when MAE < 0 (easy-plane anisotropy), the magnetic hardness parameter loses its meaning [39] and is treated as zero in our calculations.

3. Results and discussion

3.1. Magnetic properties of CeFe₁₂

Previous calculations for CeFe₁₁Ti gave a rather large spread of MAE (from 1.19 to 1.98 MJ m⁻³) accompanied by a similarly large scatter of magnetic moments (from 19.19 to 24.04 μ_B f.u.⁻¹) [17,19,20]. To confirm our conjecture that the obtained differences have their origin in the choice of exchange–correlation potential, we performed MAE and magnetic moment calculations for the parent CeFe₁₂ phase using the BH, PW92, PBE, and LDA exchange-only functionals. The results for various functionals are as follows: BH (MAE = 1.89 MJ m⁻³, m_S = 23.88 μ_B f.u.⁻¹), PW92 (MAE = 1.27 MJ m⁻³, m_S = 24.80 μ_B f.u.⁻¹), PBE (MAE = 0.06 MJ m⁻³, m_S = 26.56 μ_B f.u.⁻¹), and LDA exchange only (MAE = -0.79 MJ m⁻³, m_S = 28.14 μ_B f.u.⁻¹). As can be seen, the range of MAE values obtained is huge, but interestingly they correlate with the magnetic moment values. Looking at Fig. 2, it is easy to notice that these values (green circles) lie on a common straight line.

Further insight into the observed relationship can be gained by a fully relativistic implementation of the fixed spin moment (FSM) method, which allows one to calculate the MAE as a function of the total spin magnetic moment. The results of the MAE(m_S) calculation for the PBE functional confirm that the spin magnetic moment is an important factor affecting the MAE value. Moreover, the MAE(m_S) calculation for another exchange–correlation functional (BH) confirmed that the

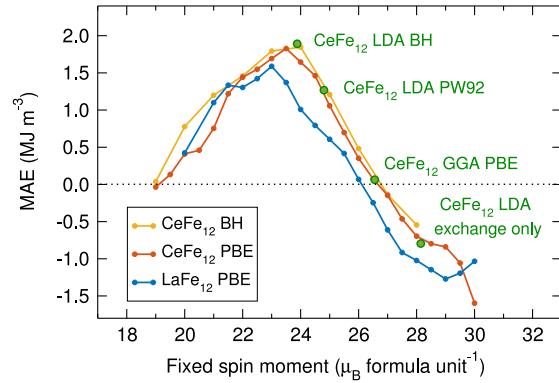


Fig. 2. The magnetocrystalline anisotropy energy (MAE) dependence of the fixed spin moment for CeFe₁₂ calculated with von Barth–Hedin (BH) and Perdew–Burke–Ernzerhof (PBE) exchange–correlation potentials. Together with corresponding PBE results for LaFe₁₂ and equilibrium values for CeFe₁₂ obtained for various functionals. The calculations were performed using the FPLO18 code.

shape of the MAE(m_S) function near the equilibrium magnetic moment does not depend on the choice of the functional itself. Hence, we conclude that the MAE(m_S) function is a more universal fingerprint of the material than the equilibrium MAE values calculated for individual functionals.

Although different exchange–correlation potentials (BH, PW92, and PBE) lead to different values of equilibrium magnetic moments, for a fixed value of magnetic moment, the band structures determined using the different exchange–correlation potentials are nearly equal, leading to almost identical MAE values and thus to a very similar shape of the MAE(m_S) function near the equilibrium magnetic moments. Even relatively small changes in the valence band structure have a significant effect on the MAE value [31,40]. In the case of induced variations in the spin magnetic moment, the occupancy of the spin channels changes, causing shifting the channels with respect to each other, which further leads to the evolution of the MAE(m_S) dependence. The inverted-U-like shape of the MAE(m_S) relation observed for CeFe₁₂ in the vicinity of the equilibrium magnetic moment is its individual feature, and the full dependence (from 0) is a function composed of several oscillations, similar to the Fe₂B case calculated earlier [31].

In calculations of the MAE(m_S) dependence, we observe an almost constant value of the spin magnetic moment on Ce atoms. Forcing a change in the total spin magnetic moment of the system mainly affects the magnetic moments on the Fe atoms, whose main source is the spin polarization of the 3d orbitals. Hence, the observed MAE(m_S) dependence correlates with the evolution of the band structure of the Fe 3d orbitals induced by forcing a change in magnetic moment [31].

The MAE(m_S) result for LaFe₁₂, shown in Fig. 2, will be addressed later in the paper where the effect of 4f electrons on the MAE value will be discussed. The plots for LaFe₁₂ and CeFe₁₂ have a similar shape. In both cases, the decrease in equilibrium magnetic moment leads to an increase in MAE, which reaches maximum values of 1.58 MJ m⁻³ for LaFe₁₂ and 1.82 MJ m⁻³ for CeFe₁₂. The spin and orbital magnetic moments of the CeFe₁₂ compound are presented in Table 2.

3.2. Structural and magnetic properties of CeFe₁₂-based compounds with Ti

3.2.1. Supercell model of CeFe₁₁Ti

To find the simplest supercell to model the composition of CeFe₁₁Ti, we consider five possible non-equivalent substitution configurations of the dopant atom at the Fe (8i) position. The MAEs, total and partial magnetic moments, and the energy difference relative to the lowest energy structure ($E - E_0$) for these five configurations are presented

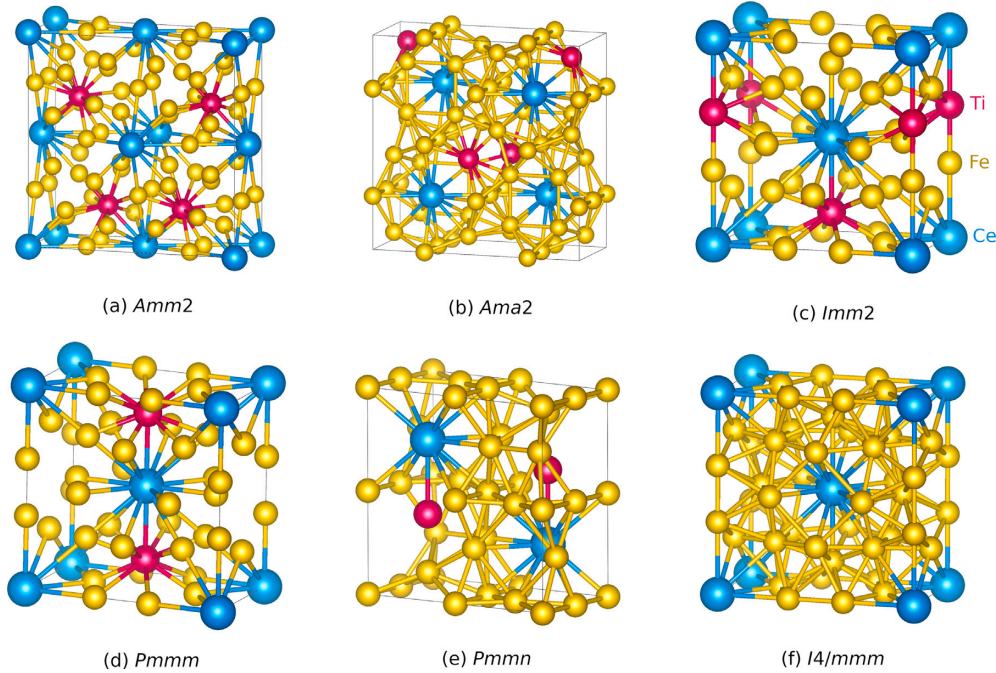


Fig. 3. (a–e) Five orthorhombic crystal structures prepared for CeFe₁₁Ti compound and (f) tetragonal crystal structure for CeFe₁₂.

Table 2

Spin and orbital magnetic moments (μ_B) on Ce, Fe, and Ti atoms in CeFe₁₁Ti (s.g. *Pmmn*, No. 59) and CeFe₁₂ (s.g. *I4/mmm*, No. 139). Calculations were performed with FPLO18 using the PBE functional.

CeFe ₁₁ Ti s.g. <i>Pmmn</i>			CeFe ₁₂ s.g. <i>I4/mmm</i>		
Site	m_s	m_l	Site	m_s	m_l
Ce	-1.13	0.290	Ce	-1.15	0.264
Fe	1.70	0.036	Fe	2.57	0.051
Fe	1.86	0.039	Fe	2.38	0.047
Fe	2.47	0.059	Fe	1.96	0.035
Fe	2.23	0.058			
Fe	2.08	0.050			
Fe	2.33	0.049			
Fe	2.24	0.046			
Ti	-1.26	0.015			

Table 3

The energy difference between the considered structure and the lowest energy structure *Pmmn* [$E - E_0$ (meV)], the magnetocrystalline anisotropy energy [MAE (MJ m⁻³)], the spin magnetic moments on Ce [m_s (Ce)] and Ti [m_s (Ti)], orbital magnetic moment on Ti [m_l (Ti)], total magnetic moment [m], and magnetic hardness [κ] calculated for different possible types of structures of CeFe₁₁Ti compound. Magnetic moments are expressed in μ_B per atom or formula unit. Calculations were performed with FPLO18 using the PBE functional.

S.g.	$E - E_0$	MAE	m_s (Ce)	m_s (Ti)	m_l (Ti)	m	κ
<i>Amm2</i>	31.2	1.14	-1.04	-1.24	0.014	22.01	0.81
<i>Ama2</i>	116.8	1.08	-1.01	-1.22	0.014	21.99	0.79
<i>Imm2</i>	39.8	1.15	-1.10	-1.26	0.014	21.92	0.82
<i>Pmmm</i>	344.6	1.02	-1.08	-1.26	0.010	22.50	0.75
<i>Pmmn</i>	0.0	1.00	-1.10	-1.30	0.015	21.24	0.79

in Table 3. The cell with space group *Pmmn* has the lowest energy among the considered structures, so we choose it as the basic unit cell for the calculation of CeFe₁₁X compounds presented later in this paper. We identify the use of structures with the *Imm2* space group in earlier works [12,13,20,41] as one of the factors that may influence the differences between our and previous results. MAE range obtained for structures with different space groups is from 1.00 to 1.15 MJ m⁻³, and the corresponding range for the total magnetic moment (m) is from 21.24 to 22.50 μ_B f.u.⁻¹. In order to compare the obtained values for CeFe₁₁Ti, the experimental results are presented in Table 4. We find that the presented calculated MAEs are in relatively good agreement with the experimentally obtained low-temperature value (1.78 MJ m⁻³ [16]).

We can see in Table 3 that the spin magnetic moment on the Ce atom is close to $-1 \mu_B$ in all cases. The negative sign in this notation indicates the magnetic moment direction opposite to the ferromagnetic Fe matrix. In the case of the *Pmmn* structure, the spin and orbital magnetic moments on the Ce, Fe, and Ti are shown in Table 2. Comparing the CeFe₁₂ and the Ti doped counterpart, differences in both spin

Table 4

Experimental values of magnetocrystalline anisotropy energy [MAE (MJ m⁻³)] for CeFe₁₁Ti compound obtained from magnetization curves.

Ref.	MAE	T (K)
[16]	0.62	300
[17]	1.10	300
[16]	0.76	300
[16]	1.78	1.5

and orbital moments can be observed. For CeFe₁₂, the spin magnetic moment on the Fe atom is in the range of 1.96–2.57 μ_B , and the corresponding orbital magnetic moment is 0.035–0.051 μ_B . In the case of CeFe₁₁Ti, the spin magnetic moment on the Fe atom is in the range of 1.7–2.47 μ_B and the orbital magnetic moment is 0.036–0.059 μ_B . For both systems, the spin magnetic moment on the Ce atom is similar, however, for the Ti-doped system, the orbital magnetic moment on the Ce atom decreases by 0.026 μ_B .

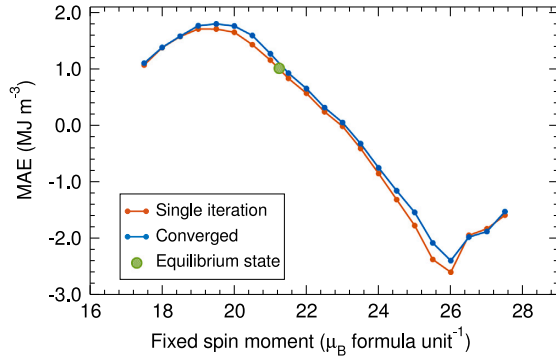


Fig. 4. Magnetocrystalline anisotropy energies (MAEs) as a function of fixed spin moment for the CeFe₁₁Ti compound calculated using full-convergence method (blue line) and the method using a single fully relativistic iteration (orange line). The green point represents the equilibrium value. The calculations were performed using FPLO18 with the PBE functional.

Table 5
Magnetocrystalline anisotropy energy [MAE (MJ m⁻³)], total magnetic moment [*m* (μ_B f.u.⁻¹)], and magnetic hardness [*κ*] for selected CeFe_{12-y}Ti_y compounds. The calculations were performed with FPLO18 using the PBE functional.

Compound	S.g.	MAE	<i>m</i>	<i>κ</i>
CeFe ₁₂	I4/mmm	0.06	26.55	0.16
CeFe _{11.5} Ti _{0.5}	Pmm2	0.59	24.68	0.52
CeFe ₁₁ Ti	Pmmn	1.00	21.24	0.79
CeFe ₁₀ Ti ₂	P4/mmm	1.30	18.04	1.06

3.2.2. Effect of Ti concentration on magnetic properties

Comparing the presented computational results for CeFe₁₂ and CeFe₁₁Ti, we expect that a further increase in the amount of substituent should lead to a further decrease in the total magnetic moment, which in turn, due to the MAE(*m_S*) relation, should lead to an increase in the MAE value. This prediction is tentatively confirmed by the computational results for CeFe_{12-y}Ti_y, where *y* = 0, 0.5, 1, 2, presented in Table 5. We see that the magnetic moment strongly decreases with increasing concentration of Ti and observe a close to linear dependence of MAE(*y*). We also see that for *y* = 2 the result of magnetic hardness is clearly above 1, making this material a potential new permanent magnet.

3.2.3. Fixed spin moment calculations

Fig. 4 presenting the MAE(*m_S*) relation for CeFe₁₁Ti is very similar to the analogous result for CeFe₁₂ shown earlier, see Fig. 2. In both cases, we observe a parabola-shaped relationship with a maximum below the equilibrium magnetic moment. For CeFe₁₁Ti, the MAE maximum of 1.78 MJ m⁻³ occurs for a total spin magnetic moment of 19.5 μ_B f.u.⁻¹, while the equilibrium MAE value is 1.00 MJ m⁻³ for *m_S* = 21.2 μ_B f.u.⁻¹. Comparing again the results for CeFe₁₁Ti and CeFe₁₂, we can interpret the increase in the equilibrium MAE value for CeFe₁₁Ti as the effect of the doping-induced decrease in the total magnetic moment of the system. Furthermore, a comparison of calculations based on a single fully relativistic iteration shown in Fig. 4 with the fully convergent calculations positively verifies the approximation applied, the main advantage of which is a multiple reduction in computation time.

3.2.4. Effect of interstitial dopants on magnetic hardness

To shift the position on the MAE(*m_S*) curve from the equilibrium location towards the observed maximum, we consider the addition of light atoms such as carbon, boron, nitrogen, or hydrogen at the interstitial positions of CeFe₁₂ and CeFe₁₁Ti. From the results presented

Table 6
The magnetocrystalline anisotropy energy [MAE (MJ m⁻³)], total magnetic moment [*m* (μ_B f.u.⁻¹)], and magnetic hardness [*κ*] for CeFe₁₂-based and CeFe₁₁Ti-based compounds with interstitial dopants H, B, C, and N. The calculations were performed with the FPLO18 code using the PBE functional.

Compound	MAE	<i>m</i>	<i>κ</i>
CeFe ₁₂	0.06	26.55	0.16
CeFe ₁₂ H	1.12	25.83	0.69
CeFe ₁₂ C	1.50	25.39	0.81
CeFe ₁₂ N	1.82	27.03	0.84
CeFe ₁₁ Ti	1.00	21.24	0.79
CeFe ₁₁ TiB	1.52	20.96	0.99
CeFe ₁₁ TiN	1.64	22.53	0.95

in Table 6, it can be seen that nitridation allows us to approach the maximum MAE value for the pure CeFe₁₂ compound. The results for CeFe₁₁TiB and CeFe₁₁TiN show that doping with a light atom can increase both the MAE value and the magnetic hardness of the resulting compound.

3.3. Intrinsic magnetic properties of CeFe₁₁X and CeFe₁₀X₂ compounds

3.3.1. Magnetocrystalline anisotropy energy

Since we considered the doping of CeFe₁₁X and CeFe₁₀X₂ with all 3d, 4d, and 5d transition metals, we obtained a complete picture of the MAE changes depending on the type and amount of substituent, see Figs. 5(a) and 5(d) and Table 8. Moreover, the dependence of magnetic hardness (*κ*) on transition metal is shown in Figs. 5(b) and 5(e). It can be seen that the magnetic hardness results are very similar to the MAE trends. Among all CeFe₁₁X compositions, only CeFe₁₁Nb and CeFe₁₁Re can be classified as hard permanent magnets (*κ* > 1), while the values of *κ* for CeFe₁₁W and CeFe₁₁Mo are slightly below the classification criterion, which is still a good indication for further modifications. In the context of potential applications, in addition to the physical parameters, the economic aspect must be taken into account. Thus, although we observe that also Au and Pt significantly increase magnetic hardness, it is difficult to imagine their practical applications. Considering the raw material prices, the economically justified dopant group will include Ti, Cr, Ni, W, Mo, Mn, and Nb. The MAE(*m_S*) dependencies for the selected Ti, W, Mo, and Mn dopants in “1-11-1” system are shown in Fig. 5(c). It can be seen that in each of these cases the CeFe₁₁X compound has the potential to reach the MAE of about 1.5 MJ m⁻³ and *κ* > 1.

MAE calculations of the CeFe₁₀X₂ compositions show that: CeFe₁₀W₂, CeFe₁₀Nb₂, CeFe₁₀Mo₂, and CeFe₁₀Mn₂ can be classified as hard permanent magnets and can be worthy of further investigations. We also calculated MAE(*m_S*) curves for the selected compounds to show that, especially in the case of the CeFe₁₀W₂ compound, there is a possible range for further modification to obtain very high MAE even above 3 MJ m⁻³, see Fig. 5(f). From our enthalpy of formation calculations, it is clear that CeFe₁₁Ti is chemically stable, whereas the considered compounds with W, Mo and Mn are not. In this situation, to obtain the indicated compounds with promising hard magnetic properties, it may be necessary to stabilize them, for example, by partial replacement of Ce with other rare earth elements or complementary replacement of some Fe atoms with an additional element [42,43]. Zhou and Pinkerton described the magnetic hardening of CeFe_{12-x}Mo_x by melt spinning, while revealing a complex multiphase microstructure with “1-12” phase contents ranging from 78 to 87 wt% [14]. Our enthalpy of formation calculations suggest chemical instability of CeFe₁₁Mo and CeFe₁₀Mo₂, which may explain the experimental difficulties in obtaining a homogeneous phase of nominal composition.

Article: Effect of transition metal doping on magnetic hardness of CeFe₁₂-based compounds

J. Snarski-Adamski and M. Werwiński

Journal of Magnetism and Magnetic Materials 554 (2022) 169309

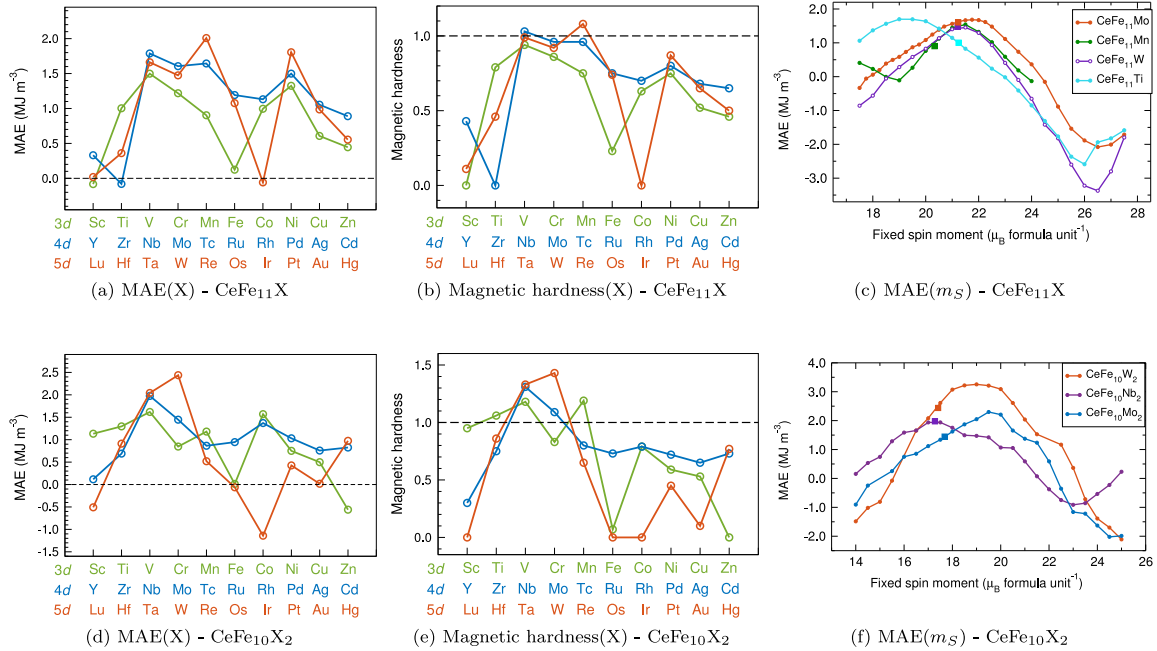


Fig. 5. The hard-magnetic properties of CeFe₁₁X and CeFe₁₀X₂ systems calculated for various 3d, 4d, and 5d transition metals. (a, d) the magnetocrystalline anisotropy energy, (b, e) the magnetic hardness, and (c, f) magnetocrystalline anisotropy energy dependencies of fixed spin moment for the selected elements (X = Mo, Mn, W, Ti for CeFe₁₁X and X = W, Nb, Mo for CeFe₁₀X₂). The squares in the MAE(*m_S*) plots represent equilibrium values. The calculations were performed with FPLO18 using the PBE functional and supercell approach.

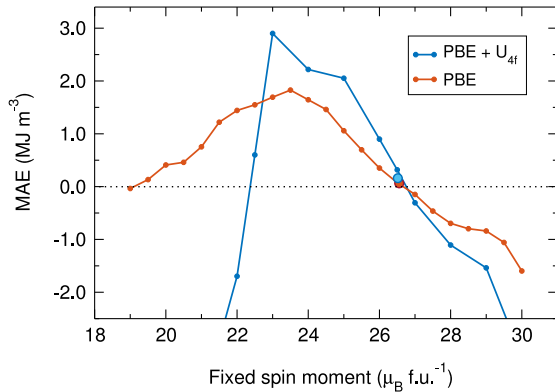


Fig. 6. The magnetocrystalline anisotropy energy (MAE) dependence of the fixed spin moment for CeFe₁₂ calculated with PBE + U exchange–correlation potential, for U equal to 0 and 3 eV, together with corresponding equilibrium values denoted by larger filled circles. The calculations were performed using the FPLO18 code.

3.3.2. Magnetic moments

The results shown in Figs. 7(b) and 7(e) indicate that none of the considered dopant elements at position 8i has a higher spin magnetic moment than the corresponding Fe atom in the reference compound CeFe₁₂. For the CeFe₁₁X compounds considered, the range of spin magnetic moments on the Ce atom is from -0.88 to $-1.15 \mu_B$, and the orbital magnetic moments on the Ce atom is from 0.14 to $0.31 \mu_B$. For doping with Mn, we observe the lowest values of both the total spin magnetic moment and the partial magnetic moment. We also observe that the function of the spin magnetic moments on the substitutions

Table 7

Total spin magnetic moments [*m_S* (μ_B f.u.⁻¹)] and magnetocrystalline anisotropy energies [MAE (MJ m⁻³)] calculated for CeFe₁₂ with different values of Hubbard U (in eV) for PBE + U approach, with U applied to the Ce 4*f* orbitals. The calculations were performed using the FPLO18 code.

U	MAE	<i>m_S</i>
0	0.06	26.56
1	0.25	26.55
2	0.11	26.54
3	0.16	26.52

resembles a sinusoidal function with a minimum and maximum on the positive and negative side of the value interval, see Fig. 7. Results obtained are consistent with previous calculations of the dependence of the total spin magnetic moment on the position of substitution, for example of the 3d elements in NdFe₁₁X system [44]. Analogous trends in the substitution of 5d elements in the 3d matrix have been previously found computationally [32,45,46] and experimentally [47].

3.3.3. Effect of 4f electrons on magnetocrystalline anisotropy

In the heavy-fermion regime, the local magnetic moment of Ce is shielded by conduction electrons that couple to the single Ce 4*f* electron to form a nonmagnetic single state [41]. This kind of heavy-fermionic behavior of Ce has been observed in families “1-5” (CeCo₅) [48] and “2-14-1” (Ce₂Fe₁₄B) [49] of hard-magnetic intermetallics. To determine the effect of 4*f* electrons on the obtained MAE values, we performed MAE(*m_S*) calculations for an isostructural LaFe₁₂ compound with an empty 4*f* shell, see Fig. 2. The relatively small differences observed between the MAE(*m_S*) curves calculated for the LaFe₁₂ and CeFe₁₂ compounds indicate that, at least in the PBE approximation, the effect of the 4*f* shell on the MAE values is small.

Article: Effect of transition metal doping on magnetic hardness of CeFe₁₂-based compounds

J. Snarski-Adamski and M. Werwiński

Journal of Magnetism and Magnetic Materials 554 (2022) 169309

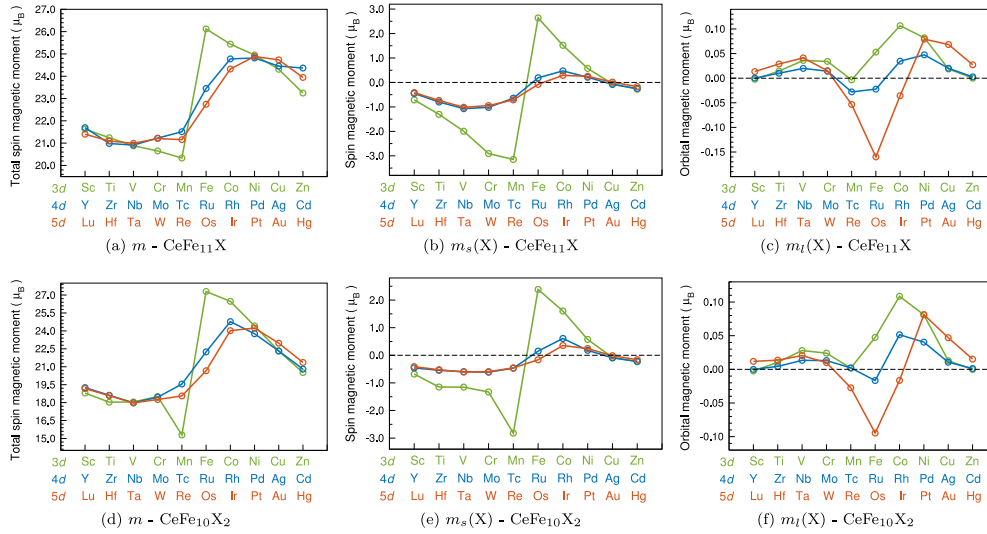


Fig. 7. The magnetic moments of CeFe₁₁X and CeFe₁₀X₂ systems calculated for various 3d, 4d, and 5d transition metals X. (a, d) Total magnetic moments per formula unit and (b, c, e, f) spin and orbital magnetic moments on dopant element X. The calculations were performed with FPLO18 using the PBE functional for quantization axis [010].

Table 8

The magnetocrystalline anisotropy energy [MAE (MJ m⁻³)], total magnetic moment [*m*], magnetic hardness [*κ*], orbital magnetic moment [*m_l*(X)], and spin magnetic moment [*m_s*(X)] calculated for CeFe₁₁X (s.g. *Pnmm*, No. 59) and CeFe₁₀X₂ (s.g. *P4/mmm*, No. 123) with various 3d, 4d, and 5d transition metal elements X in compounds. Magnetic moments are expressed in μ_B per atom or formula unit. Calculations were performed with FPLO18 using the PBE functional.

CeFe ₁₁ X						CeFe ₁₀ X ₂					
3d elements											
	MAE	<i>m</i>	<i>κ</i>	<i>m_l</i> (X)	<i>m_s</i> (X)		MAE	<i>m</i>	<i>κ</i>	<i>m_l</i> (X)	<i>m_s</i> (X)
CeFe ₁₁ Sc	-0.08	22.37	0.00	-0.002	-0.71	CeFe ₁₀ Sc ₂	1.13	18.80	0.95	-0.003	-0.68
CeFe ₁₁ Ti	1.00	21.24	0.79	0.015	-1.30	CeFe ₁₀ Ti ₂	1.30	18.04	1.06	0.011	-1.15
CeFe ₁₁ V	1.50	21.75	0.94	0.036	-2.00	CeFe ₁₀ V ₂	1.62	18.06	1.18	0.028	-1.15
CeFe ₁₁ Cr	1.22	21.51	0.86	0.034	-2.91	CeFe ₁₀ Cr ₂	0.85	18.51	0.83	0.024	-1.33
CeFe ₁₁ Mn	0.90	21.14	0.75	-0.003	-3.15	CeFe ₁₀ Mn ₂	1.18	15.29	1.19	0.002	-2.82
CeFe ₁₁ Fe	0.12	26.12	0.23	0.053	2.64	CeFe ₁₀ Fe ₂	0.01	27.30	0.07	0.048	2.38
CeFe ₁₁ Co	1.00	26.38	0.63	0.107	1.52	CeFe ₁₀ Co ₂	1.57	26.47	0.79	0.109	1.60
CeFe ₁₁ Ni	1.32	25.87	0.75	0.082	0.57	CeFe ₁₀ Ni ₂	0.75	24.42	0.59	0.081	0.57
CeFe ₁₁ Cu	0.61	25.15	0.52	0.019	-0.06	CeFe ₁₀ Cu ₂	0.50	22.32	0.53	0.013	-0.08
CeFe ₁₁ Zn	0.45	24.07	0.46	0.000	-0.27	CeFe ₁₀ Zn ₂	-0.56	20.51	0.00	0.000	-0.24
4d elements											
	MAE	<i>m</i>	<i>κ</i>	<i>m_l</i> (X)	<i>m_s</i> (X)		MAE	<i>m</i>	<i>κ</i>	<i>m_l</i> (X)	<i>m_s</i> (X)
CeFe ₁₁ Y	0.33	22.39	0.43	0.000	-0.45	CeFe ₁₀ Y ₂	0.12	19.26	0.30	0.000	-0.46
CeFe ₁₁ Zr	-0.08	21.72	0.00	0.010	-0.80	CeFe ₁₀ Zr ₂	0.69	18.62	0.75	0.004	-0.54
CeFe ₁₁ Nb	1.79	21.77	1.03	0.020	-1.07	CeFe ₁₀ Nb ₂	1.98	17.98	1.31	0.013	-0.60
CeFe ₁₁ Mo	1.61	22.06	0.96	0.014	-1.02	CeFe ₁₀ Mo ₂	1.45	18.45	1.09	0.013	-0.61
CeFe ₁₁ Tc	1.64	22.30	0.96	-0.028	-0.64	CeFe ₁₀ Tc ₂	0.86	19.55	0.80	0.002	-0.47
CeFe ₁₁ Ru	1.19	24.26	0.75	-0.022	0.19	CeFe ₁₀ Ru ₂	0.95	22.25	0.73	-0.017	0.15
CeFe ₁₁ Rh	1.13	25.65	0.70	0.035	0.47	CeFe ₁₀ Rh ₂	1.37	24.78	0.79	0.052	0.61
CeFe ₁₁ Pd	1.50	25.71	0.80	0.048	0.21	CeFe ₁₀ Pd ₂	1.03	23.76	0.72	0.040	0.18
CeFe ₁₁ Ag	1.05	25.30	0.68	0.020	-0.08	CeFe ₁₀ Ag ₂	0.76	22.32	0.65	0.011	-0.09
CeFe ₁₁ Cd	0.89	24.37	0.65	0.003	-0.25	CeFe ₁₀ Cd ₂	0.83	20.81	0.73	0.001	-0.22
5d elements											
	MAE	<i>m</i>	<i>κ</i>	<i>m_l</i> (X)	<i>m_s</i> (X)		MAE	<i>m</i>	<i>κ</i>	<i>m_l</i> (X)	<i>m_s</i> (X)
CeFe ₁₁ Lu	0.02	22.08	0.11	0.013	-0.41	CeFe ₁₀ Lu ₂	-0.51	19.18	0.00	0.020	-0.41
CeFe ₁₁ Hf	0.36	21.85	0.46	0.029	-0.74	CeFe ₁₀ Hf ₂	0.91	18.58	0.86	0.014	-0.52
CeFe ₁₁ Ta	1.66	21.88	0.99	0.041	-1.02	CeFe ₁₀ Ta ₂	2.04	17.97	1.33	0.020	-0.61
CeFe ₁₁ W	1.47	22.09	0.92	0.015	-0.95	CeFe ₁₀ W ₂	2.44	18.26	1.43	0.010	-0.59
CeFe ₁₁ Re	2.01	22.00	1.08	-0.053	-0.71	CeFe ₁₀ Re ₂	0.52	18.56	0.65	-0.027	-0.46
CeFe ₁₁ Os	1.08	23.56	0.74	-0.160	-0.08	CeFe ₁₀ Os ₂	-0.06	20.67	0.00	-0.095	-0.16
CeFe ₁₁ Ir	-0.06	25.26	0.00	-0.036	0.29	CeFe ₁₀ Ir ₂	-1.14	24.02	0.00	-0.017	0.35
CeFe ₁₁ Pt	1.80	25.89	0.87	0.079	0.25	CeFe ₁₀ Pt ₂	0.43	24.24	0.45	0.081	0.24
CeFe ₁₁ Au	0.99	25.67	0.65	0.069	0.01	CeFe ₁₀ Au ₂	0.02	22.97	0.10	0.047	-0.02
CeFe ₁₁ Hg	0.55	24.76	0.50	0.027	-0.17	CeFe ₁₀ Hg ₂	0.97	21.36	0.77	0.015	-0.16

Table 9
Lattice parameters (in Å) and atomic positions for CeFe₁₀X₂ (s.g. *P4/mmm*, No. 123), CeFe₁₁Ti (s.g. *Pmmn*, No. 59), CeFe₁₂ (s.g. *I4/mmm*, No. 139), and CeFe₁₁TiH (s.g. *I4/mmm*, No. 139). See Fig. 3 for illustrations of the structures. The atomic positions presented for CeFe₁₁TiH were obtained experimentally by Isnard et al. [18].

CeFe ₁₀ X ₂ s.g. <i>P4/mmm</i>				CeFe ₁₁ Ti s.g. <i>Pmmn</i>				CeFe ₁₂ s.g. <i>I4/mmm</i>				CeFe ₁₁ TiH s.g. <i>I4/mmm</i>			
<i>a, b, c</i>	8.539	8.539	4.78	<i>a, b, c</i>	8.539	4.78	8.539	<i>a, b, c</i>	8.539	8.539	4.78	<i>a, b, c</i>	8.566	8.566	4.80
Site	<i>x</i>	<i>y</i>	<i>z</i>	Site	<i>x</i>	<i>y</i>	<i>z</i>	Site	<i>x</i>	<i>y</i>	<i>z</i>	Site	<i>x</i>	<i>y</i>	<i>z</i>
Ce	0.0	0.0	0.0	Ce	0.25	0.25	0.25	Ce	0.0	0.0	0.0	Ce (2a)	0.0	0.0	0.0
Ce	−0.5	−0.5	−0.5	Fe	0.5	0.5	0.5	Fe	0.3582	0.0	0.0	Fe (8i)	0.3534 (6)	0.0	0.0
Fe	0.251	0.251	0.254	Fe	0.5	0.5	0.0	Fe	−0.2275	0.0	0.5	Ti (8i)	0.3534 (6)	0.0	0.0
Ti	0.349	0.0	0.0	Fe	0.89	0.25	0.25	Fe	−0.25	0.25	0.25	Fe (8j)	0.2753 (4)	0.5	0.0
Fe	−0.141	−0.5	−0.5	Fe	0.25	0.25	0.89					Fe (8f)	0.25	0.25	0.25
Fe	0.277	−0.5	0.0	Fe	0.75	0.25	0.515					H (2b)	0.0	0.0	0.5
Fe	−0.219	0.0	−0.5	Fe	0.75	0.25	0.985								
				Fe	0.515	0.25	0.75								
				Ti	0.25	0.25	0.61								

Table 10
Lattice parameters (in Å) and atomic positions for several considered crystal structures of CeFe₁₁Ti with space groups *Amm2* (No. 38), *Ama2* (No. 40), *Imn2* (No. 44), and *Pmmn* (No. 47). See Fig. 3 for illustrations of the structures.

<i>Amm2</i>				<i>Ama2</i>				<i>Imn2</i>				<i>Pmmn</i>			
<i>a, b, c</i>	4.78	12.075	12.075	<i>a, b, c</i>	4.78	12.075	12.075	<i>a, b, c</i>	4.78	8.539	8.539	<i>a, b, c</i>	8.539	8.539	4.78
site	<i>x</i>	<i>y</i>	<i>z</i>	site	<i>x</i>	<i>y</i>	<i>z</i>	site	<i>x</i>	<i>y</i>	<i>z</i>	site	<i>x</i>	<i>y</i>	<i>z</i>
Ce	0	0	0	Ce	0.25	0.75	0.25	Ce	0	0	0	Ce	0.5	0.5	0.5
Ce	0.5	0.5	0	Fe	0.5	0.25	0	Fe	0.75	0.75	0.0025	Ce	0	0	0
Fe	0.25	0.75	0	Fe	0.5	0.5	0.25	Fe	0	0.64	0	Fe	0.75	0.75	0.75
Fe	0.25	0.5	0.25	Fe	0.5	0	0.25	Fe	0	0	0.36	Fe	0.5	0.14	0.5
Fe	0.25	0	0.25	Fe	0.25	0.93	0.07	Fe	0.5	0	0.235	Fe	0.36	0	0
Fe	0	0.32	0.32	Fe	0.25	0.57	0.07	Fe	0	0.5	0.265	Fe	0	0.36	0
Fe	0.5	0.32	0.18	Fe	0.25	0.57	0.43	Fe	0	0.265	0.5	Fe	0.765	0	0.5
Fe	0.5	0.18	0.32	Fe	0.25	0.1325	0.1325	Fe	0	0	0.64	Fe	0	0.765	0.5
Fe	0	0.1175	0.3825	Fe	0.25	0.3675	0.3675	Ti	0	0	0	Fe	0.265	0.5	0
Fe	0	0.3825	0.1175	Fe	0.25	0.3675	0.1325					Fe	0.5	0.265	0
Fe	0.5	0.6175	0.3825	Fe	0.25	0.1325	0.3675					Ti	0.86	0.5	0.5
Fe	0.5	0.8825	0.1175	Ti	0.25	0.93	0.43								
Ti	0	0.82	0.18												

Subsequent MAE calculations for LaFe₁₁Ti (0.66 MJ m^{−3}), CeFe₁₁Ti (1.00 MJ m^{−3}), LaFe₁₀W₂ (1.91 MJ m^{−3}), and CeFe₁₀W₂ (2.43 MJ m^{−3}) also confirm the secondary effect of the 4*f* shell on the MAE values in these compounds. Since La and Ce are extracted in large quantities during the mining of Nd-containing rare earth ores, both of these elements may play an important role in the development of lower-cost high-performance permanent magnets.

Finally, we would like to briefly discuss how the use of the intra-atomic Hubbard repulsion term *U* (GGA + *U*) affects the obtained results. For this purpose, we performed PBE + *U* calculations of the magnetic properties for the example compound CeFe₁₂. With increasing *U* in the range from 0 to 3 eV, the equilibrium total spin magnetic moment slightly decreases, see Table 7. The introduction of intra-atomic repulsion also affects the MAE value raising it from 0.06 MJ m^{−3} for *U* = 0 to 0.16 MJ m^{−3} for *U* = 3 eV. The observed changes are rather not qualitative, which allow us to conclude that the use of the PBE approximation in this work was justified. The results of calculations of the magnetocrystalline anisotropy energy (MAE) dependence on the fixed spin moment with PBE + *U*, see Fig. 6, lead to similar conclusions. Although the differences between the results without and with Hubbard *U* correction are clear, in both cases we obtain similar equilibrium state properties and qualitatively similar relations showing the MAE maximum for reduced magnetic moments.

4. Summary and conclusions

Using density functional theory, we investigated the magnetic properties of the compounds CeFe₁₁X and CeFe₁₀X₂ with all 3*d*, 4*d*, and 5*d* transition metals. As a starting example we used the CeFe₁₁Ti system, for which we determined the simplest model of the crystal structure and further studied how changing the Ti concentration affects the obtained magnetic properties. We found that in the doping range of 0 to 2 Ti atoms per 12 Fe atoms, an increase in

Ti concentration leads to a decrease in the total magnetic moment and a significant increase in the magnetocrystalline anisotropy energy (MAE) and magnetic hardness. Using the fully relativistic fixed spin moment method, we calculated for CeFe₁₁Ti the dependence of the MAE on the spin magnetic moment, which confirmed the expected relation that MAE increases with decreasing magnetic moment. An almost identical dependence of the magnetocrystalline anisotropy energy on the magnetic moment as for CeFe₁₁Ti was observed for the parent compound CeFe₁₂. We also showed that the discussed relation of the anisotropy energy on the magnetic moment practically does not depend on the choice of the exchange–correlation potential. On the other hand, the equilibrium magnetic moment values obtained depend very strongly on the choice of the exchange–correlation potential, which indirectly affects the anisotropy energy values and leads to a very wide range of results, from strongly negative to strongly positive. Additional calculations for CeFe₁₂ and CeFe₁₁Ti-based alloys with smaller elements such as B, C, and N placed in interstitial positions showed that such doping can lead to a decrease in the total magnetic moment and an accompanying increase in the MAE.

After a detailed analysis of the structure model of CeFe₁₁Ti and verification of the fixed spin moment method, we performed systematic calculations for the CeFe₁₁X and CeFe₁₀X₂ compounds considering the full range of transition metal dopants. We have presented and discussed the courses of dependence of magnetic moments and magnetocrystalline anisotropy energy on the type of dopant. Compositions showing very high magnetic hardness include CeFe₁₁W, CeFe₁₀W₂, CeFe₁₁Mn, CeFe₁₀Mn₂, CeFe₁₁Mo, CeFe₁₀Mo₂, and CeFe₁₀Nb₂.

Furthermore, we also determined the effect of 4*f* electrons on the obtained MAE values by performing MAE(*m_S*) calculations for isostructural LaFe₁₂ and equilibrium calculations of LaFe₁₁Ti and LaFe₁₀W₂ compounds with empty 4*f* shell. By comparing the obtained results for the corresponding systems with Ce, we found a secondary effect of the 4*f* shell on the MAE value in these systems. We also found that the

Article: Effect of transition metal doping on magnetic hardness of CeFe₁₂-based compounds

J. Snarski-Adamski and M. Werwiński

Journal of Magnetism and Magnetic Materials 554 (2022) 169309

application of the intra-atomic Hubbard repulsion term U (GGA + U) for the CeFe₁₂ test case does not induce qualitative differences in the obtained results between GGA and GGA + U results, which justifies the use of the PBE approximation throughout the paper.

CRediT authorship contribution statement

Justyn Snarski-Adamski: Conceptualization, Methodology, Validation, Formal analysis, Investigation, Writing – original draft, Data curation, Writing – review & editing. **Miroslaw Werwiński:** Conceptualization, Methodology, Validation, Formal analysis, Investigation, Writing – original draft, Resources, Data curation, Writing – review & editing, Supervision, Project administration, Funding acquisition.

Declaration of competing interest

The authors declare that they have no known competing financial interests or personal relationships that could have appeared to influence the work reported in this paper.

Acknowledgments

We gratefully acknowledge financial support from the National Science Center Poland under decisions DEC-2019/35/O/ST5/02980 (PRELUDIUM-BIS 1) and DEC-2018/30/E/ST3/00267 (SONATA-BIS 8). We thank Paweł Leśniak and Daniel Depcik for compiling the scientific software and administering the computational cluster at the Institute of Molecular Physics, Polish Academy of Sciences.

Appendix

The lattice parameters and atomic positions of the considered systems “1-11-1” and “1-10-2” and the compound CeFe₁₂ are presented in Tables 9 and 10. The presented parameters relate directly to the crystallographic structures illustrated in Figs. 1(b) and 3. In the present work the structures shown in Table 9 are used. CeFe₁₁TiH structure is shown for the comparison as an experimental result [18].

References

- [1] Y. Toga, M. Nishino, S. Miyashita, T. Miyake, A. Sakuma, Anisotropy of exchange stiffness based on atomic-scale magnetic properties in the rare-Earth permanent magnet Nd₂Fe₁₄B, *Phys. Rev. B* 98 (5) (2018) 054418.
- [2] B. Das, R. Choudhary, R. Skomski, B. Balasubramanian, A.K. Pathak, D. Paudyal, D.J. Sellmyer, Anisotropy and orbital moment in Sm-Co permanent magnets, *Phys. Rev. B* 100 (2) (2019) 024419.
- [3] K. Bourzac, The rare-Earth crisis, *Techn. Rev.* 114 (3) (2011) 58–63.
- [4] D. Niarchos, G. Giannopoulos, M. Gjoka, C. Sarafidis, V. Psycharis, J. Ruzs, A. Edström, O. Eriksson, P. Toson, J. Fidler, E. Anagnostopoulou, U. Sanyal, F. Ott, L.-M. Lacroix, G. Viau, C. Bran, M. Vazquez, L. Reichel, L. Schultz, S. Fähler, Toward rare-Earth-free permanent magnets: A combinatorial approach exploiting the possibilities of modeling, shape anisotropy in elongated nanoparticles, and combinatorial thin-film approach, *JOM J. Miner. Met. Mater. Soc.* 67 (6) (2015) 1318–1328.
- [5] S. Hirose, Current status of research and development toward permanent magnets free from critical elements, *J. Magn. Soc. Jpn.* 39 (3) (2015) 85–95.
- [6] D. Li, D. Pan, S. Li, Z. Zhang, Recent developments of rare-Earth-free hard-magnetic materials, *Sci. China Phys. Mech. Astron.* 59 (1) (2015) 617501.
- [7] S. Hirose, M. Nishino, S. Miyashita, Perspectives for high-performance permanent magnets: Applications, coercivity, and new materials, *Adv. Nat. Sci. Nanosci. Nanotechnol.* 8 (1) (2017) 013002.
- [8] R. Skomski, J.M.D. Coey, Magnetic anisotropy — How much is enough for a permanent magnet? *Scr. Mater.* 112 (2016) 3–8.
- [9] S. Ener, K.P. Skokov, D. Palanisamy, T. Devillers, J. Fischbacher, G.G. Eslava, F. Maccari, L. Schäfer, L.V.B. Diop, I. Radulov, B. Gault, G. Hrkač, N.M. Dempsey, T. Schrefl, D. Raabe, O. Gutfleisch, Twins — A weak link in the magnetic hardening of ThMn₁₂-type permanent magnets, *Acta Mater.* (2021) 116968.
- [10] M. Werwiński, W. Marciniak, Ab initio study of magnetocrystalline anisotropy, magnetostriction, and Fermi surface of Li₉ FeNi (tetraenaite), *J. Phys. D: Appl. Phys.* 50 (49) (2017) 495008.

- [11] O. Gutfleisch, M.A. Willard, E. Brück, C.H. Chen, S.G. Sankar, J.P. Liu, Magnetic materials and devices for the 21st century: stronger, lighter, and more energy efficient, *Adv. Mater.* 23 (7) (2011) 821–842.
- [12] P. Delange, S. Biermann, T. Miyake, L. Pourovskii, Crystal-field splittings in rare-Earth-based hard magnets: An Ab initio approach, *Phys. Rev. B* 96 (15) (2017) 155132.
- [13] H.I. Sözen, S. Ener, F. Maccari, K.P. Skokov, O. Gutfleisch, F. Körmann, J. Neugebauer, T. Hickel, Ab initio phase stabilities of Ce-based hard magnetic materials and comparison with experimental phase diagrams, *Phys. Rev. Mater.* 3 (8) (2019) 084407.
- [14] C. Zhou, F.E. Pinkerton, Magnetic hardening of CeFe_{12-x}Mo_x and the effect of nitrogenation, *J. Alloys Compd.* 583 (2014) 345–350.
- [15] G.C. Hadjipanayis, A.M. Gabay, A.M. Schönhöbel, A. Martín-Cid, J.M. Barandiaran, D. Niarchos, ThMn₁₂-Type alloys for permanent magnets, *Engineering* 6 (2) (2020) 141–147.
- [16] Q. Pan, Z.-X. Liu, Y.-C. Yang, Structural and magnetic properties of Ce(Fe,M)₁₂N_x interstitial compounds, M=Ti, V, Cr, and Mo, *J. Appl. Phys.* 76 (10) (1994) 6728–6730.
- [17] M. Akayama, H. Fujii, K. Yamamoto, K. Tatami, Physical properties of nitrogenated RFe₁₁Ti intermetallic compounds (R=Ce, Pr and Nd) with ThMn₁₂-type structure, *J. Magn. Magn. Mater.* 130 (1) (1994) 99–107.
- [18] O. Isnard, S. Miraglia, M. Guillot, D. Fruchart, Hydrogen effects on the magnetic properties of RFe₁₁Ti compounds, *J. Alloys Compd.* 275–277 (1998) 637–641.
- [19] L. Ke, D.D. Johnson, Intrinsic magnetic properties in R(Fe_{1-x}Co_x)₁₁TiZ (R=Y and Ce; Z=H, C, and N), *Phys. Rev. B* 94 (2) (2016) 024423.
- [20] R. Martínez-Casado, A. Dasmahapatra, M.F. Sgroi, C. Romero-Muñiz, H.C. Herper, O.Y. Vekilova, A.M. Ferrari, D. Pullini, J. Desmarais, L. Maschio, The CeFe₁₁Ti permanent magnet: A closer look at the microstructure of the compound, *J. Phys.: Condens. Matter* 31 (50) (2019) 505505.
- [21] F. Maccari, S. Ener, D. Koch, I. Dirba, K.P. Skokov, E. Bruder, L. Schäfer, O. Gutfleisch, Correlating changes of the unit cell parameters and microstructure with magnetic properties in the CeFe₁₁Ti compound, *J. Alloys Compd.* 867 (2021) 158805.
- [22] F. Tran, F. Karsai, P. Blaha, Nonmagnetic and ferromagnetic fcc cerium studied with one-electron methods, *Phys. Rev. B* 89 (15) (2014) 155106.
- [23] P. Skokowski, K. Synoradzki, M. Werwiński, T. Toliński, A. Bajorek, G. Chelkowska, Influence of Pr substitution on the physical properties of the Ce_{1-x}Pr_xCoGe₃ system: Combined experimental and first-principles study, *Phys. Rev. B* 102 (24) (2020) 245127.
- [24] J.M.D. Coey, Permanent magnets: Plugging the gap, *Scr. Mater.* 67 (6) (2012) 524–529.
- [25] W. Körner, G. Krugel, C. Elsässer, Theoretical screening of intermetallic ThMn₁₂-type phases for new hard-magnetic compounds with low rare Earth content, *Sci. Rep.* 6 (1) (2016) 24686.
- [26] K. Koepnick, H. Eschrig, Full-potential nonorthogonal local-orbital minimum-basis band-structure scheme, *Phys. Rev. B* 59 (3) (1999) 1743–1757.
- [27] J.P. Perdew, K. Burke, M. Ernzerhof, Generalized gradient approximation made simple, *Phys. Rev. Lett.* 77 (18) (1996) 3865–3868.
- [28] U. von Barth, L. Hedin, A local exchange-correlation potential for the spin polarized case. i, *J. Phys. C: Solid State Phys.* 5 (13) (1972) 1629.
- [29] J.P. Perdew, A. Zunger, Self-interaction correction to density-functional approximations for many-electron systems, *Phys. Rev. B* 23 (10) (1981) 5048–5079.
- [30] J.P. Perdew, Y. Wang, Accurate and simple analytic representation of the electron-gas correlation energy, *Phys. Rev. B* 45 (23) (1992) 13244–13249.
- [31] A. Edström, M. Werwiński, D. Jušan, J. Ruzs, O. Eriksson, K.P. Skokov, I.A. Radulov, S. Ener, M.D. Kuz'min, J. Hong, M. Fries, D.Y. Karpenkov, O. Gutfleisch, P. Toson, J. Fidler, Magnetic properties of (Fe_{1-x}Co_x)₂B alloys and the effect of doping by 5d elements, *Phys. Rev. B* 92 (17) (2015) 174413.
- [32] M. Werwiński, A. Edström, J. Ruzs, D. Hedlund, K. Gunnarsson, P. Svedlindh, J. Cedervall, M. Sahlberg, Magnetocrystalline anisotropy of Fe₃PB₂ and its alloys with Co and 5d elements: A combined first-principles and experimental study, *Phys. Rev. B* 98 (21) (2018) 214431.
- [33] F. Körmann, A. Dick, T. Hickel, J. Neugebauer, Pressure dependence of the curie temperature in bcc iron studied by Ab initio simulations, *Phys. Rev. B* 79 (18) (2009) 184406.
- [34] M. Matyunina, M. Zagrebin, V. Sokolovskiy, V. Buchelnikov, Ab initio study of magnetic and structural properties of Fe-Ga alloys, *EPJ Web Conf.* 185 (2018) 04013.
- [35] A.H. Romero, M.J. Verstraete, From one to three, exploring the rungs of Jacob's ladder in magnetic alloys, *Eur. Phys. J. B* 91 (8) (2018) 193.
- [36] J. Lee, S. Ryu, I. Kim, M. Byeon, M.-H. Jeong, J.S. Lee, T.E. Hong, J. Cho, J. Lee, J.K. Park, H. Jeon, Large enhancement of magnetic moment in nitridated CeFe₁₂, *J. Alloys Compd.* 886 (2021) 161245.
- [37] K. Schwarz, P. Mohn, Itinerant metamagnetism in YCo₂, *J. Phys. F: Met. Phys.* 14 (7) (1984) L129.
- [38] K. Momma, F. Izumi, VESTA: A three-dimensional visualization system for electronic and structural analysis, *J. Appl. Crystallogr.* 41 (3) (2008) 653–658.

- [39] P. Nieves, S. Arapan, J. Maudes-Raedo, R. Marticorena-Sánchez, N.L. Del Brío, A. Kovacs, C. Echevarria-Bonet, D. Salazar, J. Weischenberg, H. Zhang, O.Y. Vekilova, R. Serrano-López, J.M. Barandíaran, K. Skokov, O. Gutfleisch, O. Eriksson, H.C. Herper, T. Schrefl, S. Cuesta-López, Database of novel magnetic materials for high-performance permanent magnet development, *Comput. Mater. Sci.* 168 (2019) 188–202.
- [40] T. Burkert, L. Nordström, O. Eriksson, O. Heinonen, Giant magnetic anisotropy in tetragonal FeCo alloys, *Phys. Rev. Lett.* 93 (2) (2004) 027203.
- [41] A. Galler, S. Ener, F. Maccari, I. Dirba, K.P. Skokov, O. Gutfleisch, S. Biermann, L.V. Pourovskii, Intrinsically weak magnetic anisotropy of cerium in potential hard-magnetic intermetallics, *NPJ Quantum Mater.* 6 (1) (2021) 2.
- [42] H. Martínez Sánchez, L.E.Z. Alfonso, J.S.T. Hernandez, D.S. Jaramillo, G.A.P. Alcázar, Effect of nitrogenation on the intrinsic magnetic properties of the compounds (Nd_{1-x}Ce_x)₁₁Fe₁₀CoTi, *IEEE Trans. Magn.* 56 (11) (2020) 1–5.
- [43] A. Dasmahapatra, R. Martínez-Casado, C. Romero-Muñiz, M.F. Sgroi, A.M. Ferrari, L. Maschio, Doping the permanent magnet CeFe₁₁Ti with Co and Ni using ab-initio density functional methods, *Physica B* 620 (2021) 413241.
- [44] Y. Harashima, K. Terakura, H. Kino, S. Ishibashi, T. Miyake, First-principles study on stability and magnetism of NdFe₁₁M and NdFe₁₁MN for M = Ti, V, Cr, Mn, Fe, Co, Ni, Cu, Zn, *J. Appl. Phys.* 120 (20) (2016) 203904.
- [45] H. Akai, Nuclear spin-lattice relaxation of impurities in ferromagnetic iron, *Hyperfine Interact.* 43 (1) (1988) 253–270.
- [46] P.H. Dederichs, R. Zeller, H. Akai, H. Ebert, Ab-initio calculations of the electronic structure of impurities and alloys of ferromagnetic transition metals, *J. Magn. Magn. Mater.* 100 (1) (1991) 241–260.
- [47] R. Wienke, G. Schütz, H. Ebert, Determination of local magnetic moments of 5d impurities in Fe detected via spin-dependent absorption, *J. Appl. Phys.* 69 (8) (1991) 6147–6149.
- [48] M.I. Bartashevich, T. Goto, R.J. Radwanski, A.V. Korolyov, Magnetic anisotropy and high-field magnetization process of CeCo₅, *J. Magn. Magn. Mater.* 131 (1) (1994) 61–66.
- [49] T.W. Capehart, R.K. Mishra, G.P. Meisner, C.D. Fuerst, J.F. Herbst, Steric variation of the cerium valence in Ce₂Fe₁₄B and related compounds, *Appl. Phys. Lett.* 63 (26) (1993) 3642–3644.

Appendix

Here I would like to introduce two submitted manuscripts that are related to the topic of this dissertation. While both are currently under review in scientific journals, their unpublished status precludes their inclusion into this thesis. Nevertheless, their relevance and alignment warrant their mention here.

Searching for magnetically hard monoborides (and finding a few): A first-principles investigation

In the paper entitled *Searching for magnetically hard monoborides (and finding a few): A first-principles investigation*, I have analyzed the potential of transition metal monoborides, such as MnB, FeB and CoB and their alloys, as new hard magnetic materials. Both MnB and FeB materials crystallize in an orthorhombic structure with a space group $Pnma$. From literature, we know that MnB exhibits a relatively high Curie temperature of 568 K, but its weak coercive field of 15.9 Oe is not enough for consideration of the monoboride as a permanent magnet. Similarly, FeB, which have an experimentally measured Curie temperature of 590 K and coercive field of 10 Oe, is limited from application as permanent magnets.

In this work, DFT calculations were used to determine key magnetic properties of considered phases. I calculated magnetocrystalline anisotropy energy, magnetic hardness and Curie temperature. The main focus was on understating the magnetic behavior of MnB, FeB, (Mn-Fe)B alloys, and other alloys with transition metals from $3d$, $4d$ and $5d$ group. For alloy systems in the range from CrB-MnB-FeB-CoB, the virtual crystal approximation was used to model the dependence of the valence band occupancy on the magnetic properties. Additionally, the fully relativistic fixed spin moment calculations were applied to show the dependence of magnetocrystalline anisotropy energy on magnetic moment.

For MnB the MAE was determined as 0.45 MJ m^{-3} with the easy axis oriented along [010] direction. FeB in contrast has lower value of MAE equal to 0.14 MJ m^{-3} with the same orientation of easy axis. However, for the (Mn-Fe)B alloy with composition

Mn_{0.55}Fe_{0.45}B, the MAE reached the maximum value of 0.77 MJ m⁻³ with magnetic hardness equal to 0.83. In this range, the maximum value of magnetic hardness was obtained for the Mn_{0.15}Fe_{0.85}B and is equal to 0.95, while the MAE value is equal to 0.69 MJ m⁻³. Going with the electron occupancy to the higher values in the range of (Fe-Co)B alloys hard magnetic properties exhibit more promising key values. The highest value of MAE was obtained for the Fe_{0.5}Co_{0.5}B and it is equal to 2.87 MJ m⁻³ with extraordinary value of magnetic hardness of 5.09.

Additionally, alloying of MnB and FeB was tested with all 3d, 4d, and 5d transition metals. Most of the resultant alloys can be classified as magnetically soft or semi-hard. Nevertheless in case of FeB, doping with Sc, Ti, V, Zr, Nb, Mo, Hf, Ta, or W leads to magnetic hardness exceeding unity, making them candidates for permanent magnets. Calculations of the formation energy predict that all the considered alloying in both monoborides could be chemically stable, as they exhibit negative formation energies. The findings suggest potential for these materials in developing new rare-earth free permanent magnets, filling the MAE gap between alnico and neodymium-based magnets. The full text of the submitted manuscript is available at arXiv: <https://arxiv.org/pdf/2403.00138>.

Magnetic hardness of hexagonal and orthorhombic Fe₃C, Co₃C, (Fe-Co)₃C, and alloys with boron, nitrogen, and transition metals: A first-principles study

The manuscript entitled *Magnetic hardness of hexagonal and orthorhombic Fe₃C, Co₃C, (Fe-Co)₃C, and alloys with boron, nitrogen, and transition metals: A first-principles study* is submitted to the journal. This study aimed to identify alternative hard magnetic materials that could fill the gap between rare-earth-based magnets and alnico or ferrite magnets. The density functional theory was utilized to obtain critical properties of the 552 compositions under consideration.

One of the main aspects presented in the publication is the identification of isoelectronic trend in the MAE dependence across the considered alloys with the change of composition. This trend offers a valuable design principle for tailoring magnetic properties of the materials, to achieve desired magnetic characteristics. Such an isoelectronic trend is visible in the manuscript in Fig. 10, presenting a magnetocrystalline anisotropy energy and magnetic hardness dependence on the 3d and 2p average electron occupancy.

When considering alloying with light atoms, boron in particular improves the Curie temperature in the system, while all the transition metal substitutions in hexagonal and orthorhombic Fe₃C phase decrease that value. Nevertheless, for some transition metals substitution, it can be seen in Fig. 7 and Fig. 8 that improvement in magnetic hardness and magnetocrystalline anisotropy can be made in both structures, reaching the highest value of MAE equal to 1.73 MJ m⁻³ for Pt in hexagonal-Fe₃C. This work adopts a comprehensive approach to explore the modification of magnetic properties in

hexagonal and orthorhombic Fe_3C , providing deep analysis and insights into their structural and electronic behavior. The full text of the manuscript is available at arXiv: <https://arxiv.org/pdf/2409.07058>.

About Author

My scientific journey began at Maria Curie-Skłodowska University in Lublin, where I have pursued both my Bachelor of Engineering and Master's studies. At the engineering level, my thesis, titled *Project of UHV chamber for Si epitaxy in ARPES apparatus* was supervised by Prof. dr hab. Mariusz Krawiec. Building on this foundation, my Master's thesis, *Electronic structure of silicene on Au surface*, delved into the intriguing electronic properties of silicene on metallic substrates, also under the guidance of Prof. dr hab. M. Krawiec. Throughout my academic journey, I actively engaged in cutting-edge research projects funded by the National Science Centre of Poland. From March 2017 to February 2019, I participated in the project titled *Silicene on metallic quantum wells*. Later, from October 2019 to July 2020, I participated in the project *Emergent Dirac materials based on Si-Au anisotropic heterostructures*.

In October 2020, I embarked on my Ph.D. journey at the Institute of Molecular Physics, Polish Academy of Sciences, in Poznań. Here, I took on the pivotal role in the research project *Future permanent magnets from design*, also funded by the National Science Center of Poland. This project focuses on the development and optimization of next-generation permanent magnets.

In 2022, I had the privilege of winning a competition organized by the Polish National Agency for Academic Exchange, which awarded me a scholarship for a foreign internship. This opportunity enabled me to spend six months, from March to September 2022, at Uppsala University in Sweden, renowned for its excellence in research and education. During my time there, I engaged and led my own project, while collaborating with leading experts under the supervision of Dr. Ján Ruzs, and gained international experience that has greatly enriched my professional and personal development.

During my PhD studies, I was active in the scientific community by participating in scientific conferences, giving 5 oral talks and presenting my results on 3 poster sessions.

Outlook

Despite the wide range of compositions considered in presented publications amounting to a total of over 800, the DFT methods, though exceptionally precise, are also very time-consuming. Determining magnetic properties, such as magnetocrystalline anisotropy energy, requires the use of fully relativistic methods, which demand significant computational resources and limit the pace of discovering new materials.

To accelerate the search process and improve its efficiency, I'm planning to introduce machine learning (ML) methods based on the previous and future DFT results. The combinations of those two approaches represent a promising strategy for the discovery of new hard magnetic materials with a high value of magnetocrystalline anisotropy energy. As part of my future plans, I intend to create a database based on DFT calculations, covering a wide range of compounds. This database will then serve as the foundation for training machine learning models, such as neural networks and kernel regression, enabling the rapid identification of the most promising candidates for further investigation, significantly speeding up the entire discovery process. After training the prepared models and conducting initial analyses, the materials predicted by the algorithm will undergo detailed DFT calculations. If these materials prove their promising magnetic properties, they will proceed to experimental validation by collaborating with experimental groups. The plan presented here has the potential not only to contribute to the discovery of new materials, but also to optimize existing alloys.

Bibliography

- [1] M. N. Baibich. Giant Magnetoresistance of (001)Fe/(001)Cr Magnetic Superlattices. *Phys. Rev. Lett.*, 61(21):2472, 1988. doi:10.1103/PhysRevLett.61.2472.
- [2] J. Mathon. Theory of tunneling magnetoresistance of an epitaxial Fe/MgO/Fe(001) junction. *Phys. Rev. B*, 63(22), 2001. doi:10.1103/PhysRevB.63.220403.
- [3] J. M. Slaughter, R. W. Dave, M. DeHerrera, M. Durlam, B. N. Engel, J. Janesky, N. D. Rizzo, and S. Tehrani. Fundamentals of MRAM Technology. *J. Supercond.*, 15(1):19, 2002. ISSN 1572-9605. doi:10.1023/A:1014018925270.
- [4] Z. Li. Magnetization dynamics with a spin-transfer torque. *Phys. Rev. B*, 68(2), 2003. doi:10.1103/PhysRevB.68.024404.
- [5] D. Apalkov, A. Khvalkovskiy, S. Watts, V. Nikitin, X. Tang, D. Lottis, K. Moon, X. Luo, E. Chen, A. Ong, A. Driskill-Smith, and M. Krounbi. Spin-transfer torque magnetic random access memory (STT-MRAM). *J. Emerg. Technol. Comput. Syst.*, 9(2):13, 2013. ISSN 1550-4832. doi:10.1145/2463585.2463589.
- [6] T. Dutta, K.-H. Kim, M. Uchimiya, E. E. Kwon, B.-H. Jeon, A. Deep, and S.-T. Yun. Global demand for rare earth resources and strategies for green mining. *Environ. Res.*, 150:182, 2016. ISSN 0013-9351. doi:10.1016/j.envres.2016.05.052.
- [7] K. M. Goodenough, F. Wall, and D. Merriman. The Rare Earth Elements: Demand, Global Resources, and Challenges for Resourcing Future Generations. *Nat. Resour. Res.*, 27(2):201, 2018. ISSN 1573-8981. doi:10.1007/s11053-017-9336-5.
- [8] R. Skomski and J. M. D. Coey. Magnetic anisotropy — How much is enough for a permanent magnet? *Scr. Mater.*, 112:3, 2016. ISSN 1359-6462. doi:10.1016/j.scriptamat.2015.09.021.
- [9] H. Eschrig. *The Fundamentals of Density Functional Theory*, volume 32 of *TEUBNER-TEXTE Zur Physik*. Vieweg+Teubner Verlag, Wiesbaden, 1996. ISBN 978-3-8154-3030-9 978-3-322-97620-8. doi:10.1007/978-3-322-97620-8.
- [10] H. Eschrig. *2. The Essentials of Density Functional Theory and the Full-Potential Local-Orbital Approach*, page 7. Springer Berlin Heidelberg, Berlin, Heidelberg, 2004. ISBN 978-3-540-39915-5. doi:10.1007/978-3-540-39915-5_2.

- [11] K. Lejaeghere *et al.* Reproducibility in density functional theory calculations of solids. *Science*, 351(6280), 2016. doi:10.1126/science.aad3000.
- [12] P. Hohenberg and W. Kohn. Inhomogeneous Electron Gas. *Phys. Rev.*, 136(3B):B864, 1964. doi:10.1103/PhysRev.136.B864.
- [13] K. Koepnik and H. Eschrig. Full-potential nonorthogonal local-orbital minimum-basis band-structure scheme. *Phys. Rev. B*, 59(3):1743, January 1999. doi:10.1103/PhysRevB.59.1743.
- [14] I Opahle, K Koepnik, and H Eschrig. Full-potential band-structure calculation of iron pyrite. *Phys. Rev. B*, 60(20):14035, 1999. doi:10.1103/PhysRevB.60.14035.
- [15] J. P. Perdew, K. Burke, and M. Ernzerhof. Generalized Gradient Approximation Made Simple. *Phys. Rev. Lett.*, 77(18):3865, 1996. doi:10.1103/PhysRevLett.77.3865.
- [16] P. Ziesche and H. Eschrig. *Electronic Structure of Solids '91: Proceedings of the 75. WE-Heraeus-Seminar and 21st Annual International Symposium on Electronic Structure of Solids Held in Gaussig (Germany), Chapter: Unified Theory of Exchange and Correlation beyond the Local Density Approximation*. Walter de Gruyter GmbH, 1991. ISBN 978-3-05-501504-5.
- [17] J. P. Perdew and Y. Wang. Accurate and simple analytic representation of the electron-gas correlation energy. *Phys. Rev. B*, 45(23):13244, 1992. doi:10.1103/PhysRevB.45.13244.
- [18] T. Burkert. Giant Magnetic Anisotropy in Tetragonal FeCo Alloys. *Phys. Rev. Lett.*, 93(2), 2004. doi:10.1103/PhysRevLett.93.027203.
- [19] P. Soven. Coherent-potential model of substitutional disordered alloys. *Phys. Rev.*, 156:809, 1967. doi:10.1103/PhysRev.156.809.
- [20] V. Heine, J. H. Samson, and C. M. M. Nex. Theory of local magnetic moments in transition metals. *J. Phys. F: Met. Phys*, 11(12):2645, 1981. doi:10.1088/0305-4608/11/12/015.
- [21] P. Goodman and A. F. Moodie. Numerical evaluations of N-beam wave functions in electron scattering by the multi-slice method. *Acta Crystallogr. Sect. A*, 30(2):280, 1974. ISSN 1600-5724. doi:10.1107/S056773947400057X.
- [22] K. Ishizuka and N. Uyeda. A new theoretical and practical approach to the multislice method. *Acta Crystallogr. Sect. A*, 33(5):740, 1977. ISSN 1600-5724. doi:10.1107/S0567739477001879.
- [23] K. Ishizuka. A practical approach for STEM image simulation based on the FFT multislice method. *Ultramicroscopy*, 90(2):71, 2002. ISSN 0304-3991. doi:10.1016/S0304-3991(01)00145-0.

- [24] K. Ishizuka. FFT Multislice Method—The Silver Anniversary. *Microsc. Microanal.*, 10(1):34, 2004. ISSN 1431-9276. doi:10.1017/S1431927604040292.
- [25] J. M. Cowley and A. F. Moodie. The scattering of electrons by atoms and crystals. I. A new theoretical approach. *Acta Crystallogr.*, 10(10):609, 1957. ISSN 0365-110X. doi:10.1107/S0365110X57002194.
- [26] E. J. Kirkland. *Advanced Computing in Electron Microscopy*. Springer US, Boston, MA, 2010. ISBN 978-1-4419-6532-5 978-1-4419-6533-2. doi:10.1007/978-1-4419-6533-2.
- [27] K. Lyon and J. Ruzs. Parameterization of magnetic vector potentials and fields for efficient multislice calculations of elastic electron scattering. *Acta Crystallogr. A*, 77(6):509, 2021. ISSN 2053-2733. doi:10.1107/S2053273321008792.
- [28] R. F. Egerton. *Physical Principles of Electron Microscopy*. Springer US, Boston, MA, 2005. ISBN 978-0-387-25800-3 978-0-387-26016-7. doi:10.1007/b136495.
- [29] D. B. Williams and C. B. Carter. *Transmission Electron Microscopy*. Springer US, Boston, MA, 2009. ISBN 978-0-387-76500-6 978-0-387-76501-3. doi:10.1007/978-0-387-76501-3.
- [30] C. Kittel. *Introduction to Solid State Physics*. Wiley, Hoboken, NJ, 8 edition, 2004. ISBN 978-0-471-41526-8.
- [31] J. Marciniak, W. Marciniak, and M. Werwiński. DFT calculation of intrinsic properties of magnetically hard phase L1₀ FePt. *J. Magn. Magn. Mater.*, 556:169347, August 2022. ISSN 0304-8853. doi:10.1016/j.jmmm.2022.169347.
- [32] M. U. Farooq, A. Hashmi, T. Ono, and L. Huang. Spin–valley Hall phenomena driven by Van Hove singularities in blistered graphene. *Npj Comput. Mater.*, 6(1):1, 2020. ISSN 2057-3960. doi:10.1038/s41524-020-00470-9.
- [33] K.-H. Ding and Z.-G. Zhu. Van Hove singularity–induced negative magnetoresistance in Dirac semimetals. *Phys. Rev. B*, 108(24):245158, 2023. doi:10.1103/PhysRevB.108.245158.
- [34] J. C. Loudon. Antiferromagnetism in NiO Observed by Transmission Electron Diffraction. *Phys. Rev. Lett.*, 109(26):267204, December 2012. doi:10.1103/PhysRevLett.109.267204.